AN ABSTRACT OF THE THESIS OF

Chris Shinya Tomine for the degree of Doctor of Philosophy in Mechanical Engineering presented on October 19, 1973

Title: Integrated Forward Light Scattering As A Measure of Aerosol Mass Concentration.

Abstract approved: Redacted for privacy

Dr. Richard W. Boubel

A mathematical model was developed that relates the ratio, R, of two light flux measurements to the mass concentration, m, of the atmospheric aerosol particles between a source of parallel light (e.g., the sun) and the measuring system. R is defined as the ratio of the light fluxes passing through the pinhole and open positions of an iris diaphragm located in the focal plane of a lens system. The following relationship between the two variables was derived:

$$R = 1/(1 + Km)$$

where K is a constant that depends on the area of the lens surface, the mean wavelength of the incident light, the thickness of the turbid layer of air through which the light travels, and the parameters of the assumed Junge particle size distribution, including the specific gravity of the aerosol.

An experimental investigation was conducted under limited laboratory conditions. The results were in agreement with the functional form of the mathematically derived relationship. Quantitative agreement was not achieved between the experimental and mathematical values of K due to the dissimilarities in the experimental and atmospheric aerosol size distributions.

Integrated Forward Light Scattering as a Measure of Aerosol Mass Concentration

by

Chris Shinya Tomine

A THESIS

submitted to

Oregon State University

in partial fulfillment
of the requirements for the
degree of

Doctor of Philosophy

June 1974

APPROVED:

Redacted for privacy

Professor of Mechanical Engineering in charge of major

Redacted for privacy

Head of Department of Mechanical Engineering

Redacted for privacy

Dean of Graduate School

Date thesis is presented Oct. 19, 1973

Typed by Ellie Peck for Chris Shinya Tomine

ACKNOWLEDGMENT

The author gratefully acknowledges the patience exhibited and the helpful comments provided by the thesis committee: Dr. R. W. Boubel (major professor), Dr. D. Falkenberry, Dr. R. Wilson and Dr. H. Easterday.

Acknowledgment is also due to Dr. W. Lowry for his constructive criticisms that helped immeasurably in the writing of this thesis.

Last, but not least, acknowledgment is due to the author's wife, Sandra, family and friends for their patience, prodding and support during this long ordeal.

TABLE OF CONTENTS

LIST OF FIGURES

LIST OF TABLES

INTEGRATED FORWARD LIGHT SCATTERING AS A MEASURE OF AEROSOL MASS CONCENTRATION

I. INTRODUCTION

Statement of Problem

From common experience it is known that an aerosol (a suspension of small particles in the air) introduced into the path of a light wave results in a scattering of a certain fraction of the light from its original path. For example, on clear days shadows are sharp and distinct due to the nearly parallel rays of the sun. However, on hazy, foggy, or smoggy days, i.e., days when there are many particles in the air, shadows become more and more diffuse with increasing aerosol concentration as light is scattered away from its original path and into the shadow area. This sunlight that is scattered from its original path appears to come from all directions and is called "air-light" (Middleton, 1952). Since the amount of air-light is apparently related to the aerosol concentration, the question arises: is there a monotonic, well-defined relationship between the air-light flux and the aerosol concentration?

Objective and Scope of Investigation

The objective of this dissertation is: (1) to develop a mathematical model relating quantitatively, the air-light flux and the aerosol concentration for atmospheric aerosols, and (2) to investigate the relationship experimentally in the laboratory.

The scope of the experimental investigation is limited to results obtained in a confined laboratory test chamber with aerosols produced with a nebulizer-type generator, and aerosol concentrations measured with a Sinclair-Phoenix aerosol photometer in units of milligrams of aerosol per liter of air. The mathematical model is based on an empirical aerosol size distribution deduced from measurements made in the real atmosphere. It is beyond the scope of this investigation to produce such a distribution, however, the distribution used will allow conclusions to be reached concerning the effect of narrowing the range of particle diameters in the aerosol. The mathematical model developed in this manner however, has potentially a much greater applicability, albeit beyond the limits of this experiment.

II. BACKGROUND

Light Scattering-Qualitative Description

The mechanism of light scattering is relatively simple to describe qualitatively. When light, an electromagnetic wave, is incident on a particle, and has a frequency that does not approach any of the resonant frequencies of lattice vibration or electronic transition, then the electrons in the particle are forced to oscillate at the same frequency as the impressed electromagnetic oscillation. This follows directly from the fact that the electron, bearing an electrical charge, experiences a force in the electric field parallel to the field, and in the magnetic field, perpendicular to the field. Since light consists of an electric field and a magnetic field perpendicular to each other that oscillate at the same frequency, the electron, or any other charged particle under its influence, will be forced to oscillate at the same frequency. These accelerating electrons in turn radiate light in all directions of the same frequency, as any accelerating charge will do. The intensity of this re-radiated or scattered light, however, is not the same in all directions. Light from each of the electrons in a given particle originate at different locations within the particle and thus, pathlengths to any

observation point and the phase relationships among the waves will vary. If the angle of scattering is such that the waves from individual electrons are in phase, then the superposition of the waves results in an intensity maximum. If the angle is such that the waves are 180° out of phase, then an intensity minimum results. Light scattered by small particles then, is omni-directional, but varies in intensity with the scattering angle.

Light Scattering - Quantitative

A rigorous mathematical description of the phenomenon of light scattering by small particles requires the solution of Maxwell's equations of electromagnetic theory. The solution must then be subjected to the requisite boundary conditions on the electric and magnetic field vectors at the particle-air interface. This problem can be reduced to the solution of a three-dimensional vector wave equation, which is solved most easily in spherical coordinates due to the nature of the solution, i.e., an out-going spherical wave (Stratton, 1941; Van De Hulst, 1957; Kerker, 1969). The application of the boundary conditions, in actual practice, becomes extremely complex except in the simplest case of a spherical particle. The details of this problem of light scattering by small (dimensions on the same order of magnitude as the wavelength of the light) spherical particles

were worked out by Gustav Mie in 1908, following the treatment of Debye's 1908 thesis. These solutions, however, are most commonly referred to as the Mie solutions. These Mie solutions give the intensity of scattered light as a function of the scattering angle, θ, the index of refraction, n, and the parameter $\alpha = \frac{2\pi r}{\lambda}$, where r is the particle radius and λ is the wavelength of light. The form of these solutions, however, is a very slowly converging infinite series of associated Le Gendre polynomials, spherical Bessel functions and exponential functions, and consequently, numerical values in closed form were not obtainable until the advent of high speed computers in the mid-1940s. Since then, numerous tables of the numerical solutions for various values of the parameters and n, have been prepared. Typical scattering patterns calculated from the Mie solutions are shown as plots of intensity vs scattering angle in Figure 1.

Several conclusions can be drawn from these figures: (1) angular maxima and minima in the intensity are present as predicted by the qualitative arguments, (2) the number and angular location of the maxima are dependent on r and λ through α, and (3) there exists an omnipresent and predominant forward scattering lobe (in the 0° direction).

As indicated, the preceding discussion applies only to single spherical particles. The problem of scattering from single particles of arbitrary, or even regular but

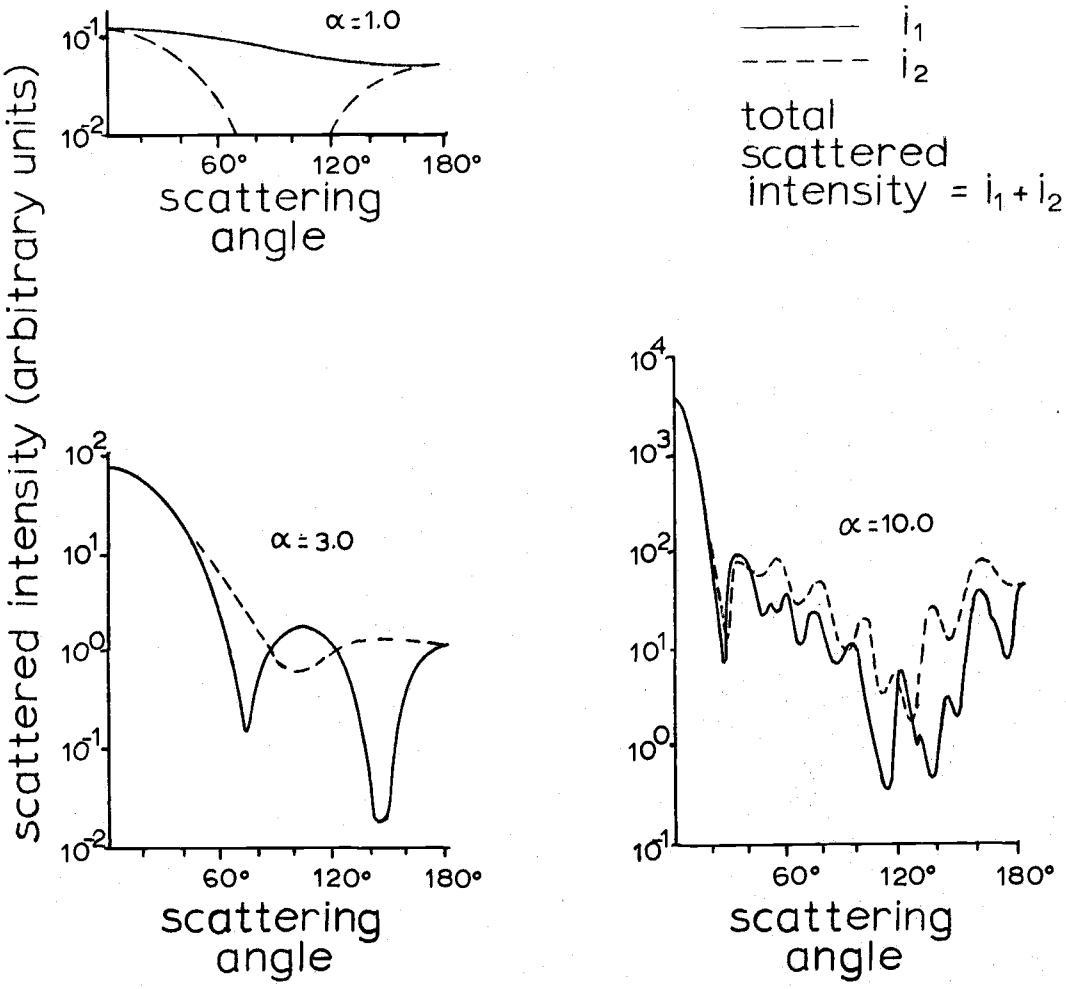

Figure 1. Angular distribution of monochromatic light scattered by single spheres of refractive index 1.5.

non-spherical shape becomes almost impossible to solve. Hodkinson (1966) however, has determined that a large number of randomly oriented non-spherical particles together as a group has a resultant scattering pattern that closely approximates that of a polydisperse (i.e., of many different diameters) assembly of spheres of equal mean volume. The explanation for this lies in the fact that the scattering pattern of an assembly of particles is a simple superposition of the scattering patterns of the individual particles, and the smoothing effect that the variation in orientation produces on the scattering pattern of the assembly of non-spherical particles is comparable to the smoothing effect that the variation in sizes produces in the assembly of spherical particles. These smoothing effects are a direct result of the superposition of the scattering patterns from the individual particles. In the case of the spherical particles, different particles have scattering patterns that differ in the number and location of its maxima and minima by virtue of the differences in the diameters. As a result, a large assembly of such particles has a combined scattering pattern that loses its rapidly oxcillating maximum and minimum intensities (Figure 2). Hodkinson's conclusion implies then that an assembly of randomly oriented non-spherical particles scatters light in a manner that is similar to a polydisperse assembly of spherical particles and therefore

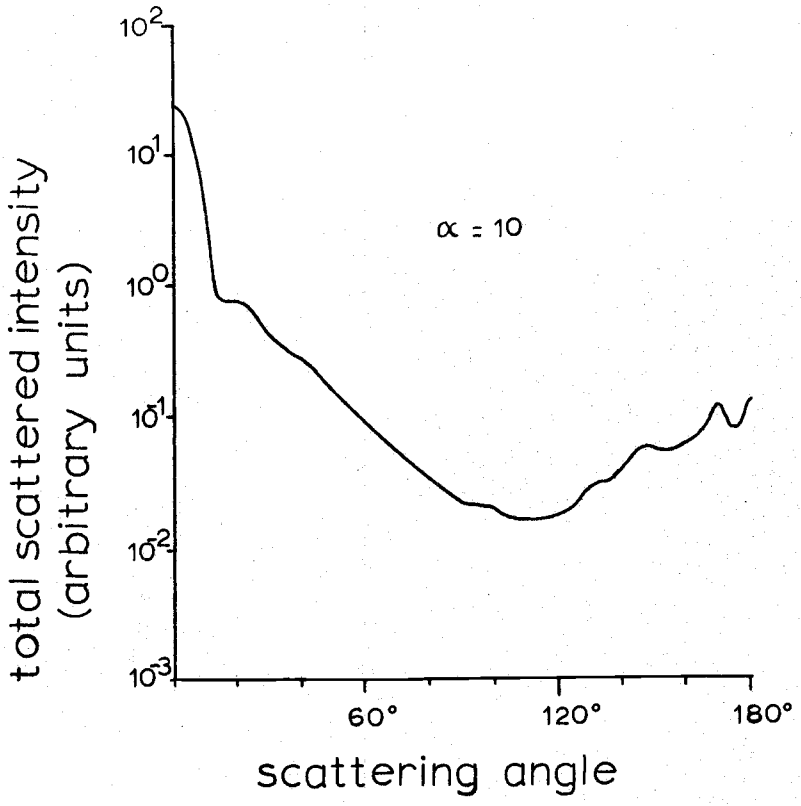

Figure 2. Angular distribtuion of monochromatic light by poly-disperse spheres of refractive index 1.33.

following the Mie theory. Hodkinson adds further that if the smoothing effect of polychromatic light is added to that of the orientation and size polydispersity, the resemblance of the two scattering patterns becomes even closer (recall that the pattern of maxima and minima depends on λ as well as diameter). Cadle (1965) reaches the same conclusion for light scattering in the forward lobe.

Thus, using the Mie solutions as guides, certain conclusions can be drawn concerning the passage of light through an aerosol "cloud." First, the intensity of the scattered light is the greatest about the forward direction. This is due both to the constant occurrence of the forward lobe in the scattering patterns of all particles and also to the large relative magnitude of the forward lobe. Hodkinson (1966) estimates that the light flux in the forward lobe is about 84% of the flux geometrically incident on the particles. The second conclusion is that the occurrence of the forward lobe is independent of λ, n or d (the magnitude, of course, is not). The third conclusions follows from the first, and it is that in the forward direction, multiple scattering becomes relatively negligible, i.e., the addition of light that has been scattered successively by two or more particles into the forward direction, to the light that has been scattered only once into the forward direction, is negligible. It

is evident that the intensity of the once-scattered light is much greater than that of the twice-scattered light. The difference becomes proportionally greater for higher orders of multiple scattering. The subtraction of light, however, from that which has been scattered only once into the forward direction, due to subsequent scattering, is not negligible, but can be accounted for quite simply by the well known exponential attenuation law. This law (Cadle, 1965; Hodkinson, 1966; Bullrich, 1964; Van De Hulst, 1957), which is also known as Bouguer's or Beer's or the Beer-Lambert law, states that light is removed from a beam in passing through a turbid medium in such a manner that:

$$f = f_0 \exp -bl \qquad (1)$$

where: f = light flux at distance l
f_0 = light flux at distance 0
b = attenuation coefficient
l = pathlength of light

The fourth conclusion is that the use of white light would make the Mie solution (spherical particles) more applicable to arbitrary particles.

The conclusions suggest that the measurement of air-light would be most feasible in directions making only small angles with the incident light and with polychromatic or white light.

It should be noted that the term "forward scattered light" as used in the preceding discussion should not be confused with or be interpreted as referring to the "unscattered light." These two terms must be strictly differentiated in any application of light scattering or extinction principles. When a beam of light passes through a volume of air containing suspended particles, some of the light is scattered by the particles but some of the light passes through without encountering any particles in its path. The proportion of the light that is scattered of course depends on the concentration of the particles in the volume. Of the light that is scattered, some will be scattered in the forward direction, i.e., in the same direction as the original beam and therefore in the same direction as the unscattered light. Since the Mie solutions and the scattering patterns are applicable to and predict only the intensities of the <u>scattered</u> light, and since the exponential light attenuation law is applicable only to the <u>unscattered</u> light, it becomes absolutely essential to distinguish between the forward scattered light and the unscattered light when applying either or both of these mathematical descriptions to light measurements in the forward directions.

Applications to Aerosol Measurements

The principles of light scattering have been applied quite extensively to the measurement of various aerosol parameters. True scattering measurements, i.e., measurements of the scattered light, however, have been largely limited to single particle measurements or to measurements on a very small volume of aerosol-laden air, both within the confines of an instrument test chamber. Measurements in the atmosphere over extended distances, on the other hand, have generally been extinction measurements, i.e., measurements of the light that remains after scattering removes a certain fraction of the original light.

Sinclair (1953, 1967) describes a method for measuring aerosol mass concentrations in which aerosol-laden air is passed through the focal point of a converging light beam so that only one particle at a time can enter the zone where it can scatter light. A photomultiplier tube is placed opposite the light source on the axis of the light beam, but normally registers no light because it is just covered by a shadow created by an opaque screen placed on a part of the condensing lens. When the particle passes through the light beam, between the condensing lens and the photomultiplier tube, a pulse of light is scattered into the shadow region and thus registers on the photomultiplier tube. The size and frequency of these

pulses indicate the aerosol mass concentration. Similar methods are discussed by Gucker and Rose (1954) and Clarenburg and Princen (1963).

A particle analyzer described by Gucker (1956) utilizes a similar principle, except that the photomultiplier tube is at right angles to the axis of the converging light beam, and the necessity of the opaque screen is eliminated. O'Konski, Briton and Higuchi (1958), Fisher, Katz, Lieberman and Alexander (1955), and Zinky (1962) have also described 90° scattering instruments.

30° aerosol counters have been designed by Berek, Maennchen and Schaefer (1936), Stuke (1955), and Stuke and Rzeznik (1964).

45° aerosol counters have been designed by Koshi (1958), Thomas and Oglesby (1959), Thomas, Bira, Collins and Rice (1961) and Randall and Keller (1965).

The integrating nephelometer of Beutell and Brewer (1949) and Charlson et al. (1967) measures the scattering coefficient of aerosol-laden air by illuminating a four liter volume of the air with a zenon flash lamp and sensing the light scattered into a photomultiplier tube placed at right angles to the flash. The measured value of light flux in this instrument is that which is integrated over all of the particles in the volume sensed by the photomultiplier tube, as well as all of the angles of acceptance

of the photomultiplier tube.

As stated earlier, all of these light scattering studies referenced in the preceding paragraphs concern point measurements, i.e., measurements made on the air from only one point or location in the atmosphere. One exception is the work of Collis et al. (Collis and Ligda, 1964; Collis, Fernald and Ligda, 1964) who have utilized back-scattering from a Q-switched ruby laser beam as an optical radar for detecting discontinuities in the atmospheric aerosol loading. Quantitative measurements of the aerosol concentration, however, are not obtained.

The most common light measurements over extended distances in the atmosphere are the extinction measurements. Volz (1959) describes a photometer that in essence measures the extinction of sunlight due to its passage through the atmosphere. By measuring the flux of unscattered light at ground level and utilizing estimates of the fixed value of extra-terrestial solar flux and its path length based on the elevation angle of the sun at the time of measurement, the attenuation coefficient of the atmosphere is obtained from the exponential attenuation law (Equation 1).

The transmissometer (Rockney, 1959) operates on the same principle as the Volz sun photometer except that a ground level collimated light source is used instead of sunlight.

One study, that of Chinn et al. (1955) merits further discussion due to its similarities to this dissertation. Chinn proposes a method for obtaining particle size distributions for particles that are large compared to the wavelength of the incident light, by illuminating the test atmosphere with a collimated light source and measuring the scattered flux contained in the forward cone as a function of the cone angle. Using a mathematical model based on a modified Bouguer's law and an involved graphical differentiation and integration of plotted functions of the measured quantities, the size distribution is obtained. The similarity of Chinn's study to this investigation lies in the similar but independently conceived optical systems (described in section IV) used to measure the scattered light, and consequently the similar measurements that are made. However, where Chinn makes measurements for many values of the cone angle, in this investigation a measurement is made at only one angle. The flux measured at this cone angle is then divided by the value of the unscattered flux and correlated directly with the desired parameter, which in this investigation is the mass concentration. The mathematical model here is not integral to the data reduction as is the case in Chinn's work. Lastly, it should be noted that the results of this investigation, although providing different information about the aerosol

than the size distribution, may have greater practical use in the field of air pollution, since: (1) air quality standards, both Federal and California, are expressed in terms of mass concentrations, and (2) Chinn's model is subject to the condition that the measured particles be large compared to the wavelength of the light. It has been shown that particles that are approximately equal to the wavelength of light have the greatest effect on health (Hatch, 1961; Hilding, 1965; Nadel, 1965) and visibility (Steffens, 1956; Steffens and Rubin, 1949).

III. MATHEMATICAL MODEL

Assumptions

The following mathematical model is based on three assumptions. The first assumption is that the Mie solution will be applicable to large numbers of non-spherical particles if they are randomly oriented and the light is polychromatic. The second assumption is that aerosol particles will be distributed in size according to the Junge distribution. The third assumption is that the index of refraction of the aerosol will have very little effect on the experimental results, and therefore an average value of 1.5 (Bullrich, 1964) may be used in the calculations. This follows from the conclusion of Pueschel and Noll (1967) that the scattering coefficient of tropospheric aerosols is nearly independent of the index of refraction if the aerosol has a Junge's size distribution. Bullrich (1964) concludes that the effect of the index of refraction diminishes as the aerosol becomes more polydisperse. Hodkinson (1966) explains that the scattering in the forward lobe is independent of the optical properties of the particle because it is due to Fraunhofer diffraction which arises from light passing near the particle rather from

rays undergoing reflection and refraction.

The Junge size distribution (Junge, 1955, 1958, 1963; Friedlander and Wang, 1966; Whitby and Clark, 1966; Peterson and Paulus, 1967) is an empirically determined particle size distribution based on experiments on atmospheric aerosols and is commonly used in calculations where an analytical expression is required for aerosol size distributions (McCormick and Baulch, 1962; Bullrich, 1964; Charlson, 1968). The expression is written as follows:

$$dn(r) = cr^{-\nu}\, d(\log r) \qquad (2)$$

where: $dn(r)$ = the number of particles per unit volume with radii between r and $r+dr$

c = a constant of proportionality depending on the total number of particles per unit volume of air

ν = a number between 2.5 and 4.0

Junge (1955, 1958) found that the value of 3.0 for the exponent ν gave the best fit to his experimental data. Bullrich (1964) states that "the majority of direct aerosol measurements and indirect optical measurements indicate that $\nu = 3$ gives the best fit to the natural size distribution."

Due to the empirical nature of equation (2), the results developed in the following sections are not

entirely theoretical, although the word "theoretical" is used for convenience to differentiate between the analytically and experimentally obtained results.

Choice of Parameters

The first and most important parameter that must be chosen is that which provides some quantitative measure of "air-light." Some insight into this choice is provided by the discussion at the end of section II, which suggests that: (1) air-light of all wavelengths be measured (white light), (2) air-light making only small angles with the incident light be measured, and (3) scattered and unscattered light be distinguished. It will be seen that the satisfaction of requirement (3) will suggest a means for the satisfaction of requirement (2) which will subsequently lead to the definition of the parameter under search.

The requirement (3) is quite simple to achieve utilizing a lens-pinhole system as shown in Figure 3. The pinhole is located in the focal plane of the lens and is centered on the lens. The result is that only light incident on the lens parallel to the lens-pinhole axis can pass through the pinhole. Any light not parallel to the axis, focuses at a point in the focal plan whose distance from the axis, and thus the pinhole, is given by:

$$x = y \tan \theta \qquad (3)$$

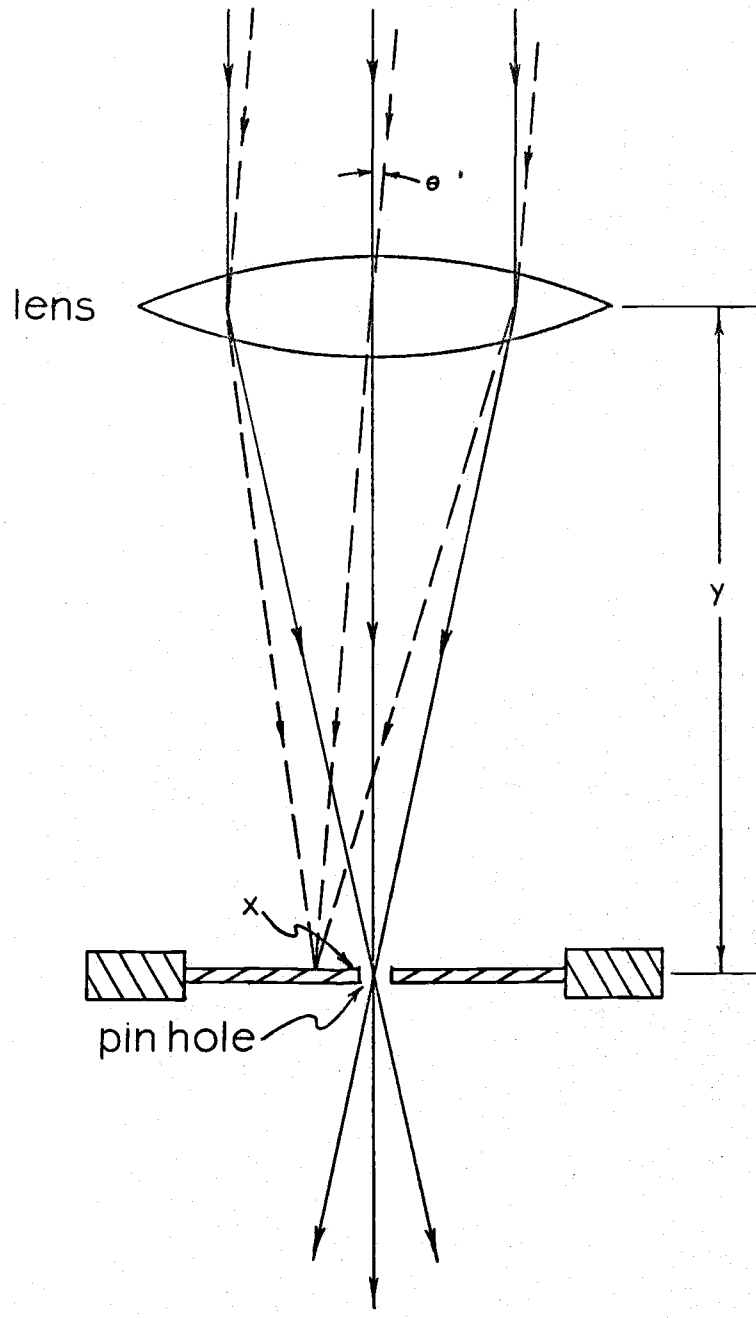

Figure 3. Lens-pinhole system.

where: y = focal length of the lens

θ = angle of incidence of the light

If the axis of the lens-pinhole system is aligned with a parallel beam of light, then essentially, only light that has not been scattered passes through the pinhole. The word "essentially" is used because a very minute fraction of the light scattered through small angles does pass through the pinhole partly because some of it is exactly parallel to the incident beam but mostly because the finite size of the pinhole does allow light that is slightly off of parallel to pass through as well. A numerical calculation will give an indication of how small this fraction is in this investigation. A 1 mm diameter pinhole and a 100 mm focal length lens were used which allowed light up to an angle of 0.17° to pass through the pinhole. Figure 2 shows that the forward lobe representing about 84% of scattered light lies within approximately 30° of the forward of 0° direction. The ratio of the solid angles corresponding to cones of half-angles 0.17° and 30°, is only 0.00007. Thus, the scattered light that was allowed to pass through the pinhole, as a result of its finite size, was that which was contained in a solid angle that was only 0.007% of the forward lobe.

If the pinhole in Figure 3 is replaced by an iris diaphragm, then it can be opened up to admit light that

has been scattered through angles greater than 0.17°. (Of course, this scattered light will still be in addition to the unscattered light.) In this investigation, the diaphragm was opened up to admit light with an angle of incidence up to 5°. The light that passed through the iris diaphragm in the open position then was the unscattered light incident on the lens plus the "air-light" incident on the lens with angles of incidence less than 5°. A measurement of this light flux passing through the open diaphragm could be chosen as the parameter being sought but the mathematical model developed in the next section suggests that the value of the original flux, f_o, in the term for the unscattered light (refer back to Equation 1), can be eliminated by dividing the flux passing through the diaphragm in the pinhole position by that passing through in the open position. Consequently, it becomes beneficial to choose as the parameter measuring airlight, the ratio

$$R = f_{pinhole}/f_{open} \qquad (4)$$

where: $f_{pinhole}$ = light flux passing through pinhole

f_{open} = light flux passing through diaphragm in the open position

The parameter used to measure the aerosol concentration in this investigation is the mass loading or concentration, i.e., the mass of aerosol per unit volume of air,

and will be designated by the letter m. This choice is made primarily because in air pollution work, this is the standard parameter for specifying suspended particulate concentrations.

Physical Description

The physical description of the model follows directly from the definition of the ratio R. Recall that the ratio R is defined from an operational standpoint as the ratio of the light flux measured with the iris diaphragm in the pinhole position to the light flux measured with the diaphragm in the open or 5° acceptance angle position. The same ratio can be expressed in terms of the incident light as the ratio of the unscattered light flux incident on the objective lens to the sum of the scattered light flux (scattered through less than 5°) and the unscattered light flux incident on the objective lens, i.e.,

$$R = f_u/(f_s + f_u) \qquad (5)$$

where: f_u = unscattered light flux incident on the objective lens

f_s = scattered light flux (through less than 5°) incident on the objective lens

The relationship between the flux passing through the diaphragm and that incident on the objective lens has already

been discussed in the preceding section.

The flux f_u represents the portion of the light originally traveling towards the objective lens parallel to the optical system axis that actually reaches the objective lens without encountering any particles. This flux decreases with the distance between the light source and the lens since more of the light will be scattered away from its original path by the aerosol. This attenuation follows Bouguer's law (Equation 1) as is well known.

The value of the flux f_s, however, is not known, and constitutes the heart of the mathematical model. The method by which this value will be obtained is to find the contribution that a volume element of air, dV, makes to f_s, and then integrate these contributions df_s over the total volume of air from which contributions can be made.

The contribution from dV can be derived from the knowledge of how individual particles within dV scatter light. This information is provided by the Mie solutions which give the intensity of scattered light in any given direction as a function of the particle radius. Junge's size distribution gives the number of particles of a given radius in dV, and since light flux combines by simple superposition or addition, the flux scattered toward the optical system by all of the particles in dV can be obtained by multiplying the flux scattered in that direction

by a particle of radius r by the number of particles having that radius r, and integrating over all r. This light is attenuated in traveling over the pathlength between the volume element dV and the optical system according to Bouguer's law.

The total volume whose volume elements contribute to f_s is determined by the angle of acceptance of the optical system. Figure 4 shows that this total volume is a right, circular cone with its vertex located at the optical system and whose axis coincides with the optical system axis. The vertex half-angle of the cone is equal to the acceptance angle of the optical system, which in this experiment will be 5°, and the height of the cone is equal to the height of the aerosol chamber. All volume elements dV_i within this cone scatter light toward the vertex (and hence the optical system) through an angle of 5° or less which consequently is measured by a pyranometer. All volume elements dV_o outside of this cone scatter light toward the optical system through angles greater than 5° which therefore is not measured as part of f_s.

The light scattered into the optical system is slightly underestimated in choosing this cone as the volume of integration due to the finite area of the objective lens. This underestimation will be discussed in the last part of this section.

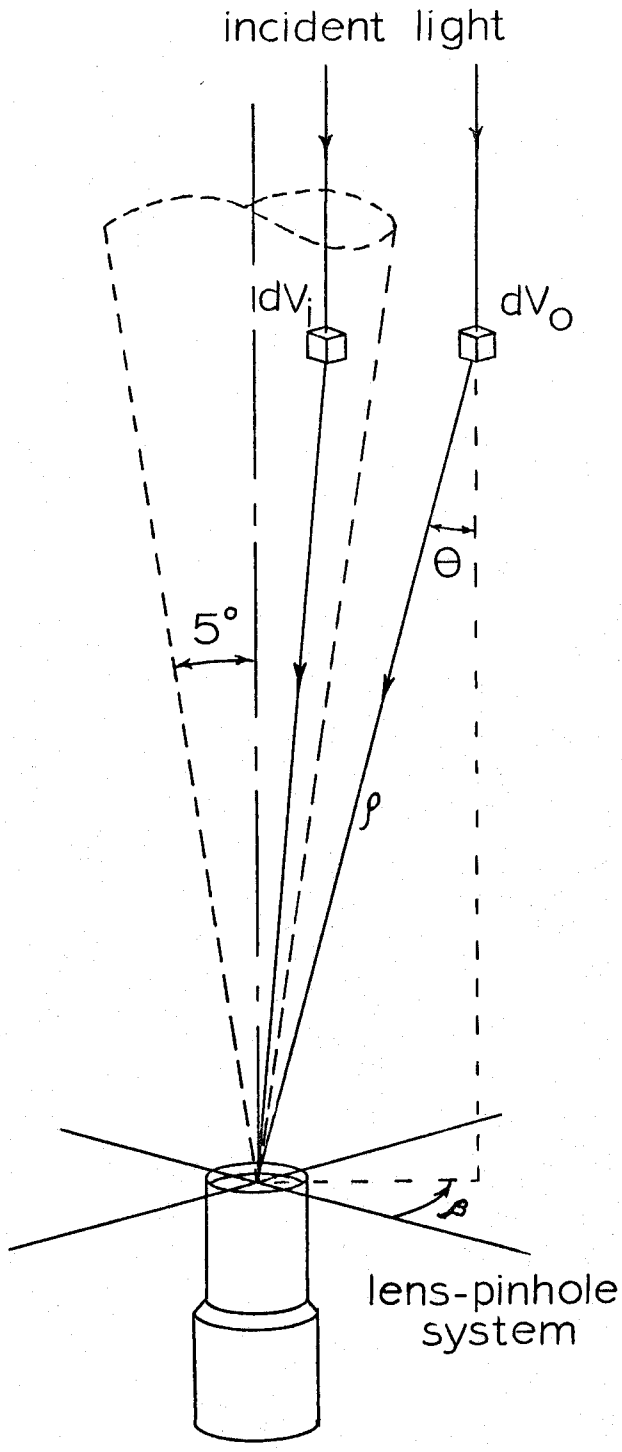

Figure 4. Volume of integration for determining f_s.

Analytical Derivation

The unscattered light flux, f_u, is given by Bouguer's law:

$$f_u = f_o \exp{-bh} \tag{6}$$

where: f_u = flux at the optical system objective lens

f_o = original flux at z = h

h = height of the cone

b = scattering coefficient

Here, the attenuation coefficient, b, is taken as a scattering coefficient and absorption is neglected as is commonly done (Charlson, Horvath and Pueschel, 1967; Robinson, 1968) due to the colorless, transparent nature of the experimental aerosols. The height of the cone, h, in this experiment is the distance between the optical system and the top of the aerosol chamber.

In order to derive the analytical expression for df_s (the contribution to f_s made by dV), the angular scattering distribution as a function of particle radius must be multiplied by the particle size distribution and integrated over all radii. The Mie solution itself, however, is commonly expressed as $i(\phi,r)$ the scattered intensity per unit of incident flux per particle divided by $\lambda^2/8\pi^2$, where λ is the wavelength of the incident light. Intensity is

defined as the flux per unit solid angle emanating from a point, therefore, $i(\phi,r)$ must first be multiplied by f_i (the flux incident on dV), $\lambda^2/8\pi^2$, and the solid angle, Ω, subtended by the objective lens of the optical system in order to give the flux per particle scattered in the direction ϕ. The size distribution given as dn(r) by the Junge equation (Equation 2) expresses the number of particles per unit volume with radii between r and r+dr and thus has to be multiplied by the volume dV in order to give the total number of particles in this size range in dV. Making these multiplications, the flux scattered in the direction of the optical system by the volume element dV is given by:

$$(df_s)_o = \int_r i(\phi,r)\ f_i(\lambda^2/8\pi^2)\Omega\ dV\ dn(r) \qquad (7)$$

Equation (7) gives the expression for the scattered flux leaving dV as a function of ϕ, the scattering angle. Now if the variable ϕ is replaced by the particular angle θ that locates the declination of the volume element dV from the optical system axis, the equation (7) gives the expression for the flux scattered by dV in the direction of the optical system.

$$(df_s)_o = \int_r i(\theta,r)\ f_i(\lambda^2/8\pi^2)\Omega\ dV\ dn(r) \qquad (8)$$

The flux actually reaching the lens, however, has been attenuated in traveling over the pathlength ρ according to Bouguer's law. The contribution to f_s made by the volume

element dV is then:

$$df_s = (df_s)_o \exp [-b\rho] \tag{9}$$

or

$$df_s = \exp[-b\rho] \int_r i(\theta,r)\ f_i(\lambda^2/8\pi^2)\Omega\ dV\ dn(r) \tag{10}$$

The flux, f_i, incident on the volume element dV is simply the original flux, f_o, attenuated according to Bouguer's law also, but in traveling from source at z = h to dV. The pathlength is a function of the location of dV, and is given by:

$$l = h-\rho\cos\theta \tag{11}$$

where: h = the height of the cone

ρ and θ are the spherical coordinates shown in Figure 4.

Thus, the incident flux is given by:

$$f_i = f_o \exp -b(h-\rho\cos\theta) \tag{12}$$

The solid angle, Ω, subtended by the objective lens of the optical system can be expressed in terms of the coordinates of dV as:

$$\Omega = A\cos\theta/\rho^2 \tag{13}$$

where: A = the area of the objective lens

ρ and θ are the spherical coordinates that locate dV

The use of the whole area of the objective lens results in a slight overestimation of the light scattered into the optical system and tends to be cancelled by the underestimation mentioned previously. This overestimation follows from the fact that all of the light from dV incident on A will not be measured since some of it may strike A at an angle greater than 5°. A detailed discussion will be pursued at the end of this section.

The expression for the volume element dV in spherical coordinates is the usual one given by:

$$dV = \rho^2 \sin\theta \, d\theta \, d\beta \, d\rho \qquad (14)$$

where β is used as the azimuthal angle in the spherical coordinate system in place of the customary designation ϕ.

Since equation (10) involves an integration over the particle radii, it is helpful to recast the Junge equation (Equation 2) in terms of the differential dr, instead of dlogr. This is accomplished easily by first converting from base 10 logarithms to natural logarithms and using the identity, dlnr = dr/r. Equation (2) then becomes:

$$dn(r) = 0.434cr^{-(\nu+1)}dr \qquad (15)$$

Grouping the terms containing r, and substituting equation (15) in equation (10) yields:

$$df_s = \exp(-b\rho)0.434cf_i\Omega \, dV(\lambda^2/8\pi^2)\int_r i(\theta,r)r^{-(\nu+1)}dr \qquad (16)$$

The integral in equation (16) can be evaluated using the results of Bullrich (1964) if a change of variables is made from r to α, where $\alpha = 2\pi r/\lambda$. Then:

$$df_s = \exp(-b\rho)0.43cf_1\Omega dV\ 1/2(2\pi/\lambda)^{\nu-2}\eta(\lambda,\theta) \tag{17}$$

where: $\eta(\lambda,\theta) = \int i'(\theta,\alpha)/\alpha^{\nu+1}d\alpha$ (18)

and, $i'(\theta,\alpha)$ is the Mie solution expressed in terms of α.

Equation (18) has been integrated numerically by Bullrich (1964) with limits of integration corresponding to radii of 0.04 microns and 10 microns. The results for an index of refraction of 1.5 are shown in Table I and graphically in Figure 5.

Substituting equations (12), (13) and (14) into equation (17) gives:

$$df_s = \exp(-b\rho)0.434cf_o\exp(-bh+b\rho\cos\theta)(A\cos\theta/\rho^2)x$$
$$\rho^2\sin\theta d\theta d\beta d\rho\ 1/2(2\pi/\lambda)^{\nu-2}\eta(\lambda,\theta) \tag{19}$$

Grouping the constant terms, equation (19) becomes:

$$df_s = K_1\exp(-b\rho - b\rho\cos\theta)\cos\theta\sin\theta\eta(\lambda,\theta)\,d\theta d\beta d\rho \tag{20}$$

where: $K_1 = f_o\exp(-bh)\ 0.434cA\ 1/2(2\pi/\lambda)^{\nu-2}$ (21)

Integrating equation (20) over the conical volume shown in Figure 4, the flux f_s is obtained:

$$f_s = K_1\int_{\theta=o}^{5^\circ}\int_{\rho=o}^{h/\cos}\exp-b\rho(1-\cos\theta)\cos\theta\sin\theta\eta(\lambda,\theta)d\theta d\rho\int_o^{2\pi}d\beta \tag{22}$$

TABLE I

Numerical Values of the Angular Function $\eta(\theta,\lambda)$

θ	η					
	ν=2.5		ν=3.0		ν=3.5	
	λ=.55	λ=.65	λ=.55	λ=.65	λ=.55	λ=.65
1	324.05	286.09	54.91	51.21	12.56	12.20
4	64.16	63.92	19.77	19.75	7.406	7.407
7	33.71	33.62	12.96	12.95	5.742	5.745
10	22.91	22.83	9.841	9.835	4.758	4.760
30	6.072	6.038	3.106	3.104	1.802	1.805
60	1.405	1.398	0.7568	0.7575	0.4821	0.4842
80	0.6263	0.6247	0.3479	0.3489	0.2306	0.2323
90	0.4514	0.4503	0.2547	0.2556	0.1719	0.1736
110	0.2843	0.2845	0.1688	0.1699	0.1190	0.1208
120	0.2600	0.2604	0.1565	0.1577	0.1119	0.1139
130	0.2662	0.2667	0.1592	0.1607	0.1135	0.1157
150	0.4323	0.4329	0.2219	0.2236	0.1414	0.1442
180	1.1613	1.1472	0.4423	0.4428	0.2213	0.2243

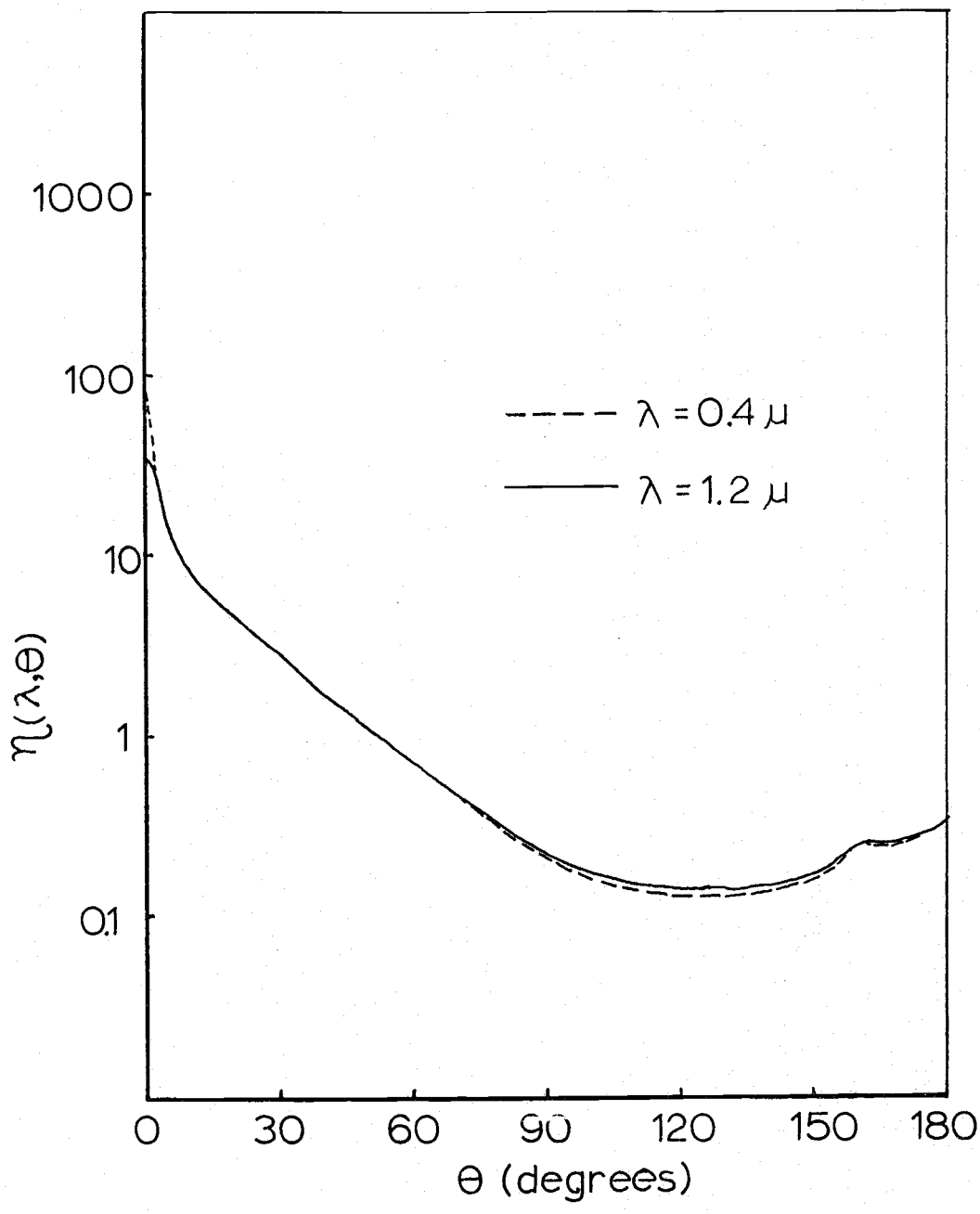

Figure 5. Angular variation of the parameter $\eta(\lambda,\theta)$ for $\nu = 3.0$.

The integration over β can be carried out immediately to yield:

$$f_s = K_1 2\pi \int_{\theta=o}^{5^\circ} \int_{\rho=o}^{h/\cos} \exp -b\rho(1-\cos\theta)\ \cos\theta\sin\theta\eta(\lambda,\theta)d\theta d\rho \qquad (23)$$

The integration over ρ yields:

$$f_s = K_1 2\pi \int_{\theta=o}^{5^\circ} \cos\theta\sin\theta\eta(\lambda,\theta)\ \left[\frac{\exp -b\rho(1-\cos\theta)}{-b(1-\cos\theta)}\right]_o^{h/\cos\theta} d\theta \qquad (24)$$

or:

$$f_s = K_1 2\pi \int_{\theta=o}^{5^\circ} \cos\theta\sin\theta\eta(\lambda,\theta) \left[\frac{(\exp +bh(\cos\theta-1)/\cos\theta)-1}{b(\cos\theta-1)}\right] d\theta \qquad (25)$$

Substituting the series expansion for the exponential term and allowing the term $(\cos\theta-1)/\cos\theta$ to be called X for the moment yields:

$$f_s = K_1 2\pi \int_{\theta=o}^{5^\circ} \frac{\sin\theta\eta(\lambda,\theta)}{bX}\ (1+hbX+\frac{h^2b^2X^2}{2!}+\ldots\ -1)d\theta \qquad (26)$$

or:

$$f_s = K_1 2\pi \int_{\theta=o}^{5^\circ} \frac{\sin\theta\eta(\lambda,\theta)}{bX}\ (hbX+\frac{h^2b^2X^2}{2!}+\ldots)d\theta \qquad (27)$$

Cancelling bX in the numerator and denominator gives:

$$f_s = K_1 2\pi \int_{\theta=o}^{5^\circ} \sin\theta\eta(\lambda,\theta)\ (1+\frac{hbX}{2!}+\frac{h^2b^2X^2}{3!}+\ldots)d\theta \qquad (28)$$

or:

$$f_s = K_1 2\pi h \sum_{n=o}^{\infty} \frac{(hb)^n}{(n+1)!} I_n = K_1 2\pi h \sum_{n=o}^{\infty} S_n \qquad (29)$$

where:
$$I_n = \int_{\theta=o}^{5^\circ} \sin\theta\eta(\lambda,\theta)X^n d\theta \qquad (30)$$

or: $$I_n = \int_{\theta=o}^{5^\circ} \sin\theta\,\eta(\lambda,\theta)\,\left(\frac{\cos\theta-1}{\cos\theta}\right)^n d\theta \qquad (31)$$

and $$S_n = \frac{(hb)^n}{(n+1)!}\, I_n \qquad (32)$$

The behavior of the series in equation (29) can be examined more easily if the first few integrals, I_n, are evaluated. Since only tabulated values of the function $\eta(\lambda,\theta)$ are available, and the functional form is not known, the integrals, I_n, must be solved numerically. The first four integrals in the series were evaluated using Simpson's rule with ten intervals of width 0.5° for three values of the exponent ν, 2.5, 3.0, and 3.5, and two values of the wavelength λ, 0.55 microns and 0.65 microns. The results are shown in Table II. The values for $\eta(\lambda,\theta)$ at 0.5° intervals were interpolated from an enlarged section of figure (5) between 0° and 5°.

The coefficients of the integrals in the summation can be evaluated for the average value of the scattering coefficient, b, encountered in this experiment. This value of b can be approximated using the linear relation between the scattering coefficient and the mass loading used by Charlson (1967) and McCormick and Baulch (1962). This relationship, which is presented as a conversion factor between b and m by Meteorological Research, Inc. with their commercial model of the integrating nephelometer, is as follows:

TABLE II

Values of I_n, for λ = 0.55, 0.65 Microns,
ν = 2.5, 3.0, 3.5

	LAMBDA = .55 MICRONS	LAMBDA = .65 MICRONS
NU = 2.5	I_0 = 2.3793086E 01	I_0 = 2.2445194E 01
	I_1 = -2.9880817E-02	I_1 = -2.9279500E-02
	I_2 = 6.5791815E-05	I_2 = 6.5182517E-05
	I_3 = -1.7653394E-07	I_3 = -1.7547430E-07
NU = 3.0	I_0 = 6.0235972E 00	I_0 = 5.8718988E 00
	I_1 = -8.9117630E-03	I_1 = -8.8250098E-03
	I_2 = 2.0480619E-05	I_2 = 2.0392037E-05
	I_3 = -5.5932891E-08	I_3 = -5.5815547E-08
NU = 3.5	I_0 = 1.8524265E 00	I_0 = 1.8322071E 00
	I_1 = -3.1521791E-03	I_1 = -3.1425358E-03
	I_2 = 7.7000265E-06	I_2 = 7.6922913E-06
	I_3 = -2.1634077E-08	I_3 = -2.1625912E-08

$$m = 0.38 \times 10^{4} b \qquad (33)$$

where: m = mass loading in micrograms per cubic meter

b = scattering coefficient in meters^{-1}

The average value of the mass loading for the one-hundred and fourteen measurements made in this experiment is 28 micrograms per liter. Using equation (33), this gives a value of 7.36 meters^{-1} or 0.0736 cm^{-1} for the scattering coefficient.

The value of h, the height of the conical test volume, is fixed in this experiment at 178 cm.

Using these values, calculations show (see Table IIIa) that the ratio of the absolute values of the second term in the series to the first term is equal to 0.00969, and the third to the first, 9.76×10^{-5}, and the fourth to the first, 8.74×10^{-7}. This is using the integrals for $\nu = 3.0$ and $\lambda = 0.55$ microns. It can be seen that the second and higher order terms are neglibigle when compared to the first term, especially when the alternating nature of the signs on successive terms is considered. Even if the worst possible case is considered, i.e., the highest single mass concentration measured in this experiment (0.116 mg/l, with the corresponding value of b = 0.305 cm^{-1}) and the most slowly decreasing series of integrals ($\nu = 3.5$ and $\lambda = 0.65$ microns), it can be seen (see

TABLE IIIa

S_n and $|S_n/S_o|$, for λ = 0.55 Microns,
ν = 3.0, b = 0.0736 cm^{-1}

n	$(hb)^n/(n+1)!$	I_n	$I_n(hb)^n/(n+1)!$	$\lvert S_n/S_o \rvert$
0	1	6.024	6.024	1
1	6.55	-8.912×10^{-3}	-5.84×10^{-2}	9.69×10^{-3}
2	28.7	2.048×10^{-5}	5.88×10^{-4}	9.76×10^{-5}
3	93.9	-5.593×10^{-8}	-5.26×10^{-6}	8.74×10^{-7}

TABLE IIIb

S_n and $|S_n/S_o|$, for λ = 0.65 Microns,
ν = 3.5, b = 0.305 cm^{-1}

n	$(hb)^n/(n+1)!$	I_n	$I_n(hb)^n/(n-1)!$	$\lvert S_n/S_o \rvert$
0	1	1.832	1.832	1
1	27.15	-3.143×10^{-3}	-8.53×10^{-2}	4.66×10^{-2}
2	492	7.692×10^{-6}	3.79×10^{-3}	2.07×10^{-3}
3	6670	-2.163×10^{-8}	-1.45×10^{-4}	7.91×10^{-4}

Table IIIb) that the ratio of the second term to the first is still only 0.0466.

It should be noted that even the average value of b used in these calculations is extremely large when compared to values found in actual atmospheric measurements. Since light scattering is dependent on the total number of particles in the light path, the short pathlength used in this experiment, due to the physical limitations of the laboratory, is compensated for by a high mass loading. In the real atmosphere, a visibility of a half-mile would correspond to a value for b of 4.87×10^{-5} cm^{-1}. This would be considered extremely high. Using this value of b and the integrals for $\nu = 3.0$ and $\lambda = 0.55$ microns calculations show (Table IV) that the ratio of the second term to the first becomes 6.41×10^{-6}.

Neglecting then the second and higher order terms in the summation in equation (29), the expression for the scattered flux, f_s, becomes:

$$f_s = K_1 2\pi h I_o \tag{34}$$

or substituting for K_1:

$$f_s = f_o \exp(-bh)\ 0.434cA\ 1/2(2\pi/\lambda)^{\nu-2}\ 2\pi h I_o \tag{35}$$

On first glance it appears that the scattered flux, f_s, is dependent on the mass concentration only through the scattering coefficient in the exponential term pre-

TABLE IV

S_n and $|S_n/S_o|$, for λ = 0.55 Microns,
ν = 3.0, b = $4 \times 10^{-5} cm^{-1}$

n	$(hb)^n/(n+1)!$	I_n	$I_n(hb)^n/(n-1)!$	$\lvert S_n/S_o \rvert$
0	1	6.02	6.02	1
1	4.335×10^{-3}	-8.912×10^{-3}	-3.86×10^{-5}	6.41×10^{-6}

cisely as in Bouguer's law, however, a dependence does exist through the "constant" c. Recall that c was considered a constant in equation (2), the Junge size distribution equation, in that it is independent of the variable r, the particle radius, and in equation (16), it was independent of the spatial variables of integration. The dependence of c on the mass concentration, m, can be obtained by returning to equation (2). Note that in equation (2), the shape of the distribution curve is indicated by the terms containing r, but that c serves as a constant of proportionality or normalization constant that raises or lowers the curve to make the area under the curve correspond to the total number of particles in a unit volume of air. This implies that if the Junge distribution (which gives the number of particles of radius r per unit volume of air) is multiplied by the mass of one particle of radius r, then c would have that value which would make the area under this new curve equal to the total mass per unit volume of air. Using this approach, the functional dependence of c on m is obtained by first writing the expression for the mass of the particles of radius r between r and r+dr per unit volume of air:

$$dm = 4/3\pi r^3 \gamma dn(r) \qquad (36)$$

where: $4/3\pi r^3$ = volume of one particle

γ = mass density of the bulk material of which the particle is composed

$dn(r)$ = number of particles of radius r between r and r+dr

Substituting equation (15) in equation (36) gives:

$$dm = 4/3\pi\gamma 0.43c\ r^{(2-\nu)}dr \tag{37}$$

Integrating equation (37) over r yields:

$$m = 4/3\pi\gamma 0.434c\int_{r_1}^{r_2} r^{(2-\nu)}dr \tag{38}$$

where the limits of integration are chosen to correspond with the integration of equation (18).

Transposing equation (35) gives the desired dependence of c on m:

$$c = m(4/3\pi\gamma 0.434\int_{r_1}^{r_2} r^{(2-\nu)}dr)^{-1} \tag{39}$$

which can be evaluated explicitly for any given value of ν.

Note that the units of the quantity c depend on the value of ν as $cm^{(\nu-3)}$, and c is dimensionless for a size distribution with $\nu = 3$.

Equation (39) can now be substituted back in equation (35) to give:

$$f_s = \frac{f_o \exp(-bh)\ 0.434Al/2(2\pi/\lambda)^{\nu-2}2\pi hI_o\ m}{4/3\pi\gamma 0.434\int_{r_1}^{r_2} r^{(2-\nu)}dr} \tag{40}$$

or:

$$f_s = f_o \exp(-bh)\ K_2\ m \tag{41}$$

where:

$$K_2 = \frac{3\ A(2\pi/\lambda)^{\nu-2} h I_o}{4\ \gamma \int_{r_1}^{r} 2r^{(2-\nu)} dr} \tag{42}$$

Now that the expression for f_s as a function of m has been derived, it can be substituted along with equation (6), the expression for f_u, into equation (5) to give:

$$R = \frac{f_u}{f_s+f_u} = \frac{f_o \exp(-bh)}{f_o \exp(-bh)+f_o \exp(-bh) K_2\ m} \tag{43}$$

or on cancelling:

$$R = 1/(1+K_2 m) \tag{44}$$

Equation (44) represents the desired model equation for the ratio R; however, the relationship between R and m is hyperbolic. In order to facilitate comparisons between the model and the experimental measurements, equation (44) can be recast into a linear form with K_2 as the slope. This is accomplished by defining a new variable:

$$R' \equiv 2-(1/R) = 1-K_2 m \tag{45}$$

which decreases from unity with increasing m, as did the original variable R, except linearly and with a slope of negative K_2. In terms of experimental measurements, R'

can be expressed as:

$$R' = 2-(f_{open}/f_{pinhole}) \tag{46}$$

where equation (4) has been substituted for R, or:

$$R' = 2-\frac{f_s+f_u}{f_u} = 1 - \frac{f_s}{f_u} \tag{47}$$

where equation (5) has been substituted for R.

Equation (45) represents the relationship between the airlight variable R' and the mass concentration of the air based on the mathematical model developed in this section. It predicts a negative linear dependence of R' on m, with the restriction on the particles that they have a Jungian size distribution and assuming that the index of refraction of the aerosol will have a negligible effect on the relationship and consequently that the value of 1.5 will be representative.

Discussion of Inaccuracies in the Mathematical Model Due to Finite Size of Objective Lens

As mentioned in previous sections, the finite size of the objective lens in the optical system results in two inaccuracies in the mathematical model. These inaccuracies, however, have the effect of cancelling each other in part, resulting in a combined error that is small.

An underestimation of the flux f_s results from assuming that only those volume elements contained in the

cone shown in Figure 4 contribute to f_s. This assumption would be valid if the objective lens area were a point; however, the finite extent of the objective lens does allow volume elements from the volume, V' surrounding the cone, to make contributions to f_s also (see Figure 6). Recalling that the optical system was designed so that only light striking the objective lens at an angle of 5° or less is detected, it can be seen that all volume elements inside the cone V, and no volume elements outside the cone can scatter light toward a point located at the vertex of the cone through an angle less than or equal to 5°. With a finite objective lens, however, light does not have to be scattered toward the vertex of the cone in order to be detected; light scattered into any part of the objective lens through an angle of 5° or less is detected. Thus the volume whose elements contribute to f_s must be extended to include V'. All volume elements outside V', however, continue to make no contribution to f_s.

An overestimation of the flux f_s results from assuming that for each volume element, the scattered flux contained within the solid angle subtended at that volume element by the whole objective lens will contribute to f_s. This is an attempt to account for the finite extent of the objective lens or equivalently, for the solid angle containing the scattered flux, since the Mie solutions are

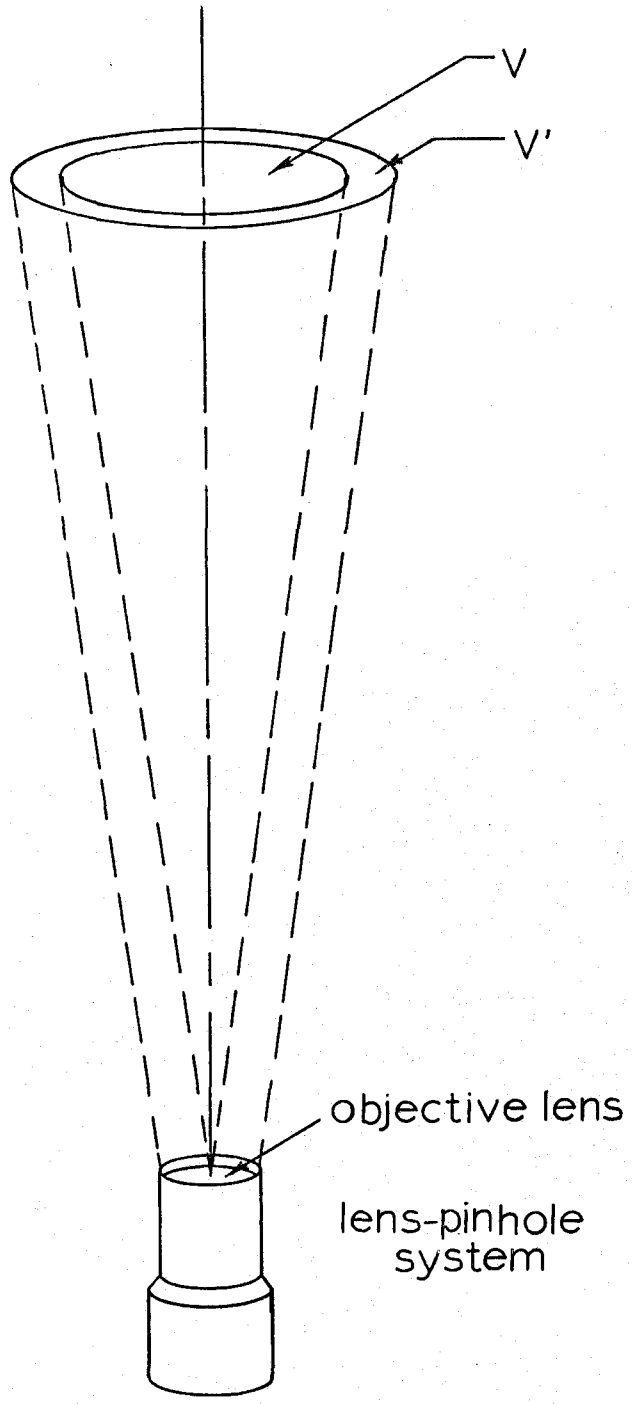

Figure 6. Extension of the volume of integration due to the finite extent of the objective lens.

expressed in terms of scattered flux per unit solid angle. If this assumption were valid, all light rays incident on any part of the objective lens after being scattered by volume elements within the conical volume V would contribute to f_s. Some of this light, however, may strike the objective lens at an angle greater than 5° depending on the location of the volume element, and actually will not be detected by the optical system.

The degree to which these two inaccuracies cancel one another can be estimated by examining the true contributions to the measured value of f_s made by volume elements at arbitrary altitudes, i.e., by comparing the assumed with the actual contributions made by volume elements at several fixed values of z, where $z = r\cos\theta$. This is illustrated in Figure 7 for an arbitrary altitude z' greater than $z = r/\tan 5°$, where r is the radius of the objective lens. According to the assumptions made in the mathematical model, the contribution made to f_s by light scattered from the volume element dV shown in Figure 7 is that flux contained in the solid angle Ω_1 subtended by the entire objective lens. Due to the limitations of the 5° acceptance angle, however, only the flux contained in the solid angle Ω_2, or equivalently, the flux striking the intersection of the objective lens and a right circular cone of half-angle 5° emanating vertically downward from

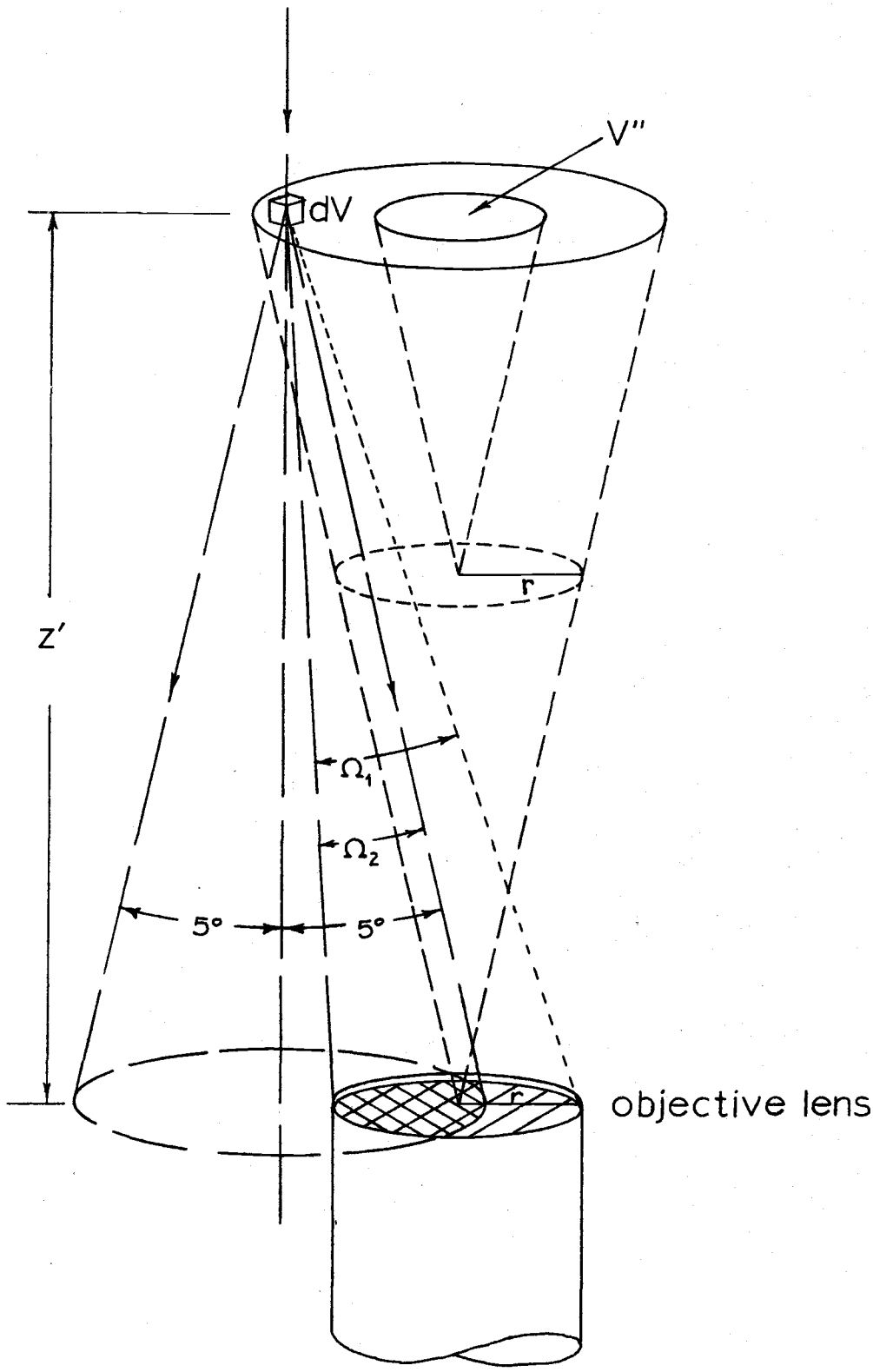

Figure 7. True contribution to f_s made by a volume element.

dV, is actually detected. This follows from the fact that all rays from dV making an angle of 5° or less with the vertical are confined to this downward 5° cone, and thus only those rays within this cone that strike the objective lens are measured. Note that for all volume elements within the conical volume V" with its vertex at the altitude $z = r/\tan 5°$ the objective lens does lie completely within the downward 5° cone and thus the assumption of the mathematical model is entirely valid. It can be seen that it is the volume elements in the region between the cones V and V" that produce the solid angle errors. For every volume element dV in this region, however, there exists a volume element dV' (in the volume V' surrounding the cone V) in the same horizontal plane as dV, diametrically opposite dV and located outside the perimeter of cone V a distance equal to the distance that dV is inside the perimeter of cone V, such that the intersection, A_1, of its downward 5° cone and the objective lens is tangent to the intersection, A_2, of the objective lens and the downward 5° cone from the volume element dV (see Figure 8). The result is that the surface of the objective lens still is not completely covered by detectable contributions to f_s from dV as assumed in the mathematical model, but the actual area covered, A_1, is supplemented by detectable light from dV' striking A_2, and the sum of A_1 and

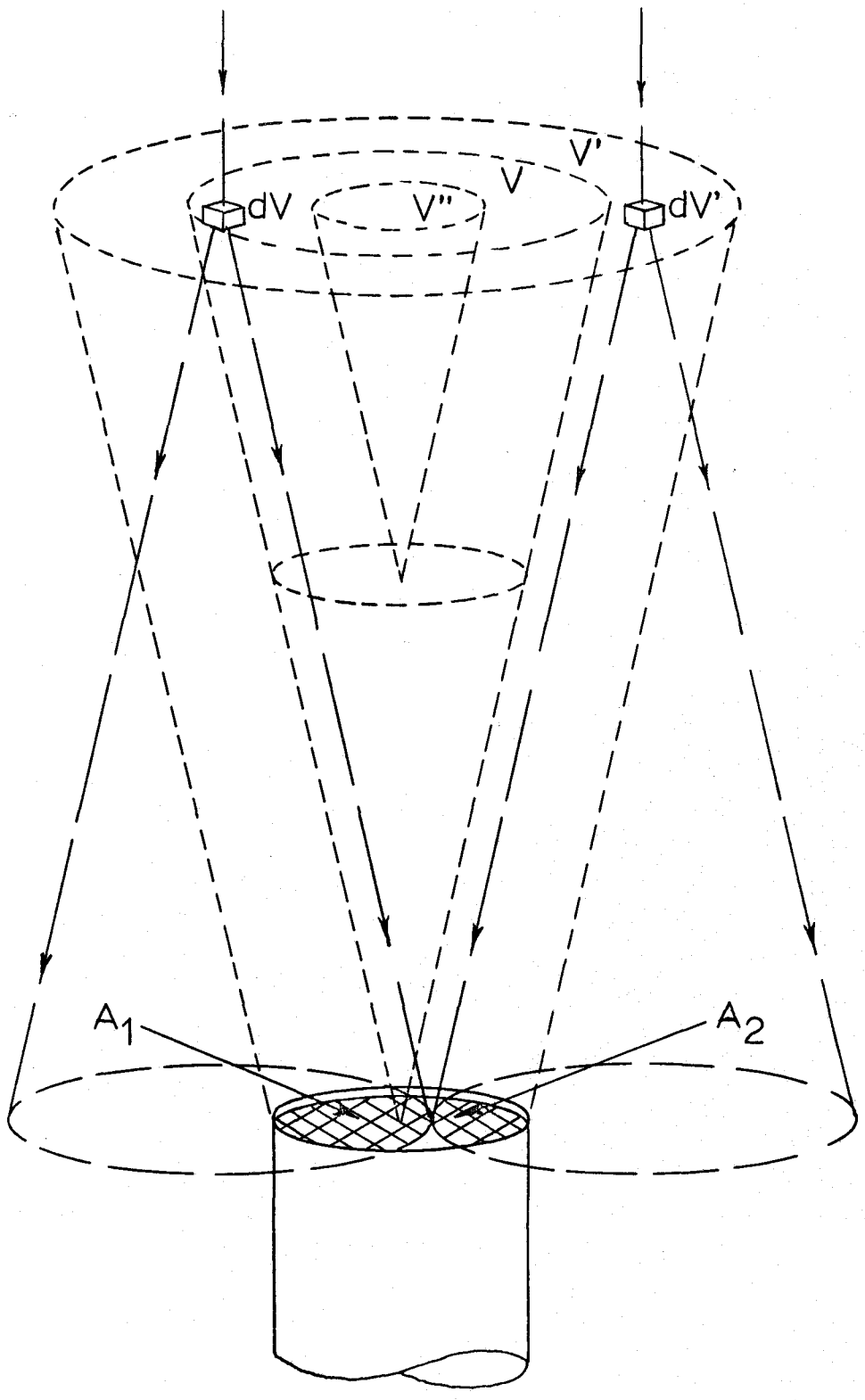

Figure 8. Combination of over- and under-estimated light fluxes.

A_2 approaches complete coverage as z increases. Thus, two conclusions are reached: (1) the solid angle error does not result from all of the volume elements and, in fact, the region from which the error causing elements come, becomes a smaller fraction of the total volume as z increases, and (2) for every volume element for which such an error results, there exists another volume element, not considered by the mathematical model, that partially compensates for the error, and this compensation becomes more complete also as z increases. As an indication of the degree of compensation, Figure 9 shows a plot of the fraction of the objective lens receiving contributions to f_s from a volume element just inside the perimeter of volume V at an altitude z and from its companion element in volume V' versus the altitude z, i.e., $(A_1 + A_2)/A_{obj}$ vs z. It can be seen that the mathematical model is in error by approximately 50% in estimating the contributions to f_s by volume elements inside V but outside V" at the altitude z = 11.5 cm, but only about 10% for volume elements at z = 40 cm. At first glance, this does not appear to be negligible; however, noting that the volume of a cone of fixed vertex angle increases as the cube of its altitude, it can be seen that the volume elements for which the mathematical model is most in error (those near the vertex of the cone V) make up only a very small per-

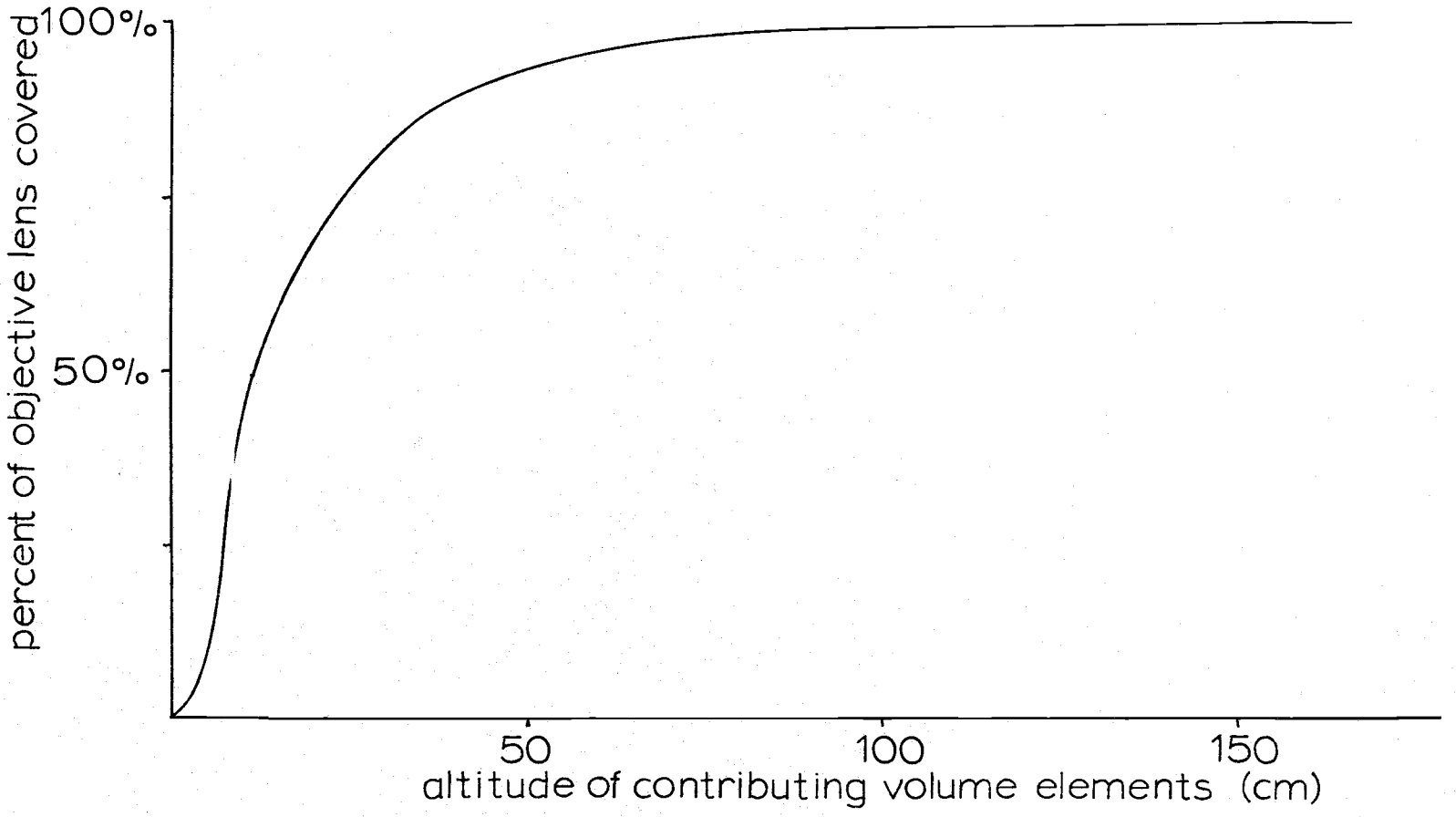

Figure 9. Degree of cancellation of over- and under-estimation of light flux.

centage of the total volume. Thus, since the altitude of the cone V in this experiment is 178 cm, for 99.97% of the total volume, the mathematical model is in error less than 50%; for 98.84% of the volume, the error is less than 10%; and for 91.08% of the volume, the error is less than 0.2%. Since the mathematical model is not in error at all for volume elements in V", 73.75% of the volume has zero error. These numbers are illustrated graphically in Figure 10.

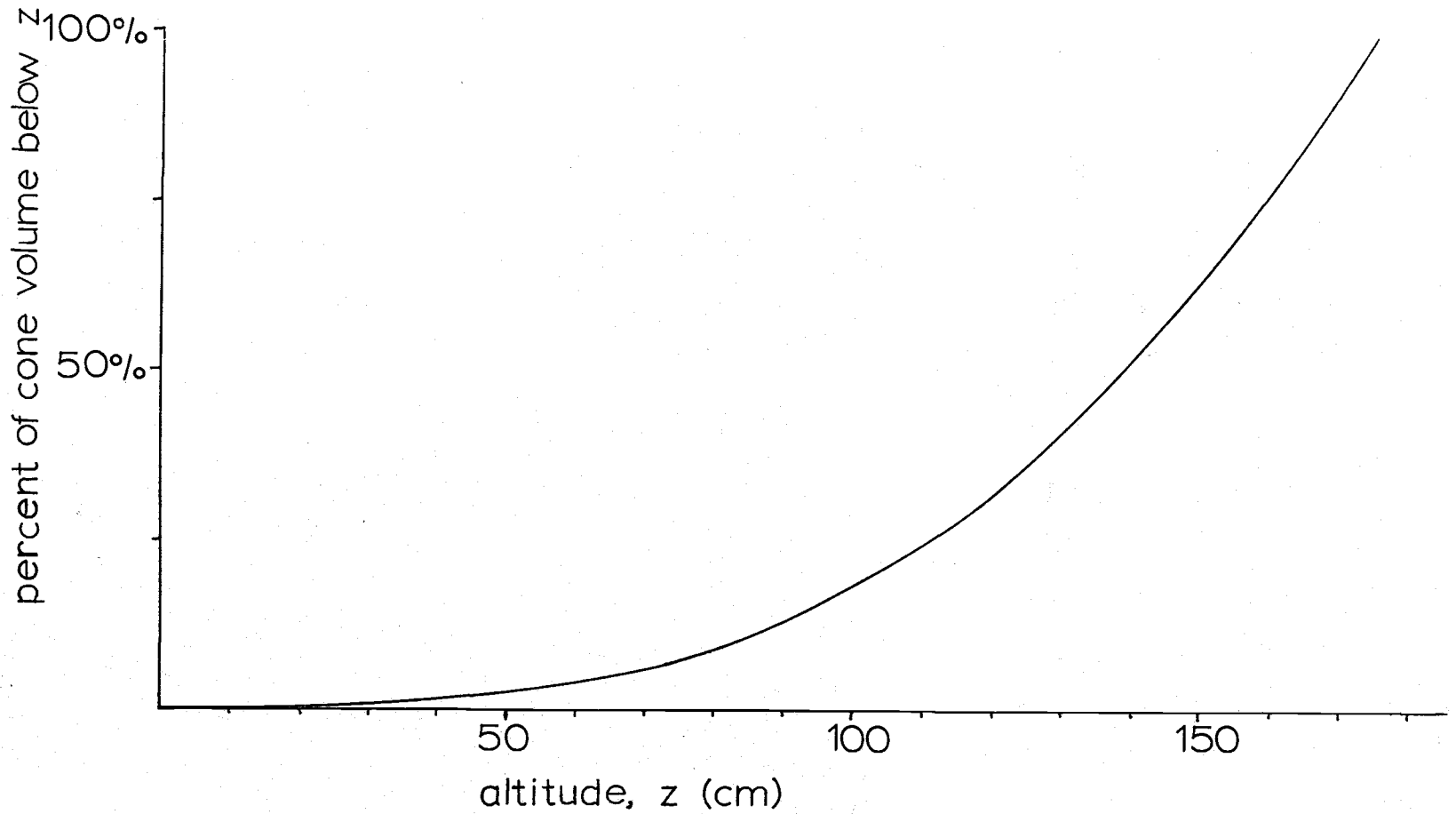

Figure 10. Percentage of volume of integration below a given altitude as a function of altitude.

IV. METHODOLOGY

Experimental Design

The design of the experiment was very simple and consisted of simultaneous R and m measurements for varying values of m for a given aerosol, i.e., a given index of refraction and size distribution. This process was carried out for nine different aerosols--three different size distributions for each of three indices of refraction. Each size distribution is characterized by the mean diameter. Regression analyses were then performed to determine the least-squares curves that provided the best fit for each of the nine sets of data points and also the correlation coefficients and indices of determination.

The three aerosol materials used in this experiment were potassium chloride, sodium chloride and ammonium chloride. These three compounds were selected because they are very similar in their light scattering properties except that their indices of refraction are different. They all have identical crystal structures (cubic), they are all colorless, and they are all transparent. The indices of refraction for KCl, NaCl, and NH_4Cl, are 1.49, 1.54, and 1.64, respectively. Thus the variations in the experimental measurements due to particle shape and light absorption

(color) were eliminated leaving only the variations due to index of refraction and particle size. A final consideration that was made in the selection of these compounds was their solubility in water. The method of generating the aerosols in this experiment (see Experimental Apparatus in this section) requires that the aerosol material be soluble enough to make at least a 20% by weight solution in water at room temperature. The different aerosol size distributions are determined by the concentration of this solution.

Experimental Procedure

In order to maintain control over the experimental variables, the experiment was performed in an airtight aerosol chamber (see Experimental Apparatus). The measurements were made by first purging the aerosol chamber with air that had been filtered and desiccated, and then charging the chamber with an aerosol of a given index of refraction and size distribution. A fan located inside the chamber was switched on for fifteen seconds to mix the aerosol with the chamber air, and insure a uniform concentration. Five minutes was allowed for spurious and unusually large particles to settle out and for equilibrium to be established. The collimated light source was then switched on at the upper end of the aerosol chamber. The light fluxes in the

open and closed positions of diaphragm were then measured at the lower end, and the light switched off. The mass loading, m, of the test atmosphere was then measured with the Sinclair-Phoenix aerosol photometer.

The chamber was again charged with the same aerosol, i.e., more of the same aerosol was added to "old" aerosol, to increase the concentration. This was again mixed with the fan and allowed to stand for five minutes. The light fluxes and m were then measured again using the same procedure as in the first measurement.

The process of recharging and measuring the light fluxes and m was repeated until the concentration in the chamber approached the upper limit of the Sinclair-Phoenix photometer.

Similar experimental runs were performed for each of the remaining eight aerosols.

The purge air is filtered for the obvious reason of providing a clean background for the test aerosol. It is desicated to allow the test aerosol to exist in a dry, solid state, with fixed diameters and indices of refraction. Junge (1958), Bullrich (1964), and Charlson (1968) have concluded that soluble aerosols can exhibit deliquescent behavior when the relative humidity is approximately 70% or greater, resulting in a growth of the particles by the absorption of water from the atmosphere and a reduction of the index of refraction toward the value

for water (1.33).

Experimental Apparatus

Aerosol Chamber. The aerosol chamber (Figure 11) consisted of a 3/8" plywood enclosure with inside dimensions of 23.5"x23.5"x70.25". The chamber was sealed at the seams with GE-RTV silicon seal, and at the door, with 1/8" foam insulation. All interior surfaces were painted with flat black latex to minimize reflections. A 16"x18"x20" expansion chamber of collapsable polyethylene was provided to allow the removal of air for sampling without the necessity of introducing replacement air which would alter the aerosol concentration. A nine-inch diameter four-blade fan was located in an upper corner of the main chamber to mix the test atmosphere to insure a uniform aerosol concentration within the chamber. The temperature and relative humidity inside the chamber were measured by means of a Weston model 4300 dial thermometer and a Frieze hair hygrometer respectively. The hygrometer was first calibrated against a sling psychrometer and psychrometric chart before installation. The relative humidity readings were made through a two inch square glass window in the chamber wall which was also sealed with GE RTV silicon seal. Stray light was prevented from entering the chamber through the window by a hinged opaque cover on the outside,

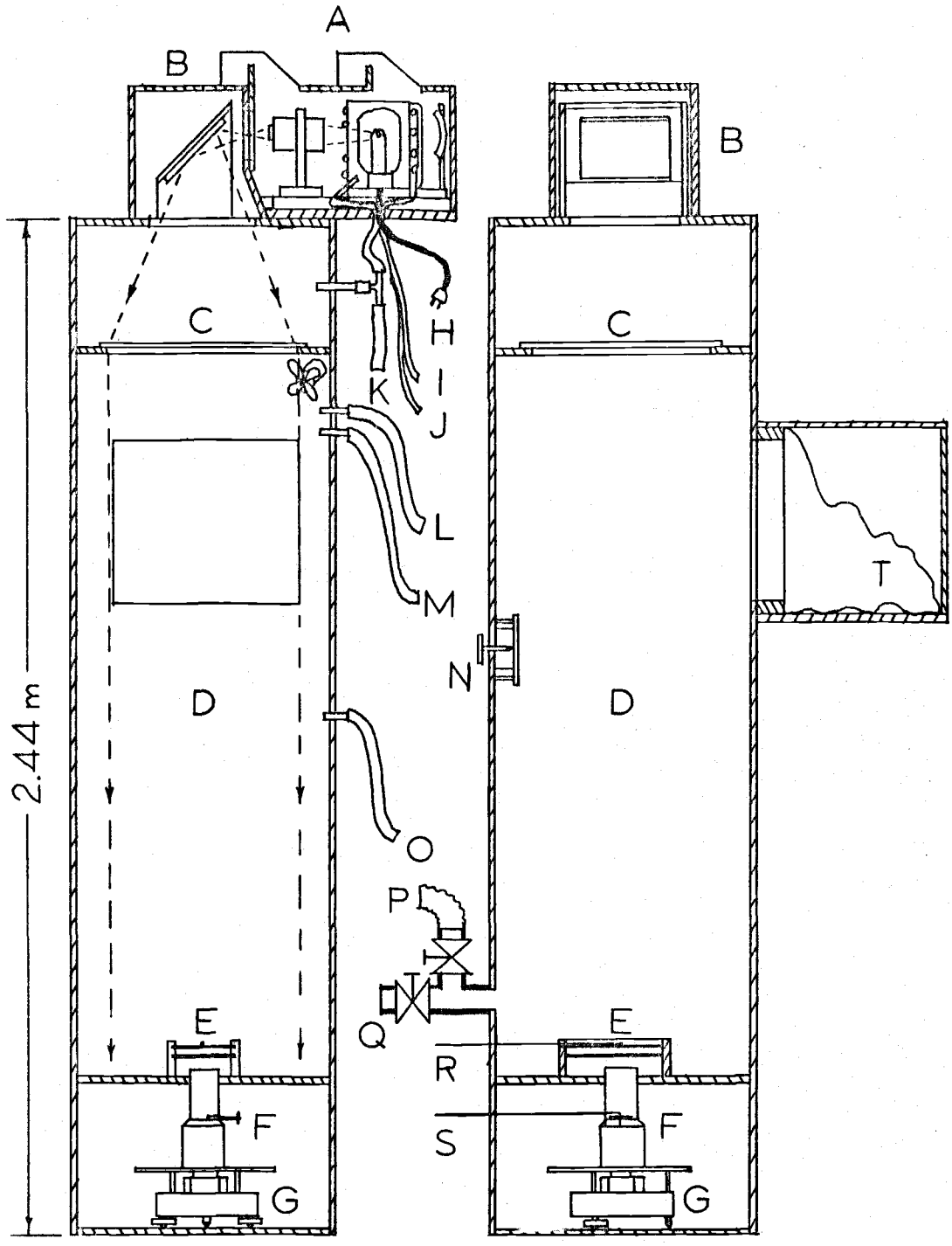

Figure 11. Aerosol chamber (Legend on following page).

Legend for Figure 11

A	Light source
B	Front surface plane mirror
C	Fresnei lens
D	Test chamber
E	I-R filter and dust cover
F	Optical system
G	Pyranometer
H	Light source power
I	Cooling water, in
J	Cooling water, out
K	Cooling air, in
L	Purge air, in
M	Aerosol, in
N	Thermometer and hygrometer
O	Sinclair-Phoenix sample, out
P	Main exhaust
Q	Purge exhaust
R	Dust cover control rod
S	Iris diaphragm control rod
T	Collapsable expansion chamber

and a 3/8" plywood screen behind the hygrometer on the inside.

Purge air and aerosol charging inlets, and sampling outlets were 3/8" tygon tubing connected to short lengths of copper tubing that passed through the chamber wall through Swage-Lok fittings.

Air was exhausted from the chamber during the purging process through standard 1/2" pipe fittings and valve located at the bottom of the chamber. During the clearing-out procedure between runs of different aerosols, a Pullman industrial vacuum cleaner was used to exhaust the chamber through standard 1" pipe fittings and valve also located at the bottom of the chamber.

Light Source. The light source was a 1000 watt incandescent projection bulb with a square array of tungsten coil filaments one centimeter on a side. In order to minimize intensity fluctuations due to line voltage fluctuations, current to the bulb was supplied by a 1000 volt-amp Sola harmonic neutralized constant voltage transformer. In order to dissipate the heat generated by the bulb, a continuous flow of air was maintained around the bulb and the bulb was enclosed laterally by a sheet brass, water-cooled jacket. The system is shown in Figure 12. A two-inch diameter front surface spherical mirror was positioned behind the bulb so that the filament fell in the focal

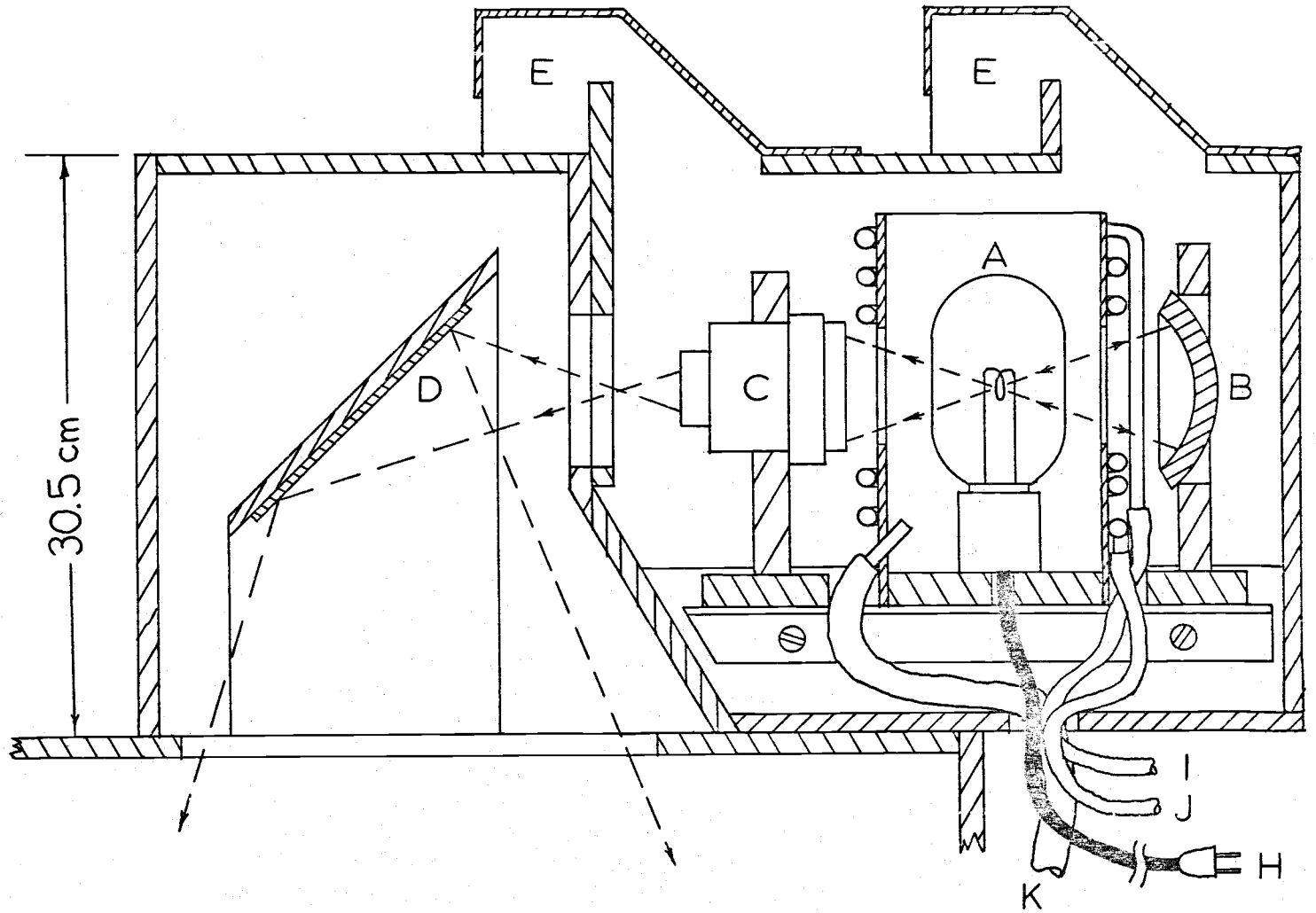

Figure 12. Light source (Legend on following page).

Legend for Figure 12

A	Light bulb
B	Spherical mirror
C	Condensing lens
D	Plane mirror
E	Exhaust louvers
H	Power
I	Cooling water, in
J	Cooling water, out
K	Cooling air, in

plane of the mirror. This effectively doubled the intensity of the light in the forward direction, which passed through a hole in the cooling jacket, and then through a condensing lens system that produced an areal reduction of approximately 45% in the filament image. The horizontal beam diverging from the image was reflected downward in a vertical direction by a 5"x7" plane front surface mirror oriented at a 45° angle. An 18-1/4" diameter collimating Fresnel lens located so that the filament image was at its focal point produced a parallel beam of light directed along the vertical axis of the aerosol chamber. The alignment of the beam with the axis of the aerosol chamber was accomplished by adjusting the position and angle of the reflecting mirror so that the spot of light created by the beam on the aerosol chamber floor was centered on the R measuring system located at the center of the floor. The collimation of the beam was adjusted by moving the condensing lens system and the light source along the horizontal track until a twelve-inch steel scale held in the vertical beam perpendicular to its axis at the upper part of the chamber cast the sharpest and most accurately sized shadow on the chamber floor. This was determined by placing a similar scale on the floor and making adjustments until the shadow of the upper scale coincided with the scale on the floor.

The entire light source system was enclosed in a 3/8" plywood cover to prevent any extraneous light from entering the aerosol chamber. All of the interior surfaces of the light source enclosure were also painted flat black to prevent reflections.

R' Measurement System. The R' measurement system (Figure 13) consisted of three components: (1) the infra-red filter and dust cover assembly, (2) the optical system and (3) the sensing device.

The filter-dust cover assembly was essentially a holder for an Oriel 2"x2" infra-red cutoff filter with a sliding dust cover that could be operated from outside of the aerosol chamber by means of a 1/32" diameter steel rod. The cover was kept closed between measurements to prevent undue deposition of the aerosol on the filter. The rod passed through the chamber wall through a rubber gasket and a sliding-fit copper tube held in place by a Swage-Lok fitting. The rod was lubricated with silicon vacuum grease. The infra-red cutoff filter was used to bring the incandescent spectrum of the projection bulb into closer conformity with the solar spectrum.

The optical system was essentially the lens-iris diaphragm system described in the preceding section, with the addition of an aspheric condensing lens system following the iris diaphragm to condense the diverging rays into

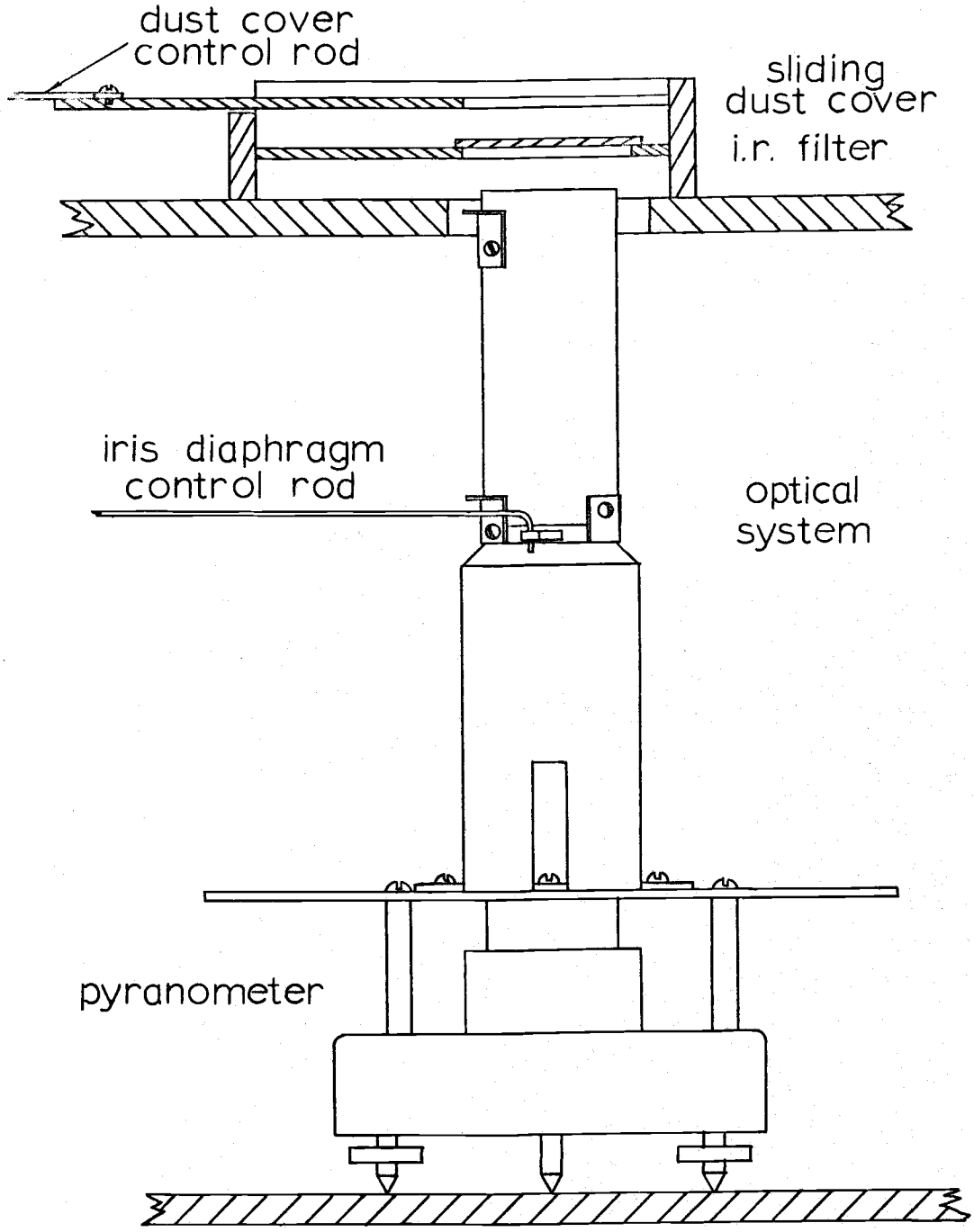

Figure 13. R' measurement system.

a beam with a small enough cross section to be completely detected by the sensing element. The objective lens was actually a compound lens made up of two 50 mm diameter binocular objective lenses with a combined focal length of 100 mm. The optical system was mounted in a two-piece, machined aluminum barrel as shown in Figure 14, with all of the inside surfaces painted flat black to minimize internal reflections. Allen head set screws were used to hold the retainer rings in place and to hold the two sections of the barrel together. The brass alignment guides were similar to those found on the Volz sun photometer, and provided a quick means of aligning the optical axis of the lens-diaphragm system with the axis of the incoming light beam, i.e., so that the parallel light rays did indeed focus within the pinhole. The guides themselves were two sheet brass plates mounted at right angles to the axis on the exterior of the front barrel section. The front plate had a 1/16" hole drilled through it while the back plate had a slightly smaller spot inked onto it. The hole and the spot were positioned so that when the optical system was aligned with the light beam, the light passing through the hole created a spot of light centered on the ink spot. The alignment of the hole and spot was initially set on an optical bench with a collimated light source. This was accomplished by placing the forward barrel section on the optical bench, aimed at the light source. A circular piece of translucent

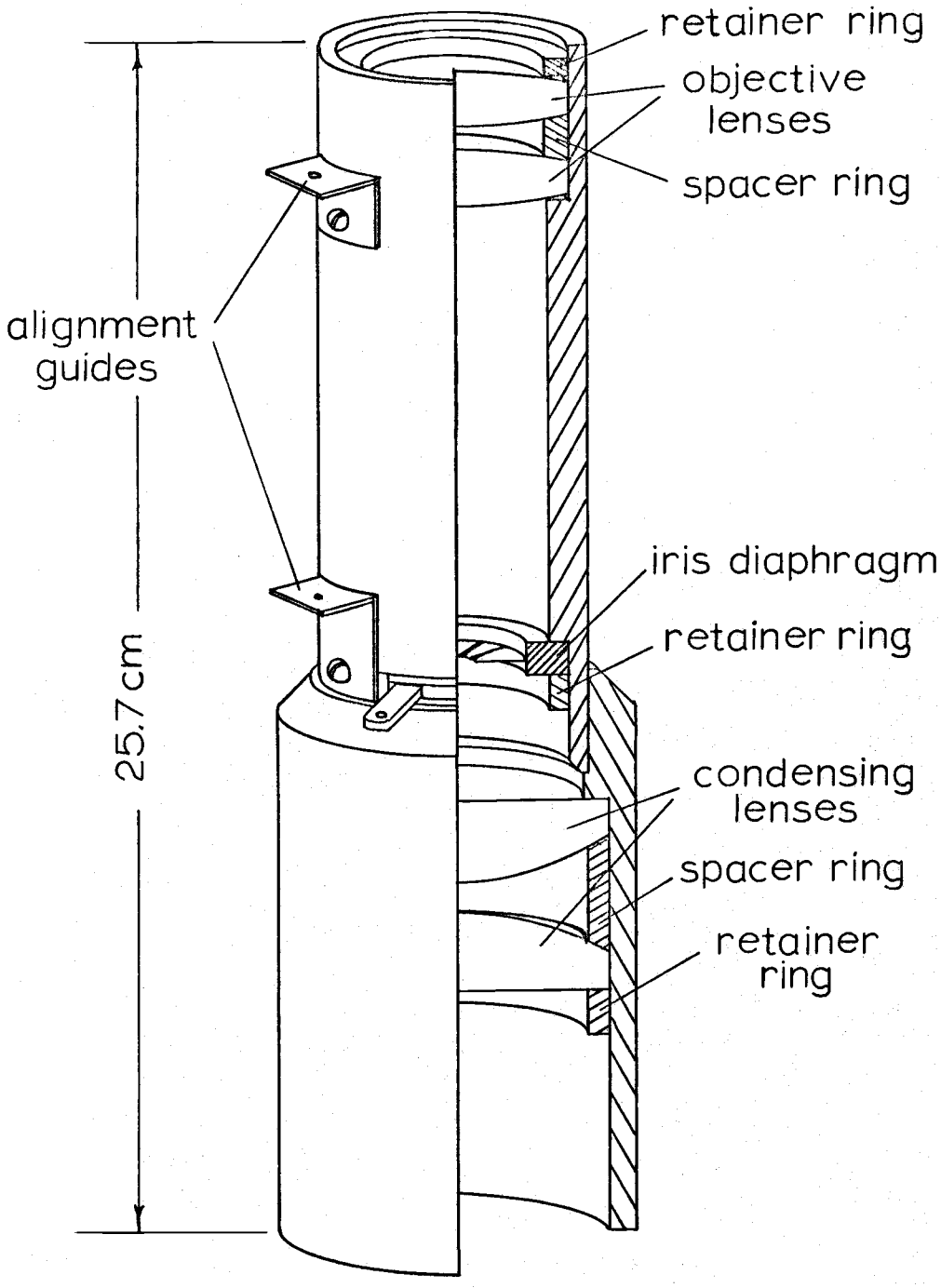

Figure 14. Optical system.

paper was placed against the diaphragm leaves to act as a screen on which the point of focused light could be seen from the back. When this point of light fell exactly in the center of the pinhole, the ink spot was marked onto the back brass plate in the center of the spot of light.

The back plate also acted as a positive stop for the diaphragm lever corresponding to a 5° acceptance angle for incoming light. This setting was also made on the optical bench with a collimated light source. The barrel was mounted this time, however, on the rotating table of a surveying transit. With the paper screen in place on the diaphragm leaves, the optical system was aligned with the light beam again by centering the point of focused light in the pinhole. The diaphragm aperture was then opened up and the transit table rotated through a horizontal angle of 5° as indicated on the vernier scale of the transit. The diaphragm was then closed down until the leaves just touched the point of light which was now off center by a distance $x = 100 \text{ mm} \tan 5°$ according to equation 3. As a check on symmetry, the table was rotated also 5° in the opposite direction from the original position, and when the point of light just touched the diaphragm leaves on the opposite side of the aperture, then the brass stop was secured against the diaphragm lever in this position.

The diaphragm lever was operated during the experiment by means of a 1/32" steel rod, with one end hooked through a hole drilled at the end of the lever, passing through the aerosol chamber wall through a rubber gasket and a sliding fit copper tube held in place by a Swage-Lok fitting.

The light sensing device in this experiment was a Kipp-Zonen pyranometer, a standard solar radiation measuring instrument used in meteorology (Hewson, 1968). This instrument consists of a fourteen junction manganin-constantan thermopile that has the "hot" junctions imbedded in flat plate which is painted black and exposed to the solar radiation. The "cold" junctions are located on the underside of the instrument and are encased in a massive brass enclosure to prevent exposure to sudden variations in temperature due to winds and variations due to the effects of the solar radiation. The "hot" junctions are sealed from the ambient air by two concentric hemispherical glass domes. The incident solar radiation is absorbed by the black surface and creates a temperature difference between the "hot" and "cold" junctions, resulting in a potential difference at the two leads proportional to the light flux.

The optical system was seated on the pyranometer on a specially constructed platform of 1/8" steel that was attached to the pyranometer base. It was centered and held in place by three adjustable brackets. The platform was

constructed of 1/8" steel to provide a rigid base for the optical system that would not allow it to rock while the diaphragm lever was being operated.

The alignment of the optical system with the light beam inside of the aerosol chamber was accomplished by means of the leveling screws that make up two points of the three point base on the pyranometer. With the collimated light beam turned on, the system was roughly aligned by using the external brass alignment guides, and then more precisely, by obtaining the maximum reading from the pyranometer while the diaphragm was in the pinhole position.

Aerosol Generator and Air Supply. The aerosol generation system consisted of a DeVilbiss nebulizer, and an air filtration system. The nebulizer (Figure 15) is essentially a liquid atomizer that transforms a liquid into a fine mist. The nebulizer can be used as a generator of a solid aerosol by atomizing a solution of the desired solid dissolved in water. When the mist enters a dry atmosphere, the water evaporates leaving an aerosol of solid particles. The index of refraction of a test aerosol generated by this method is determined by the choice of the solute used in the nebulizer solution.

The mean particle diameter for the solid aerosol is determined by the concentration of the solute in the nebulizer solution. Studies have shown (Lauterbach, et al.,

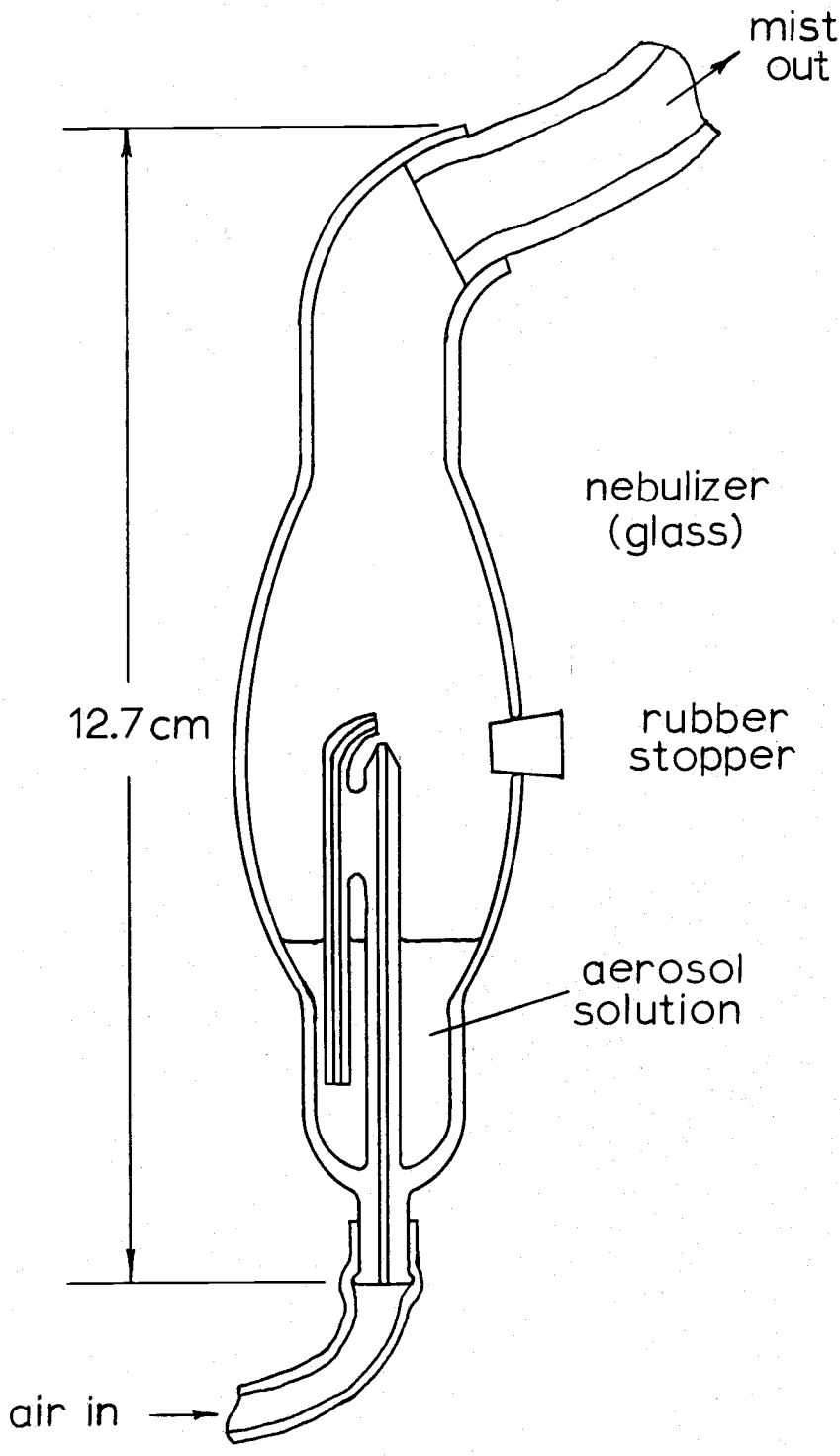

Figure 15. Aerosol generator.

1956 and Mercer, et al., 1963) that the mean particle diameter is a direct function of the solution concentration, and moreover, it has been shown by Mercer, et al., that the other two parameters, the nozzle size and the air pressure or flowrate, while having a significant effect on the total output of the atomizer, have only a minor effect on the aerosol size distribution. In this investigation, these minor effects were eliminated maintaining a constant air pressure of 18 psi through a fixed nozzle, and the mean aerosol diameter was varied by varying the concentration of the nebulizer solution.

The air supply for the nebulizer was first filtered to prevent any aerosols present in the air from contaminating the test aerosol. The filtration system is shown in Figure 16. Compressed air from the laboratory wall outlet first passed through a liquid trap and then a pressure regulator. The air then passed through a two-inch i.d.packed-tube filter containing fourteen inches of glass fiber wool followed by fourteen inches of calcium sulfate granules. The calcium sulfate is a desiccant used to absorb water vapor from the air stream. The desiccant was followed by three more inches of glass fiber wool and a wire screen to prevent particles of the desiccant from being entrained in the air stream. This packed-tube filter was followed by a similar filter but smaller in size, made of glass tubing and filled with an indicating calcium sulfate desiccant

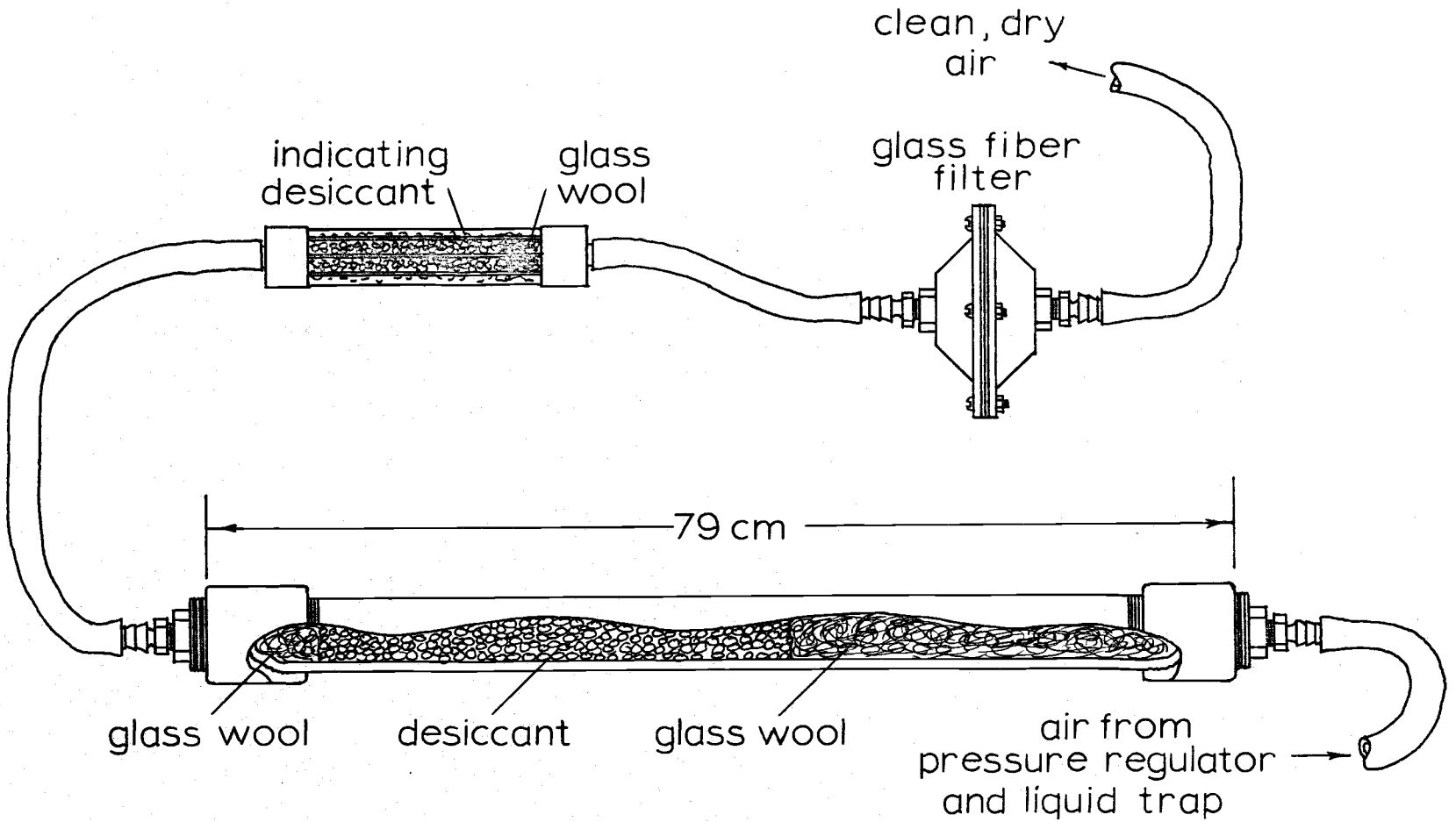

Figure 16. Air filtration system.

that gradually changed color as it becomes saturated. This served as an indicator showing the effectiveness of the main body of desiccant which loses efficiency as it absorbs water. The final filter was a four and one-half inch diameter glass fiber filter (Gelman type A) that has a collection efficiency of over 99% for particles as small as 0.3 microns in diameter (Rossano, 1969).

The purpose of the desiccant was to provide dry air for the aerosol chamber. The filtration system described above conditioned air not only for the aerosol generator but also for the purging of the aerosol chamber prior to the experimental runs and thus the filtration and the desiccation were both included in the same system. Dry air was necessary in the aerosol chamber for two reasons. First, it was necessary to eliminate deliquescence in the test aerosols whereby the aerosol particles increase in mass and size, and undergo a change in their index of refraction due to their absorption of water. The commonly used value of relative humidity below which deliquescence may be neglected is 70% (Bullrich, 1964; Charlson, 1968; California Ambient Air Quality Standards, 1973), this assumption is supported by the investigation of Lundgren and Cooper (1969). Relative humidities between 35% and 40% were achieved with the system described above. The second reason for the desiccation of the chamber air was to provide the dry atmosphere necessary to evaporate the water from the mist

the Sinclair-Phoenix photometer. The entire sample was passed through a membrane filter (Gelman Metricel GA-4) which was placed in the sample flow line in a filter holder provided for this purpose. The filter was weighed before and after sampling to obtain the mass of the particulate contained in the sample. From this mass and the sampling flowrate and time, the mass concentration in the sample was calculated. The photometer scale reading corresponding to this mass concentration was converted to a value proportional to the mass concentration by means of the calibration curve supplied with the instrument. Since the proportional scale is linear with respect to the mass concentration, and now the mass concentration corresponding to two points on the scale was known (the one just found and zero mass concentration at zero scale reading), the calibration of the proportional scale was complete and any subsequent photometer readings made on the same aerosol could be converted to mass concentration. The same procedure was followed for each of the remaining eight aerosols.

In order to determine the average photometer reading from the instantaneous variations, the output was fed into a strip chart recorder.

The light sensing instrumentation consisted of a Tektronix Type 1A7A High Gain Differential Amplifier with

droplets from the nebulizer in the formation of the solid aerosol particles. This evaporation had the effect of increasing the relative humidity of the air in the aerosol chamber to a maximum value of approximately 45% over one experimental run.

Instrumentation. The instrumentation for this experiment fell into two groups: (1) that used to measure the aerosol mass concentration and (2) that used to amplify and measure the signal from the light sensing system.

A Sinclair-Phoenix aerosol photometer was used to measure the aerosol mass concentration inside the aerosol chamber. The Sinclair-Phoenix aerosol photometer, a light scattering instrument, is described in principle in section II, but since light scattering is dependent on the physical characteristics of the aerosol, such as size, shape, and index of refraction, it was necessary to calibrate the instrument for each specific aerosol. The instrumental scale readings, however, are not proportional to the mass loading and a non-linear calibration curve is supplied with the instrument that relates the instrument scale to one that is proportional to the mass loading. This second scale is calibrated by the user for specific aerosols. The calibration was accomplished in this experiment by charging the aerosol chamber with one of the nine aerosols and sampling this atmosphere for ten minutes with

a Tektronix Type 133 plug-in power supply, and a strip chart recorder. The optical system and the light sensor is described in the preceding section. The signal of about 0.15 millivots from the pyranometer was amplified to register approximately three-quarter scale on the 1 volt full scale strip chart recorder, i.e., about a 5K amplification.

V. DATA ANALYSIS AND RESULTS

R and R' Measurements

The measured light flux signals from the pyranometer were amplified and recorded on strip charts. Due to amplifier drift and line voltage variations, three measurements of the ratio R were made for each value of m. A typical trace is shown in Figure 17. The first plateau represents light flux measured with the optical system diaphragm in the pinhole position. The second plateau represents the flux measured with the diaphragm in the open or 5° acceptance angle position. The third and fourth plateaus represent the same measurements as in the first and second plateaus except they were made with the amplifier in the DC offset mode. In this mode, the amplifier output is offset in such a manner that the baseline on the strip chart corresponds to an input voltage higher than zero, i.e., the strip chart pen is activated only when the input voltage reaches a predetermined value. Thus, since only the upper part of a trace is recorded, the amplification can be increased and still have the trace fit on the chart. The third and fourth plateaus therefore are repeat measurements of the first and second plateaus but showing only the upper portions and amplified by a factor of five.

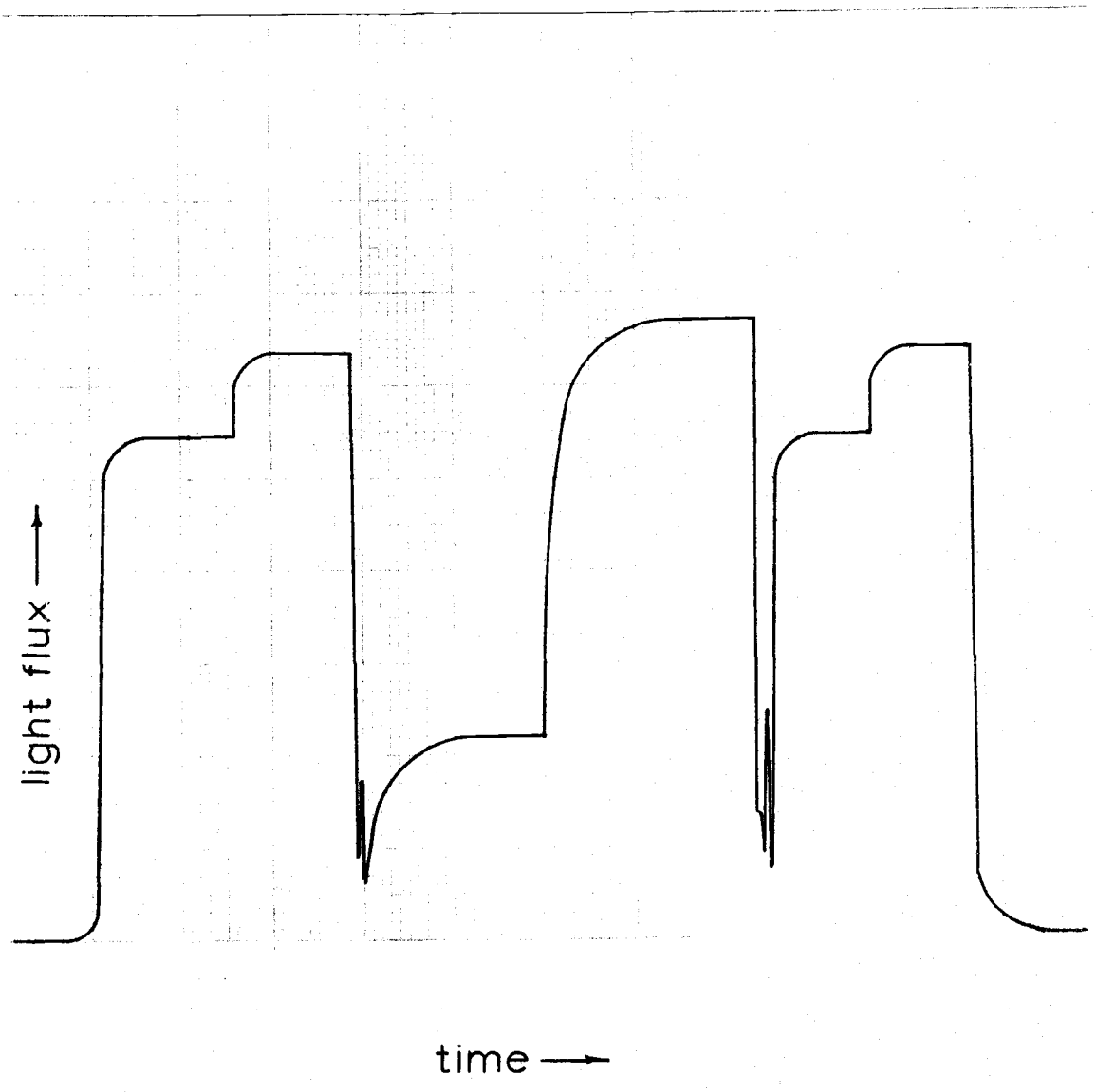

Figure 17. Strip chart trace of pyranometer output.

The fifth and sixth plateaus are a repeat of the first and second full trace measurements. When agreement was reached between the higher resolution offset trace and at least one of the two full traces on the difference between the plateaus (agreement within 0.03 units when full scale represented 10.0 units) then the observation was considered acceptable. A total of 30 observations out of 195 were rejected using this criterion.

Since the output voltage from the pyranometer is proportional to the light flux striking the sensor, the results, expressed as the ratio R, were calculated by dividing the height or voltage of the lower plateau by that of the higher plateau. R' was calculated by substituting these values of R into equation (45). Graphs of the ratio R' as a function of m for the nine experimental runs are presented in Figures 18 through 26. The curves that are shown represent the linear least squares regression lines for the data points with m greater than 1.0 micrograms/liter. The reason for the omission of the data points below 0.001 milligrams/liter are discussed in section VI. Table V lists the constants for the linear regression equations as obtained by least squares analysis and also the correlation coefficients for each regression line and its data points. Appendix A lists all of the experimental R vs m data points along with the temperature and relative humidity. Appendix B lists all of the experimental R' vs

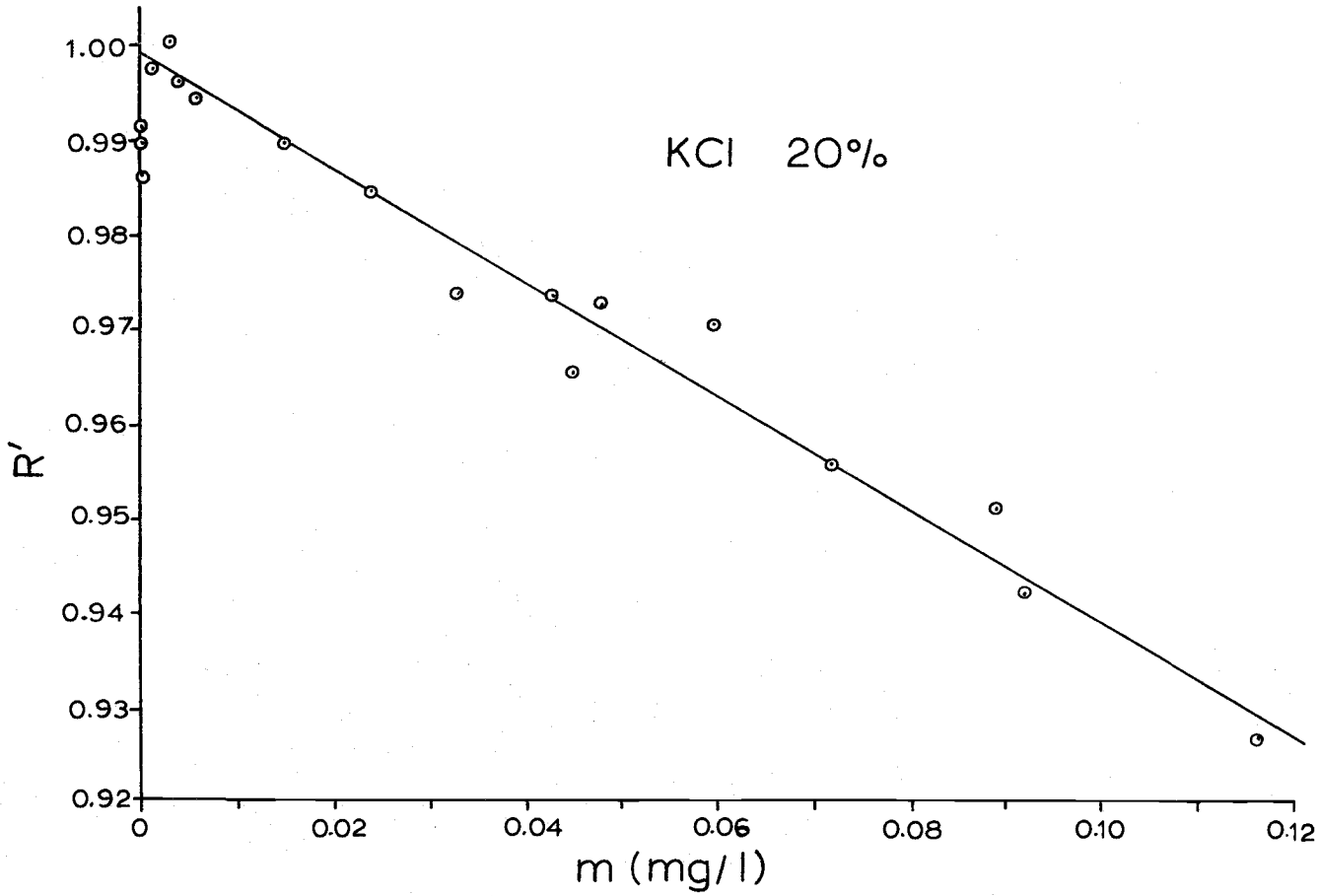

Figure 18. Plot of experimental data for KCl 20%.

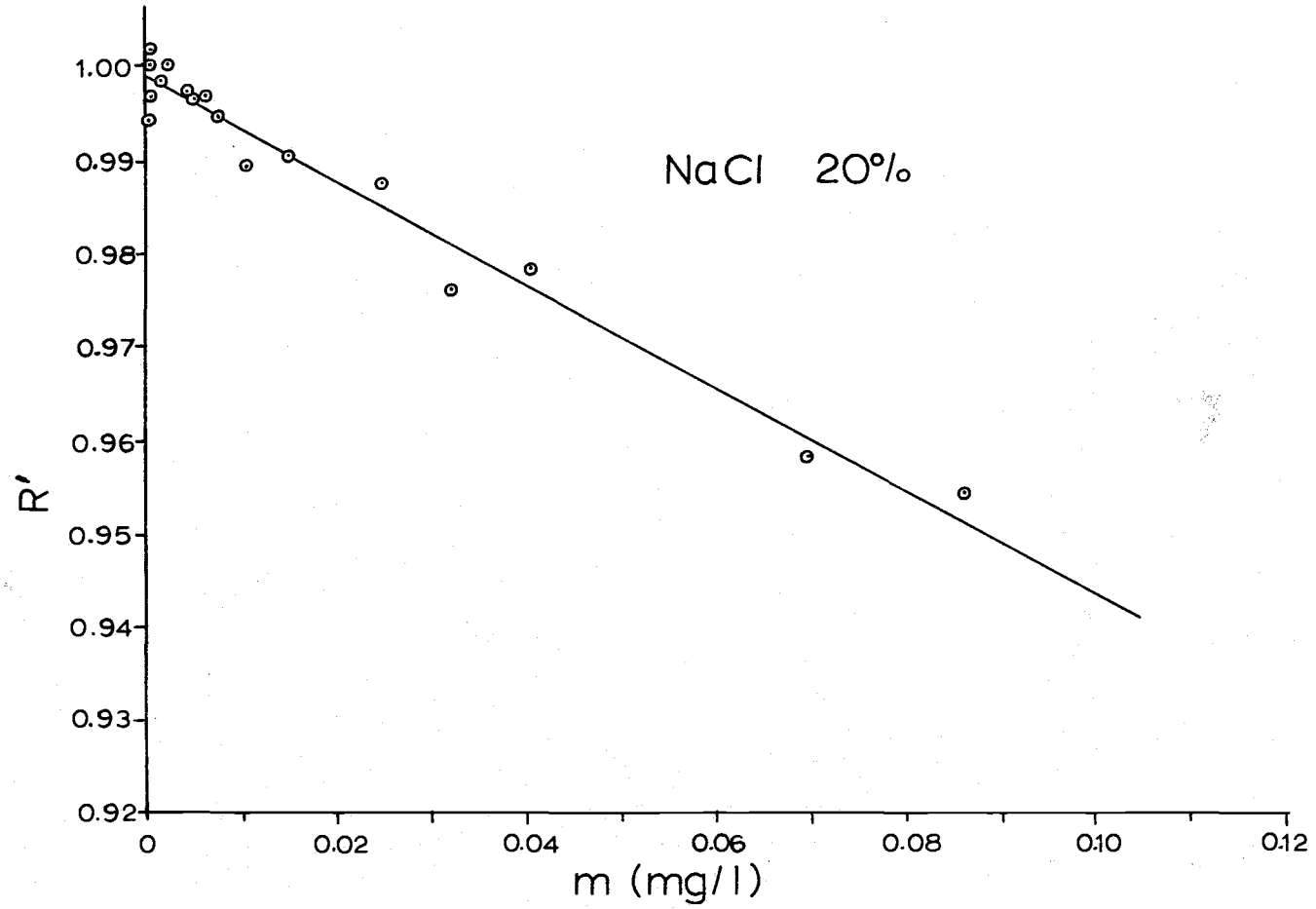

Figure 19. Plot of experimental data for NaCl 20%.

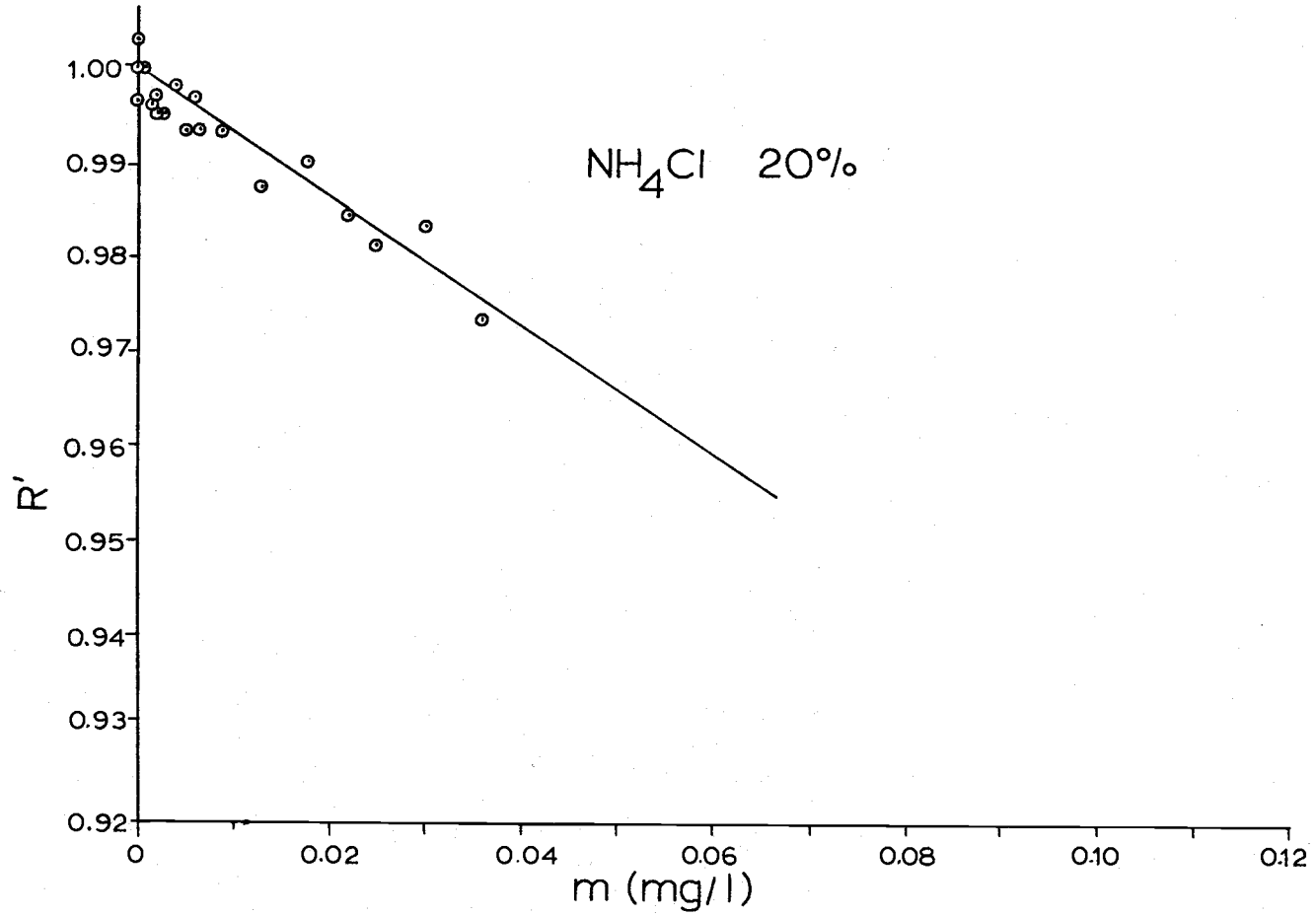

Figure 20. Plot of experimental data for NH_4Cl 20%.

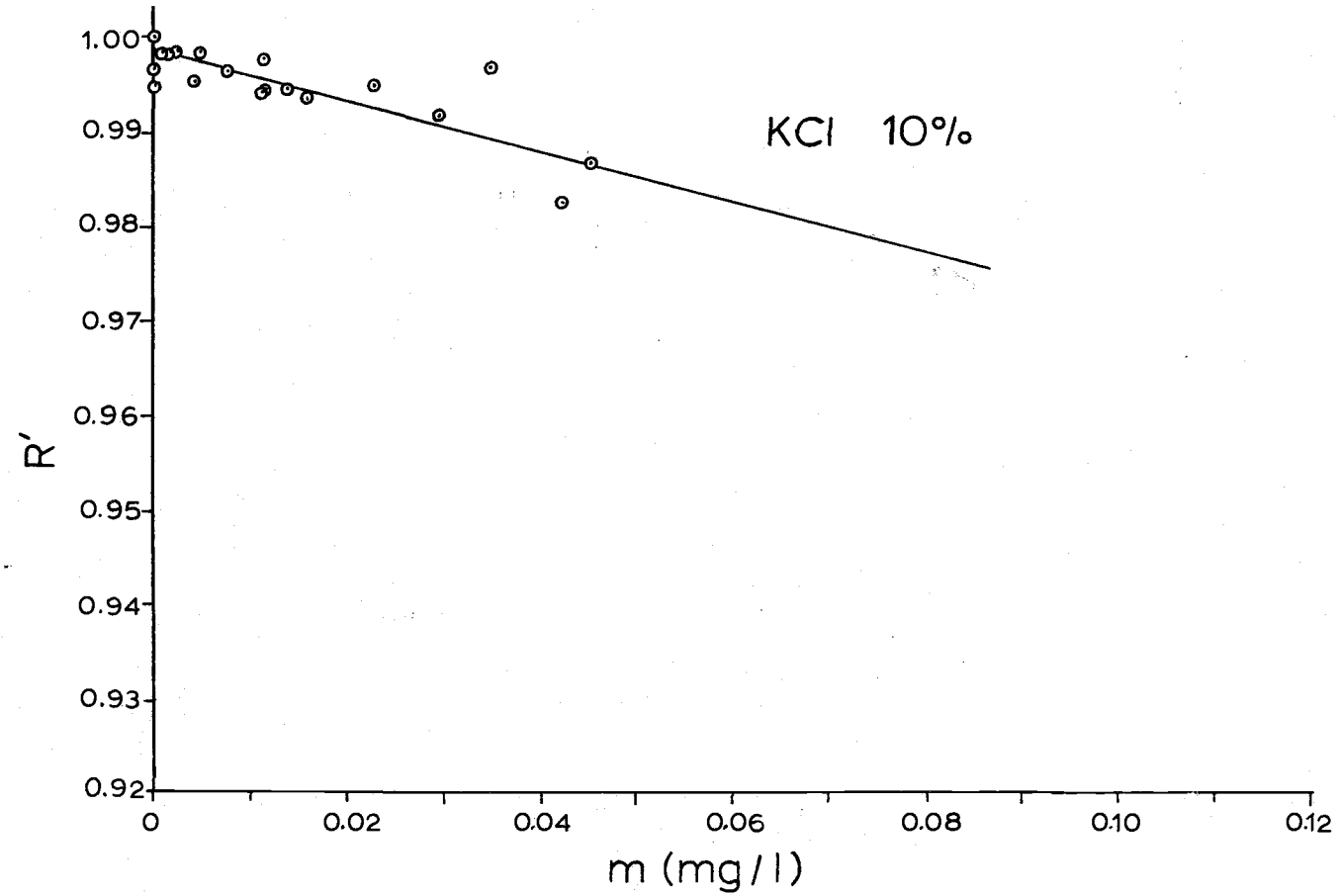

Figure 21. Plot of experimental data for KCl 10%.

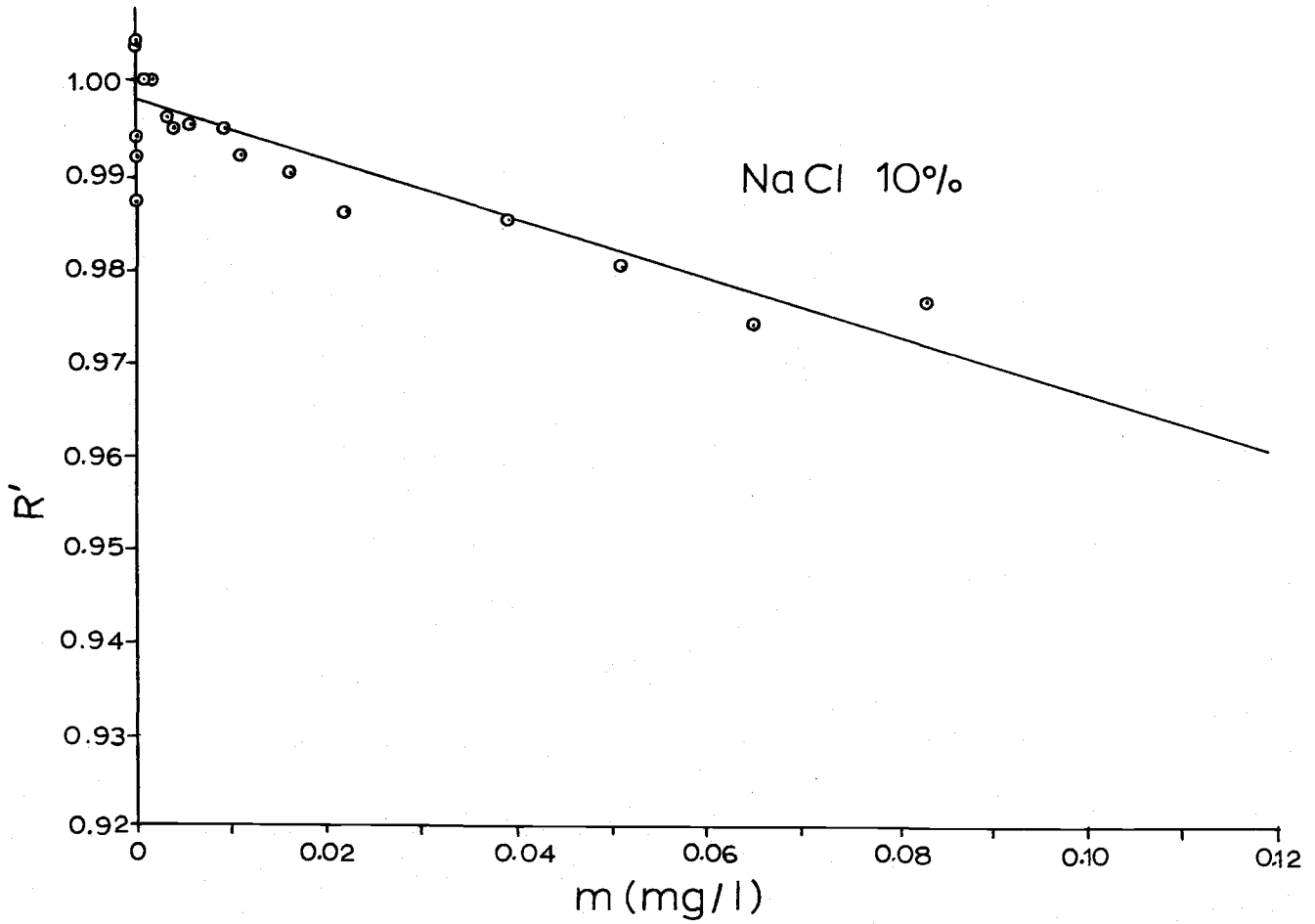

Figure 22. Plot of experimental data for NaCl 10%.

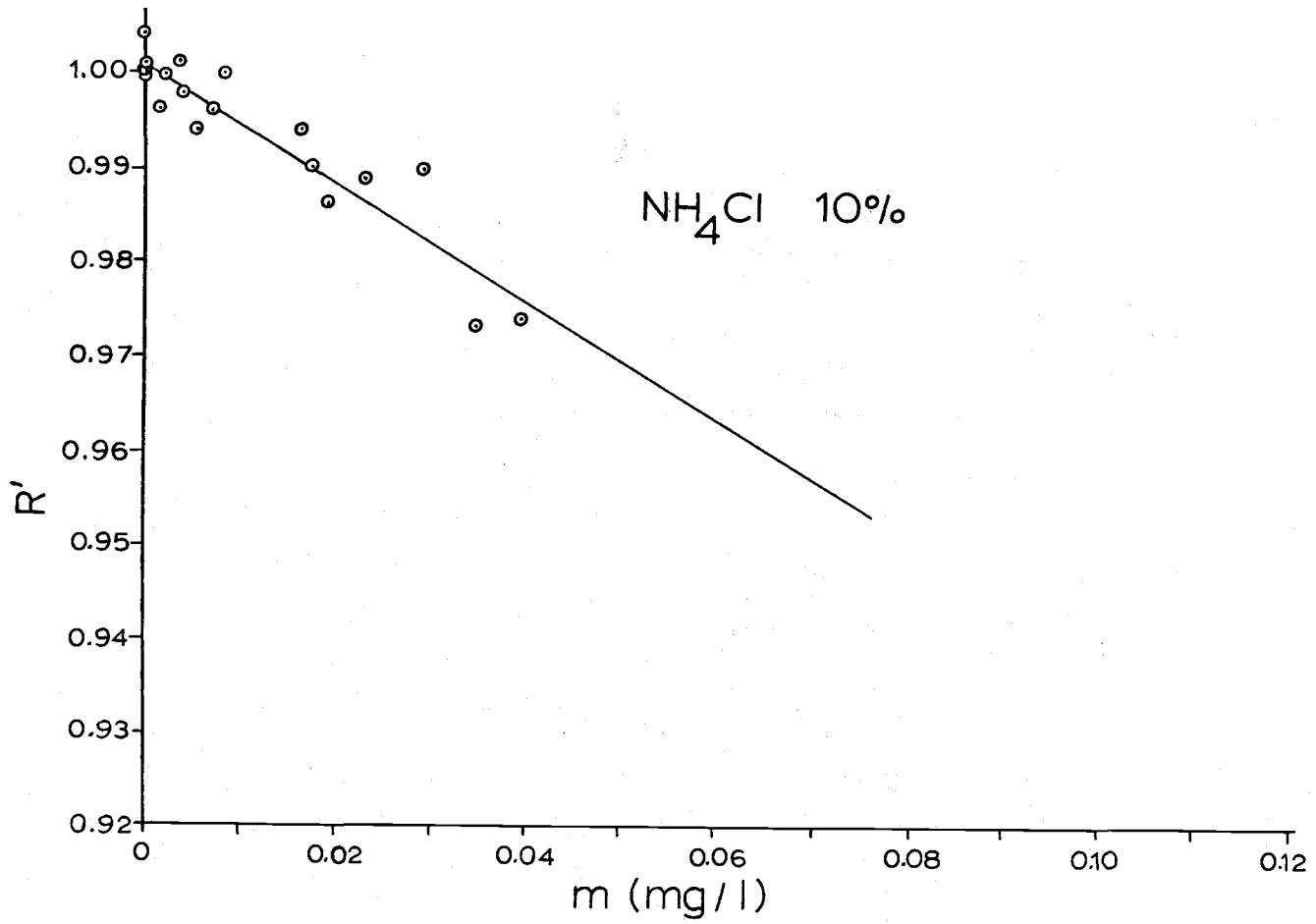

Figure 23. Plot of experimental data for NH_4Cl 10%.

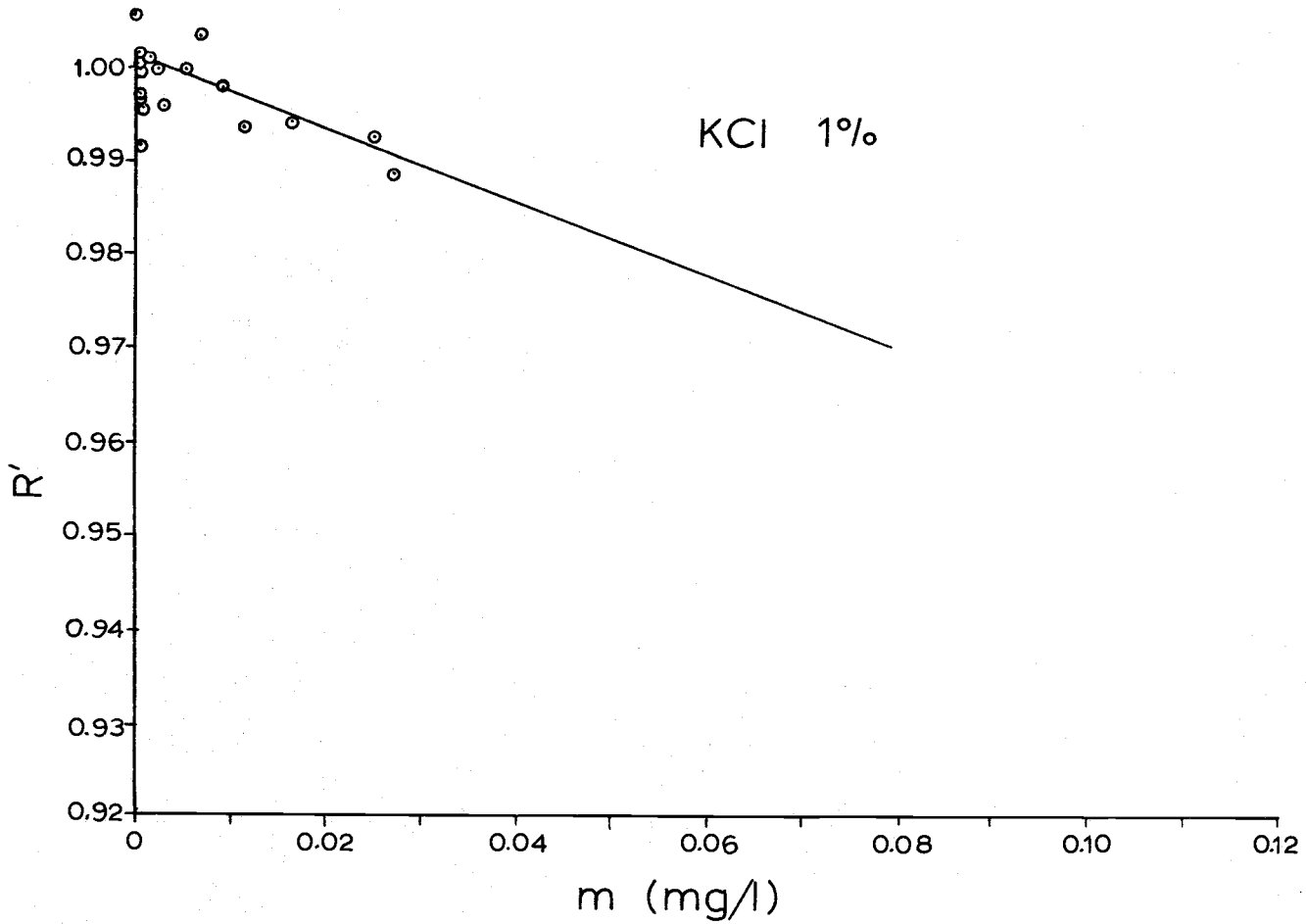

Figure 24. Plot of experimental data for KCl 1%.

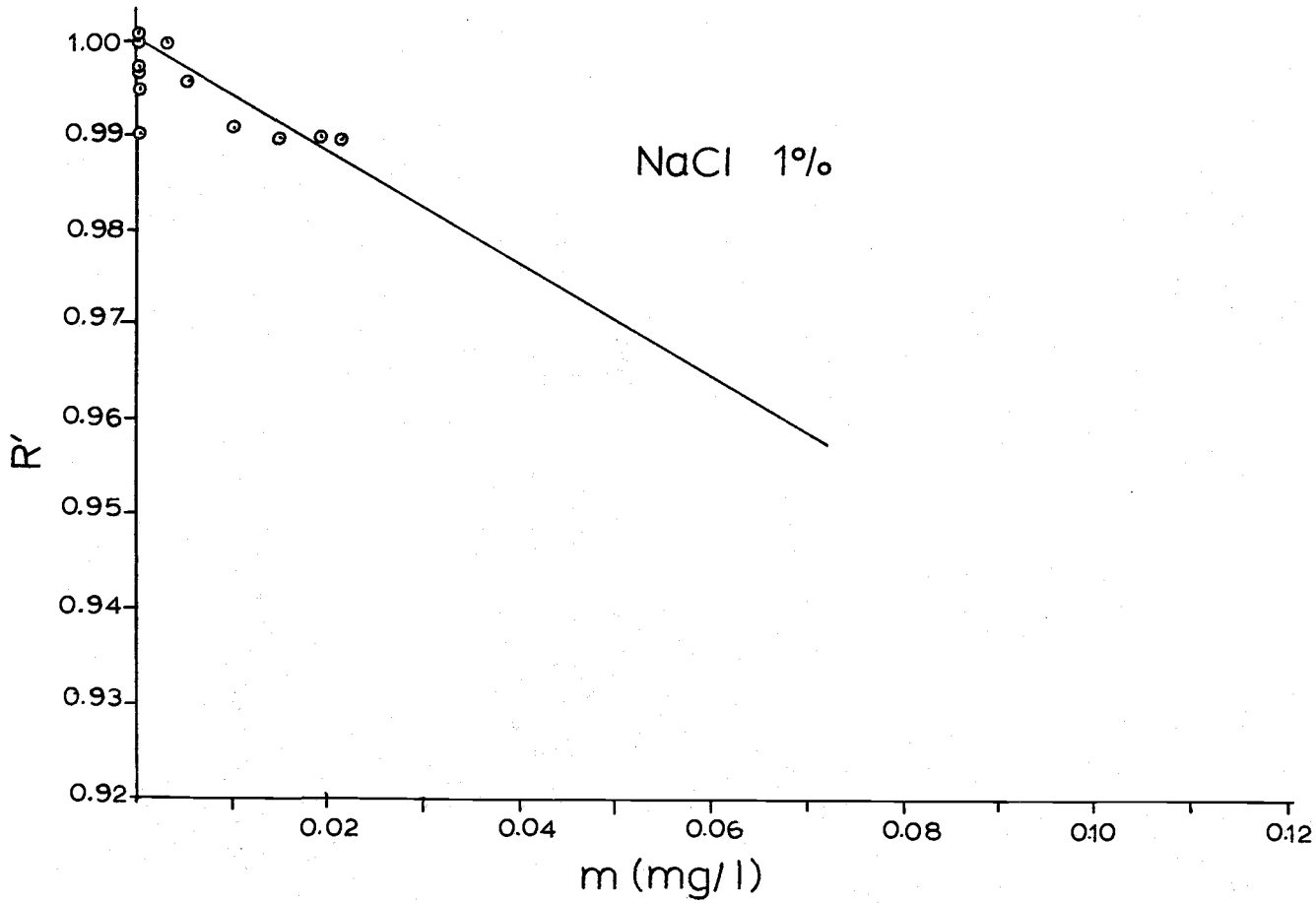

Figure 25. Plot of experimental data for NaCl 1%.

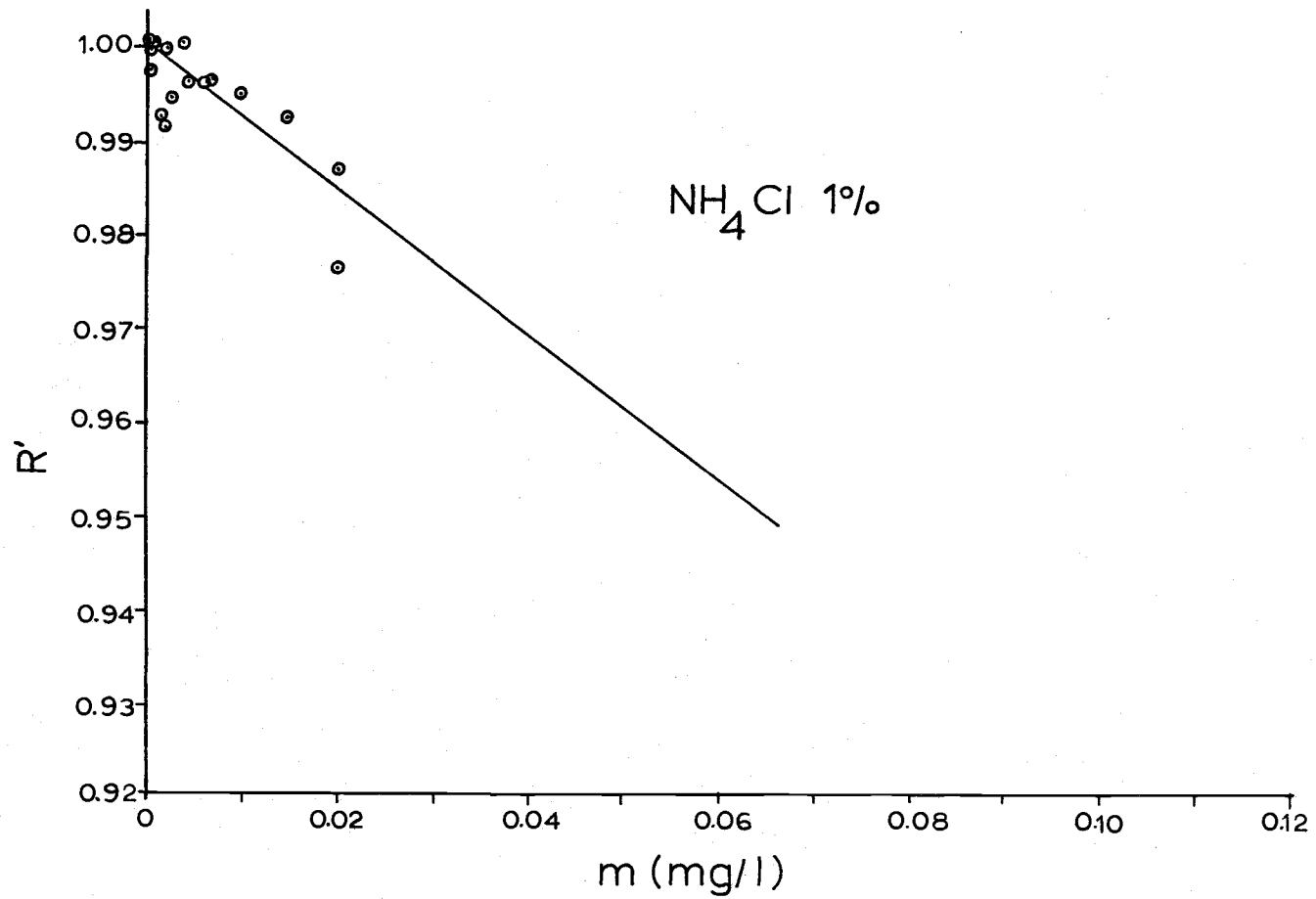

Figure 26. Plot of experimental data for NH_4Cl 1%.

TABLE V

Linear Regression Equations and Correlation Coefficients

Aerosol	Percent	(R' = A + B m) A	B (1/mg)	Correlation Coefficient
NaCl	20	0.9990	-0.5476	0.986
NH_4Cl	20	1.0002	-0.6790	0.909
KCl	20	0.9990	-0.6008	0.987
NaCl	10	0.9977	-0.3139	0.957
NH_4Cl	10	1.0016	-0.6316	0.902
KCl	10	0.9987	-0.2617	0.861
NaCl	1	1.0010	-0.5898	0.893
NH_4Cl	1	0.9998	-0.7697	0.811
KCl	1	1.0005	-0.3842	0.813

m data points and the corresponding R' values from the least squares line and the per cent difference between the two values of R' for each data point.

In each of these curves, the data has been corrected so that they all have the common intercept on the ordinate of 1.0. The fact that R(0) is not equal to 1.0 experimentally is due to the fact that the incident light is not perfectly parallel. The reasons for this deviation from perfect collimation are: (1) the spherical and chromatic aberrations associated with the condensing and particularly the Fresnel lenses, and (2) the finite size of the light source, i.e., the lamp filament, even after condensing, is not a true point source. These effects were observed and are illustrated in Figure 27. If the light were parallel, the flux recorded by the pyranometer at m = 0 would be the same for both the pinhole and the open position of the diaphragm since all of the light incident on the objective lens would be focused at a point within the pinhole. Thus the ratio of the two fluxes would equal 1.0. When the incident light has a non-parallel component, however, this non-parallel component is not detected with the diaphragm in the pinhole position. With the diaphragm in the open position, both the parallel and the non-parallel components are detected resulting in a ratio R (or R') that is less than 1.0. The correction that has been applied in Figures

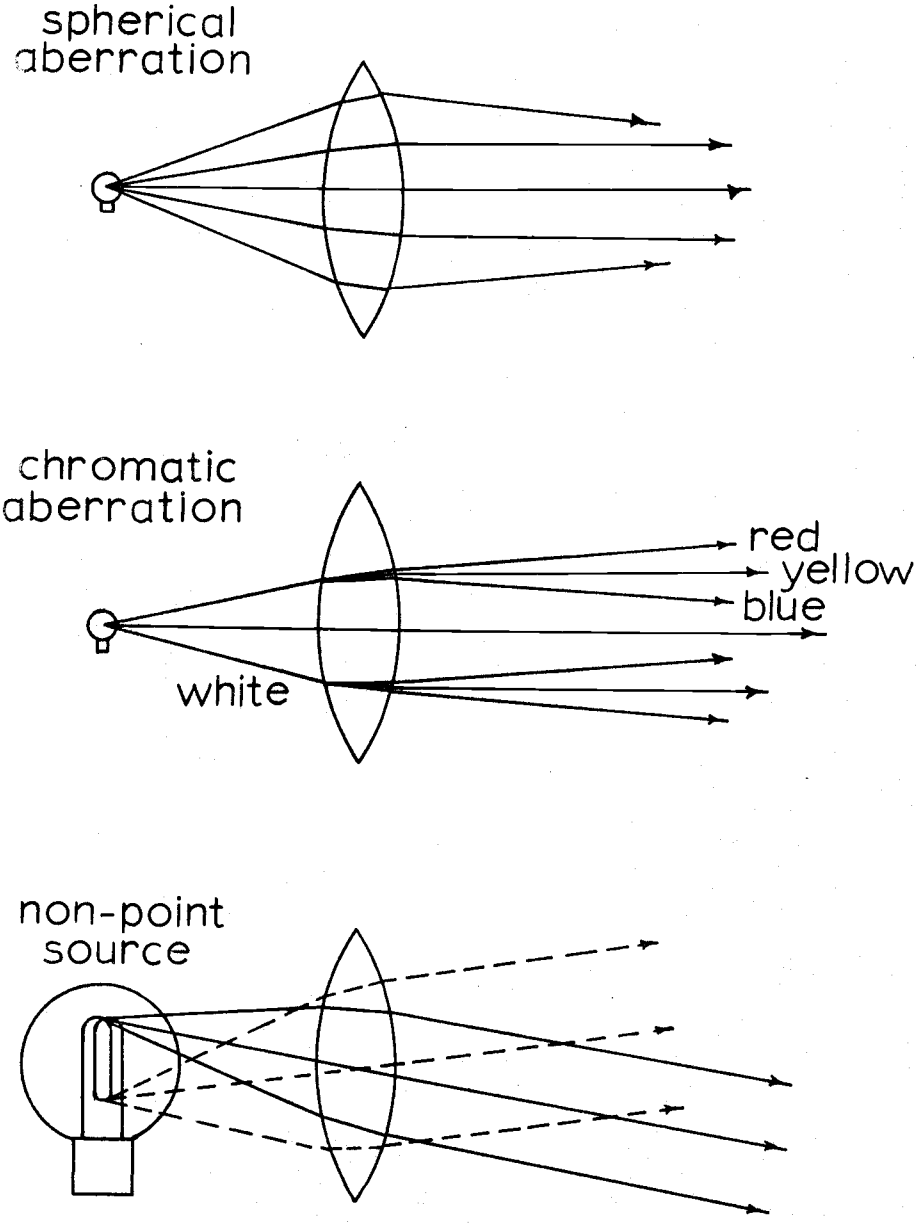

Figure 27. Causes for imperfect collimation.

18 through 26 is a simple addition of constant additive correction factor F, to all R' values, whose magnitude brings R'(0) up to 1.0. Thus the relationship of all the data points remains exactly as measured. The magnitude of this correction, however, is not truly constant over all m and the slope of the R' vs m curve must be multiplied by 1/R'(0). This can be seen by examining the regression equation of the measured values of R' on m:

$$\begin{aligned} R'(m) &= R'(0) - C\,m \\ &= R'(0)\left(1 - \frac{C}{R'(0)}\,m\right) \end{aligned} \tag{48}$$

where: C is the uncorrected slope.

This can be rearranged to give:

$$R'(m)/R'(0) = 1 - \frac{C}{R'(0)}\,m \tag{49}$$

which is of the same form as equation (45) if $K_2 = \frac{C}{R'(0)}$.

Both the additive correction factor [1-R'(0)] and the slope correction factor [1/R'(0)] were obtained by first plotting the uncorrected R' vs m curves and determining R'(0) from the regression equations. These values of R'(0) were then used in plotting Figures 18 through 26. The experimentally measured value of the slope for each R' vs m curve along with its slope correction factor, its additive correction factor, and the corrected value of the

slope are listed in Table VI.

In order to facilitate the comparison of the results of the nine experimental runs, all of the data from the nine runs are plotted together in Figure 28. The least squares straight line for the aggregate data is also indicated. Appendix C lists each experimental data point used to find this least squares line, its corresponding point (with the same value of m) on the regression line, and the percent difference between the two.

Experimental Particle Size Distributions

A sample size distribution for each of the nine aerosols used in this experiment was obtained by microscopic examination using a Porton graticule to obtain projected area diameters. Due to time limitations, a size distribution was not obtained for each of the 114 measurements of R and m. The samples were collected on Metricel GA-4 triacetate membrane filters (Gelman Instrument Company) which were made transparent on the microscope slide with dioxane. These size distributions are shown in Figures 29, 30, and 31. The tables of the data points are in Appendix E.

TABLE VI

Experimental Values of dR'/dm and Correction Factors

Aerosol	Percent	Experimental Slope (1/mg)	Slope Correction, 1/R'(0)(1/mg)	Corrected Slope (1/mg)	Additive Correction, F (1/mg)
NaCl	20	-0.5476	1.1899	-0.6516	0.1596
NH_4Cl	20	-0.6790	1.2073	-0.8198	0.1717
KCl	20	-0.6008	1.1838	-0.7113	0.1553
NaCl	10	-0.3139	1.1932	-0.3745	0.1619
NH_4Cl	10	-0.6316	1.2133	-0.7663	0.1758
KCl	10	-0.2617	1.1798	-0.3088	0.1524
NaCl	1	-0.5898	1.1891	-0.7013	0.1590
NH_4Cl	1	-0.7697	1.2034	-0.9262	0.1690
KCl	1	-0.3842	1.1905	-0.4574	0.1600

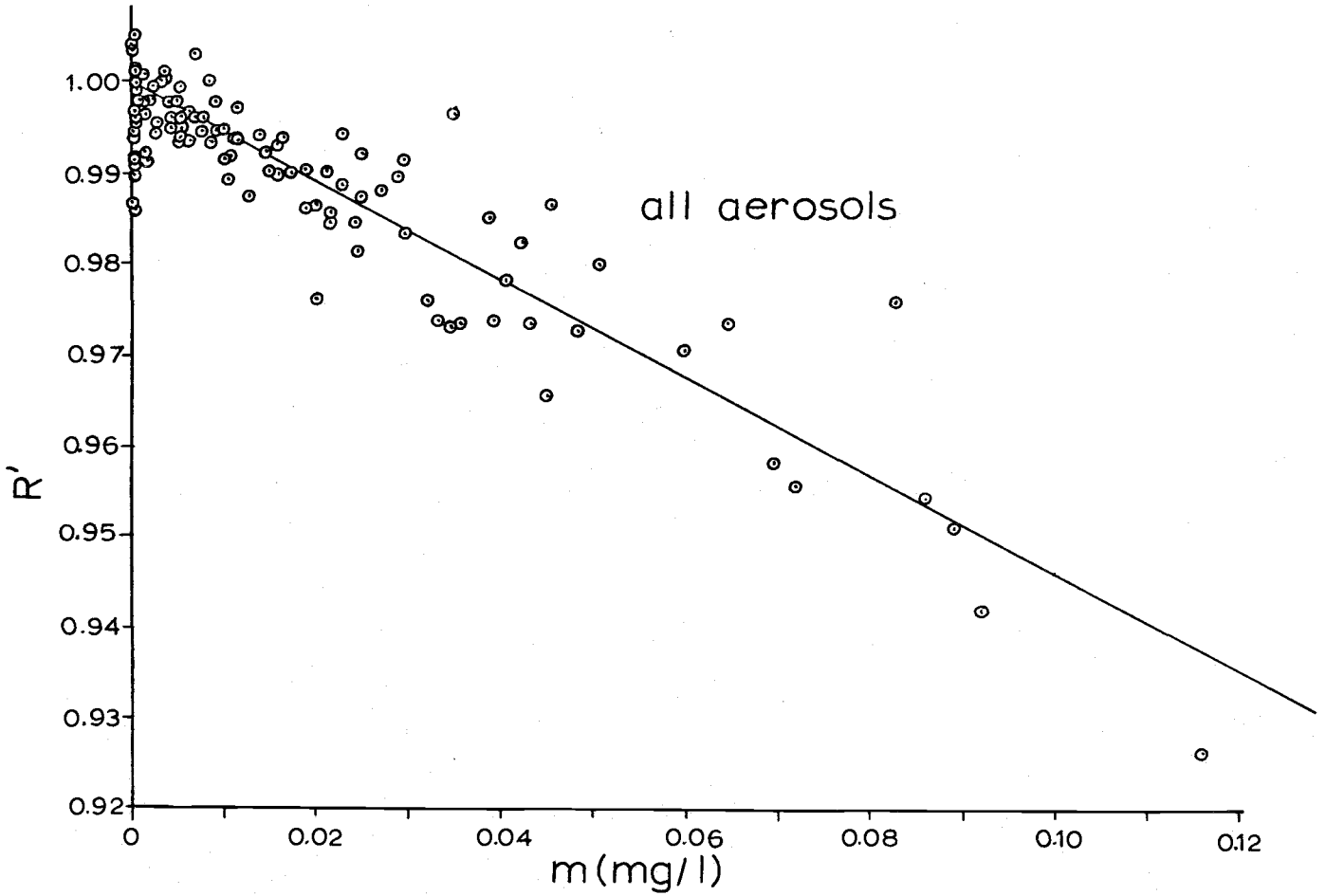

Figure 28. Plot of experimental data for all aerosols.

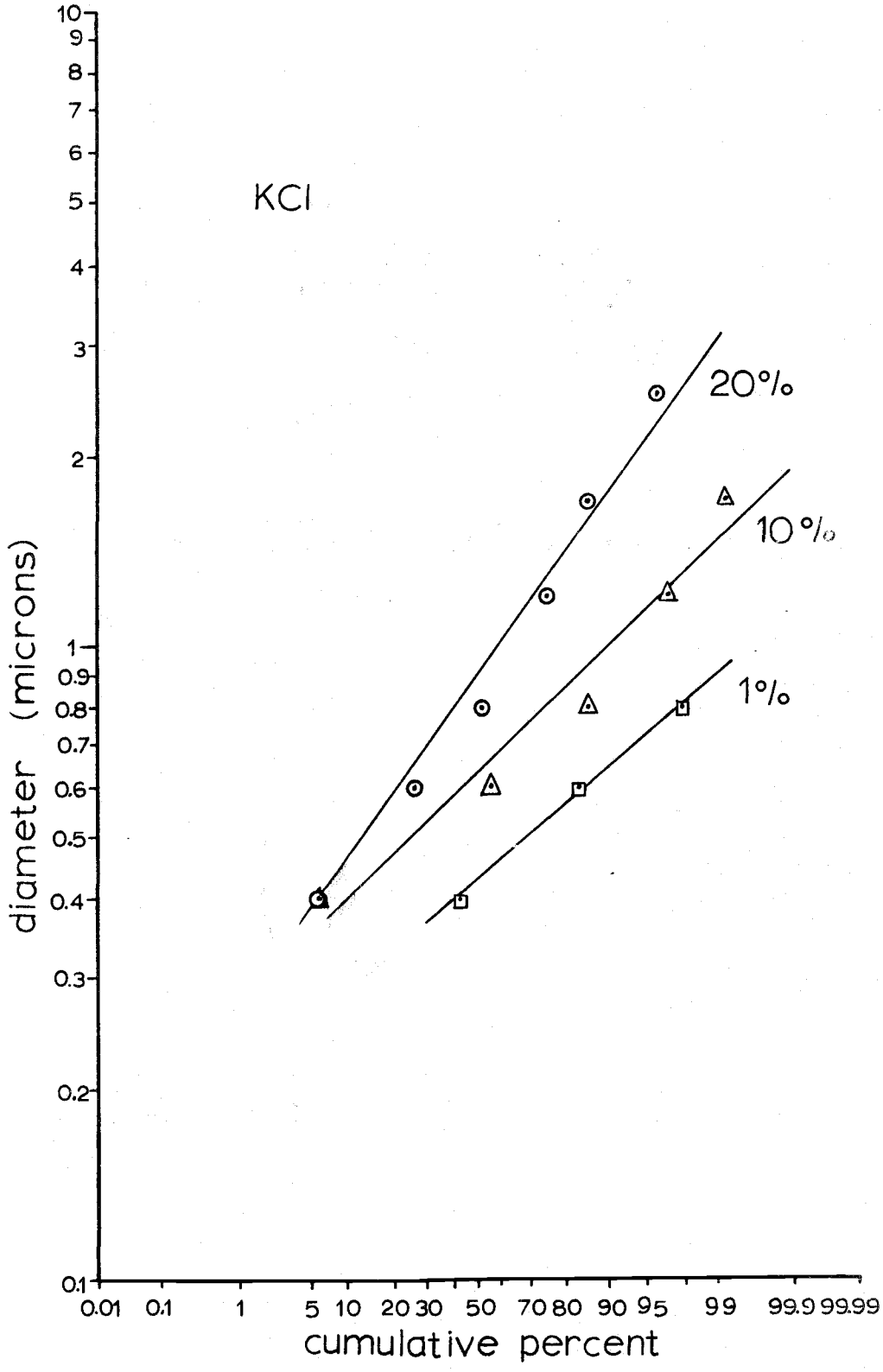

Figure 29. Sample particle size distributions for KCl.

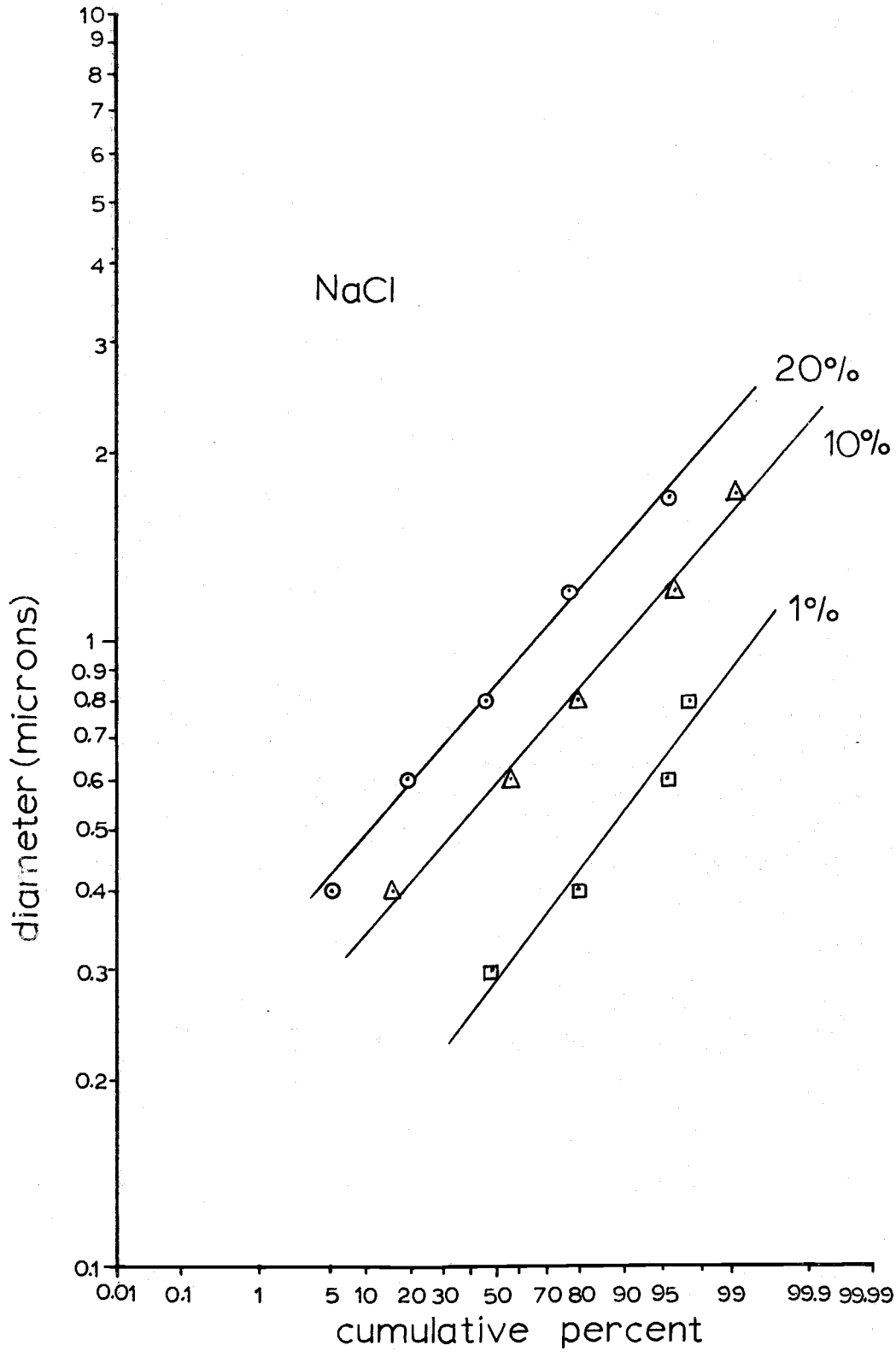

Figure 30. Sample particle size distributions for NaCl.

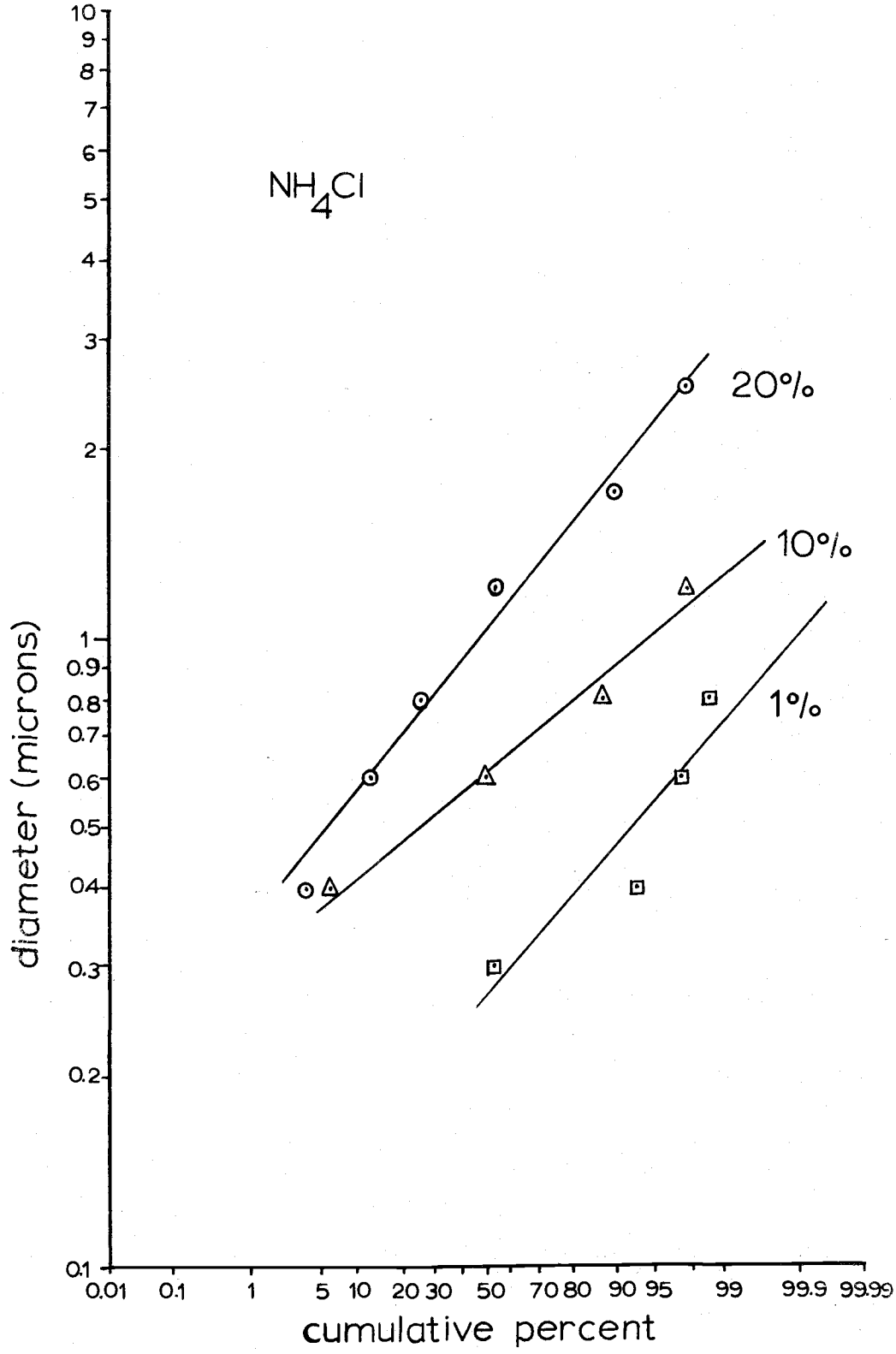

Figure 31. Sample particle size distributions for NH_4Cl.

VI. DISCUSSION

Discussion of Experimental Results

The experimental data from this investigation yields two salient results. The first and most apparent is the linearity of the dependence of R' on m. The second is the dependence that the results have on the aerosol index of refraction and the mean aerosol diameter.

The linearity of the individual R' vs m curves is apparent both from the scatter diagrams and from Table VI which lists the correlation coefficients for each set of data and its least squares line. Five out of the nine correlation coefficients are greater than 0.90, and none are below 0.811. For the number of data points involved, these coefficients indicate correlation at a 99% confidence level in all but one case. For the one exception, correlation is indicated at a 95% confidence level. Appendix B, which lists each data point and its corresponding point on the least squares line, demonstrates the correlation further by indicating that only two experimental R' value out of the 114 total were more than 0.7% above or below their respective least squares line. This evidence supports the contention that a correlation between the ratio R and the aerosol mass concentration does exist, and,

moreover, indicates that the functional form of the dependence of R and R' on m fits the prediction of the mathematical model.

The dependence of the experimental results on the aerosol index of refraction and on the mean aerosol diameter shows up as small changes in the slope of the R' vs m curve. This dependence is illustrated in Figure 32, which is a plot of $|dR'/dm|$ as a function of the aerosol mean diameter for the three indices of refraction used in this experiment. It can be seen that the variations in the slope due to variations in either the index of refraction or the mean diameter are large relative to one another, but quite small on an absolute scale. For a given index of refraction, the greatest change in slope due to a change in mean diameter is 0.3825 l/mg for KCl. This means that a change of 0.01 mg/l in the aerosol concentration results in changes in R' for the two KCl aerosols that differ by 0.003825. This is approximately 10% of the total variation in R' encountered in this experiment, or about 0.3% of the actual R' values. It should be noted that a change in aerosol concentration of 0.01 mg/l is very large in terms of atmospheric concentrations. The maximum allowable concentration of lead aerosols under the California Ambient Air Quality Standards is 1.5×10^{-6} mg/l averaged over 30 days. The smallest change in slope

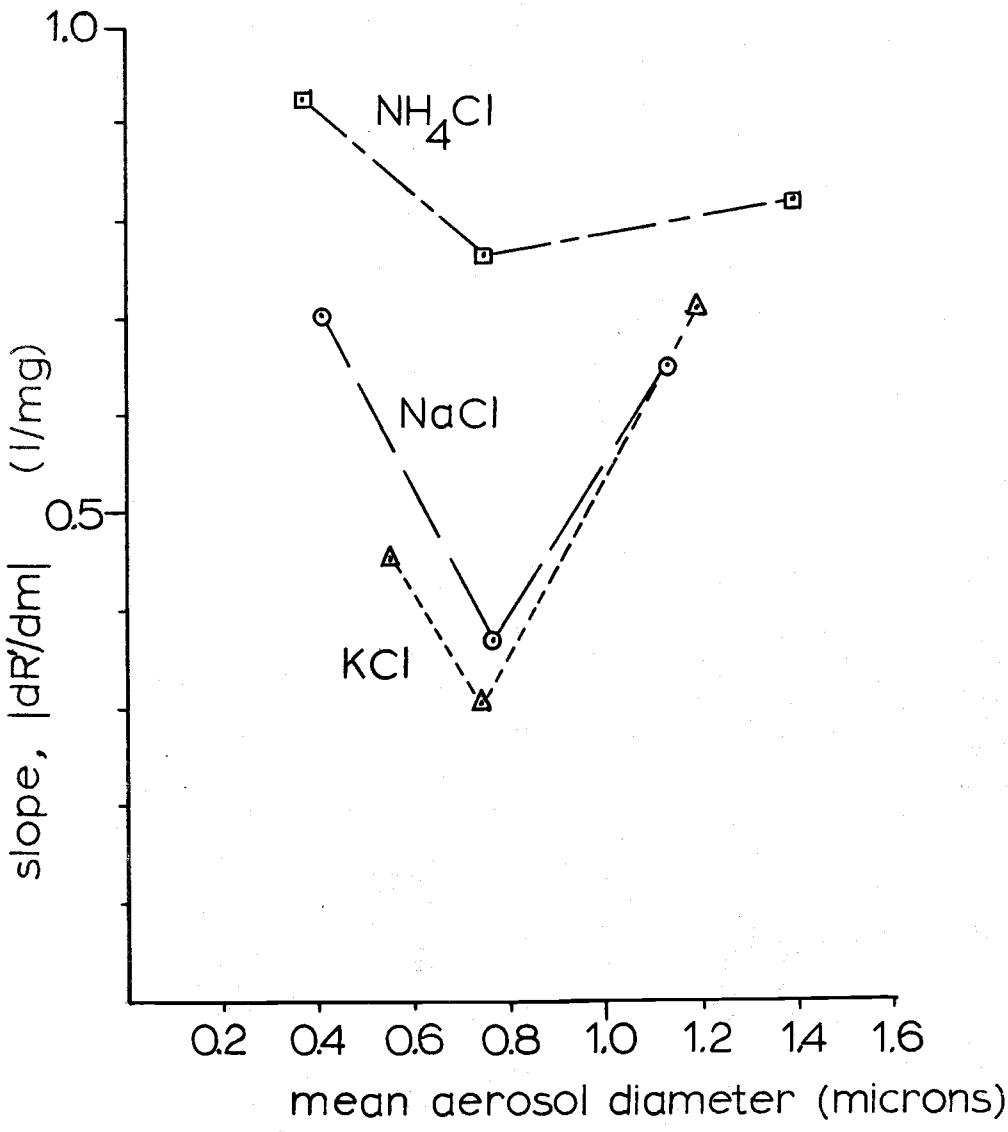

Figure 32. Experimental values of the slope of R' vs m as a function of mean aerosol diameter.

is 0.0535 l/mg and is for NH_4Cl.

The greatest difference in slope due to a difference in index of refraction (for a given mean diameter) is approximately 0.46 l/mg at d_m = 0.75 microns.

The second result indicated by Figure 32 is that the R' vs m slope is not a monotonic function of the mean aerosol diameter. For each of the indices of refraction, the R' vs m slope decreases with increasing d_m from the 1% nebulizer concentration to the 10% concentration then increases with a further increase in d_m from its 10% nebulizer concentration to the 20% concentration.

Figure 32 also shows that the dependence of the R' vs m slope on the index of refraction is not uniform over all d_m, but appears to be roughtly proportional at least for the lower values of d_m. (The indices of refraction for KCl, NaCl, and NH_4Cl are 1.49, 1.54, and 1.64, respectively.) In the range of d_m values obtained with the 20% nebulizer concentrations, however, the order of the slopes for the three indices of refraction appear to begin changing.

The weak dependence of the results on the aerosol index of refraction and mean aerosol diameter is also illustrated in Figure 28 which is a scatter diagram of all the data points from the nine experimental runs. The linear least-squares regression line for the aggregate

data is also shown. A visual inspection shows the close grouping of the data points about the least-squares line independent of the index of refraction and the mean diameter of the aerosol. More significant is the high correlation coefficient (0.936), since it is independent of the units used. A graphical plot of the data, on the other hand, could be constructed to appear closely grouped by choosing a scale that compresses the ordinate.

Comparison of Experimental and Theoretical Results

In comparing the experimental results with the mathematical model, it can be seen that the general functional relationship between R' and m is in agreement; however, the experimental points below m = 0.001 mg/l have been omitted due to the obvious non-linearity, the theoretical and experimental slopes of the R' vs m curves are in disagreement, and a dependence of the slope on the aerosol index of refraction and mean diameter not predicted by the mathematical model appears experimentally.

The non-linearity of the R' vs m data for low values of m can be explained by considering the assumption of the Junge size distribution which was made in the mathematical model. The Junge particle size distribution is based on a steady state in the shape of the distribution which is arrived at through the mechanisms of particle diffusion,

coagulation and sedimentation, and applies to so-called "aged" aerosols, i.e., aerosols that have had sufficient time to allow the mechanisms to operate. According to Smoluchowsky's theory (Smoluchowsky, 1918), the rate of coagulation is proportional to the square of the particle concentration and thus a low concentration would require a longer time to reach the steady state distribution. Since all measurements were made after relatively short aging times (five minutes) due to total time limitations, it is expected that at the lowest concentrations, the aerosol may not have had sufficient time to reach the Junge-shaped distribution. The result is a relative excess of the smaller particles (Junge, 1958), which in this experiment are in the size range (0.3 to 1.0 microns) that scatter light most efficiently (Volz, 1954; Junge, 1955; Pueschel and Noll, 1966; Horvath, 1966). Since R' is defined in equation (44) as $1-(f_s/f_u)$, the resultant increase in f_s and decrease in f_u lead to a decrease in R'. This result is seen in the R' vs m scatter diagrams.

The disagreement between the theoretical and experimental values for the slopes of the R' vs m curves is shown in Table VII which lists both the theoretical and experimental slopes. In calculating the theoretical slopes, λ was taken as 0.55 microns and ν was taken as 3.0 following Junge (1955, 1958). The difference in the three theoretical values is a result of the difference in the

TABLE VII

Experimental and Theoretical Values of dR'/dm

Aerosol	Experience Slope (l/mg)	Theoretical Slope (l/mg)
	-0.6516 (20%)	
NaCl	-0.3745 (10%)	-89.2
	-0.7013 (1%)	
	-0.8198 (20%)	
NH_4Cl	-0.7663 (10%)	-125.6
	-0.9262 (1%)	
	-0.7113 (20%)	
KCl	-0.3088 (10%)	-97.3
	-0.4574 (1%)	

The percentages in parentheses are the nebulizer concentrations.

specific gravities of the three aerosol materials. The explanation for this disagreement between experiment and theory is not as simple as that for the non-linear behavior at low values of m. Several possible explanations exist.

The most probable cause of the disagreement is the difference in the width of the aerosol size distributions assumed by the model and generated in the laboratory. Following Bullrich (1964), the Junge distribution in the mathematical model was taken to have the boundary radii, 0.04 and 10.0 microns. A sample of a typical experimental distribution, NH_4Cl-10%, was found to have the boundary radii, 0.2 and 0.85 microns. Figure 33 shows this distribution along with the Junge distribution having the same slope and representing the same total mass. The location of the Junge distribution on this graph with respect to the experimental distribution was determined by equating the total mass of the particles in each distribution as given by equation (38) to yield:

$$4/3\pi\gamma 0.434\ c_{th}\int_{0.04}^{10.0} r^{(2-\nu)}dr = 4/3\pi\gamma 0.434\ c_{ex}\int_{0.2}^{0.85} r^{(2-\nu)}dr \quad (50)$$

or:

$$c_{th}\int_{0.04}^{10.0} r^{(2-\nu)}dr = c_{ex}\int_{0.2}^{0.85} r^{(2-\nu)}dr \quad (51)$$

where: c_{th} = the theoretical constant of proportionality

c_{ex} = the experimental constant of proportionality

ν = the Junge exponent and was found to be 3.5 from the experimental distribution

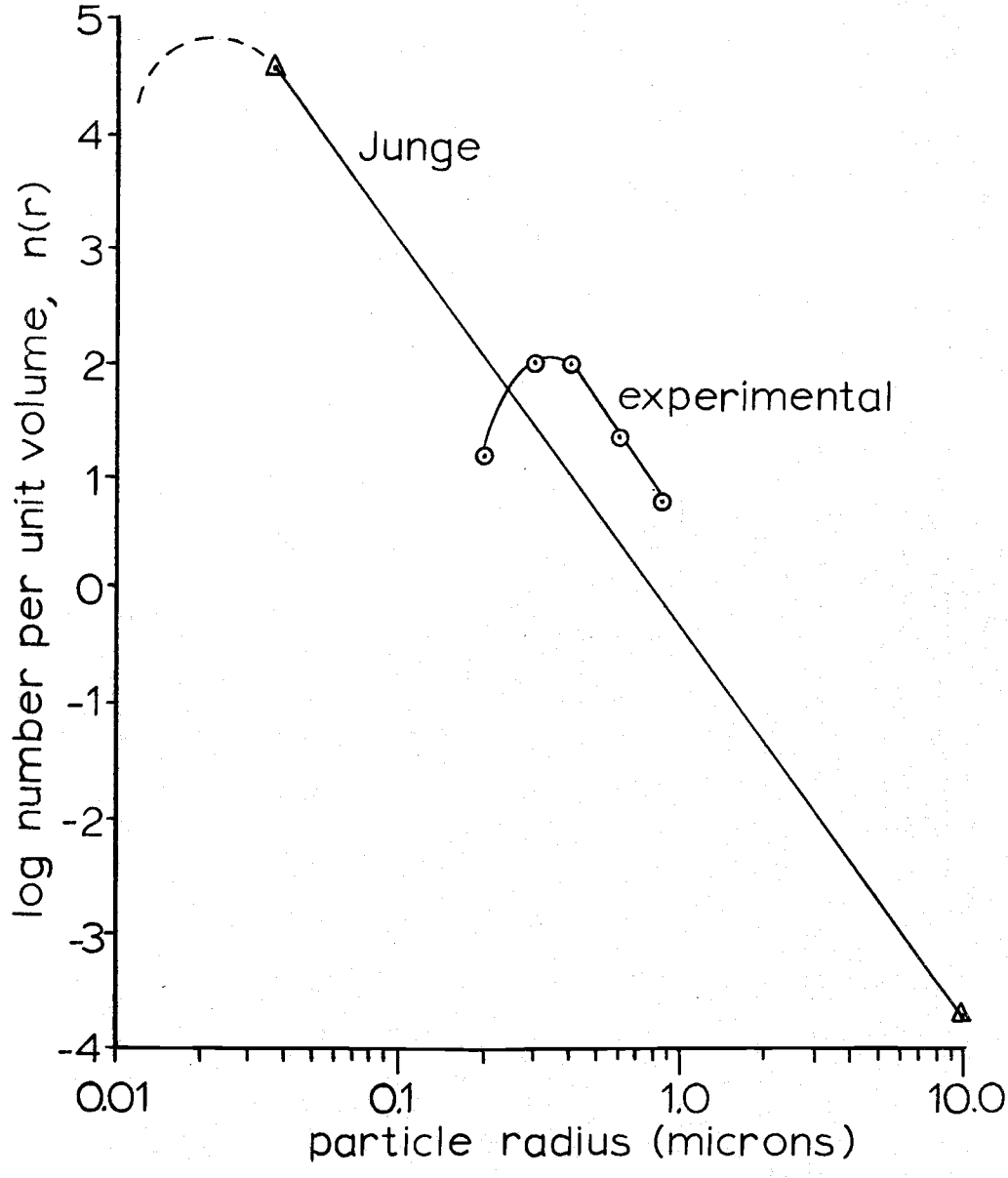

Figure 33. Comparison of experimental and "theoretical" particle size distributions on logarithmic axes.

Carrying out the integration and substituting the limits results in the following ratio:

$$c_{ex}/c_{th} = 6.38 \qquad (52)$$

Since n(r) is proportional to c, the ratio of the n(r) values of the two distributions for any given value r is equal to the ratio of their constants c.

Figure 34 shows the two curves on linear graph paper to give an undistorted visual comparison. A rough calculation of the area under the two curves shows that the Junge distribution has on the order of 10^2 times as many light scattering particles as the experimental distribution. All particles, however, do not scatter light with the same efficiency. The light scattering efficiency Q, defined as the ratio of the light scattered by a particle to the light gemoetrically incident of the particle, is an oscillating function of r (see Figure 35) whose general shape can be calculated (see Appendix E) following Penndorf's method (Penndorf, 1958). Depending on the location of the two size distribution curves with respect to maxima and minima in the efficiency curves, it can be seen that the fewer particles in the experimental distribution could result in less light being scattered, and thus a smaller value of f_s/f_u, and thus a smaller R' vs m slope than for the theoretical distribution by an amount more than sufficient to account for the disagreement in the theoretical and experimental R' vs m slopes. Two obstacles,

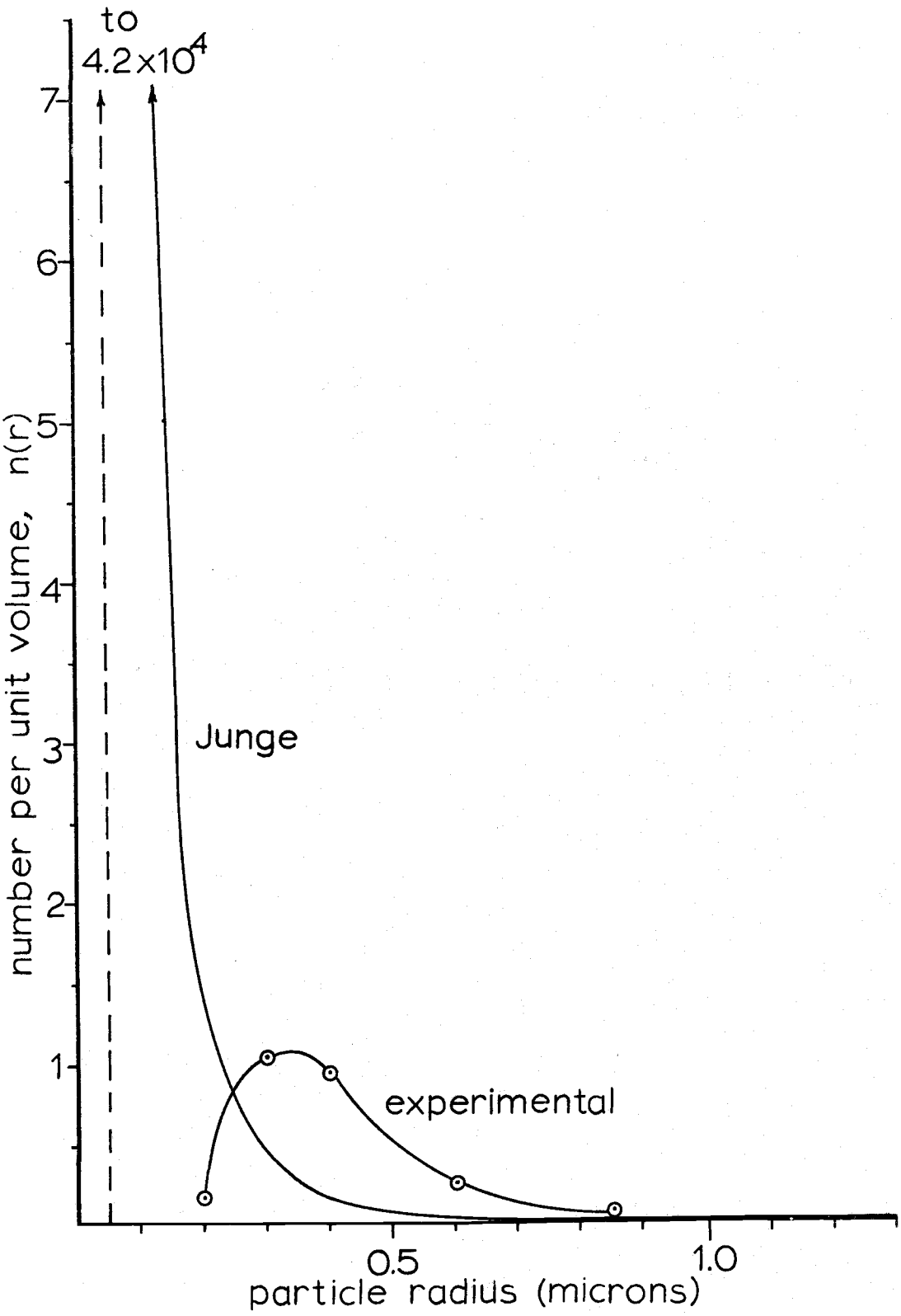

Figure 34. Comparison of experimental and "theoretical" particle size distributions on linear axes.

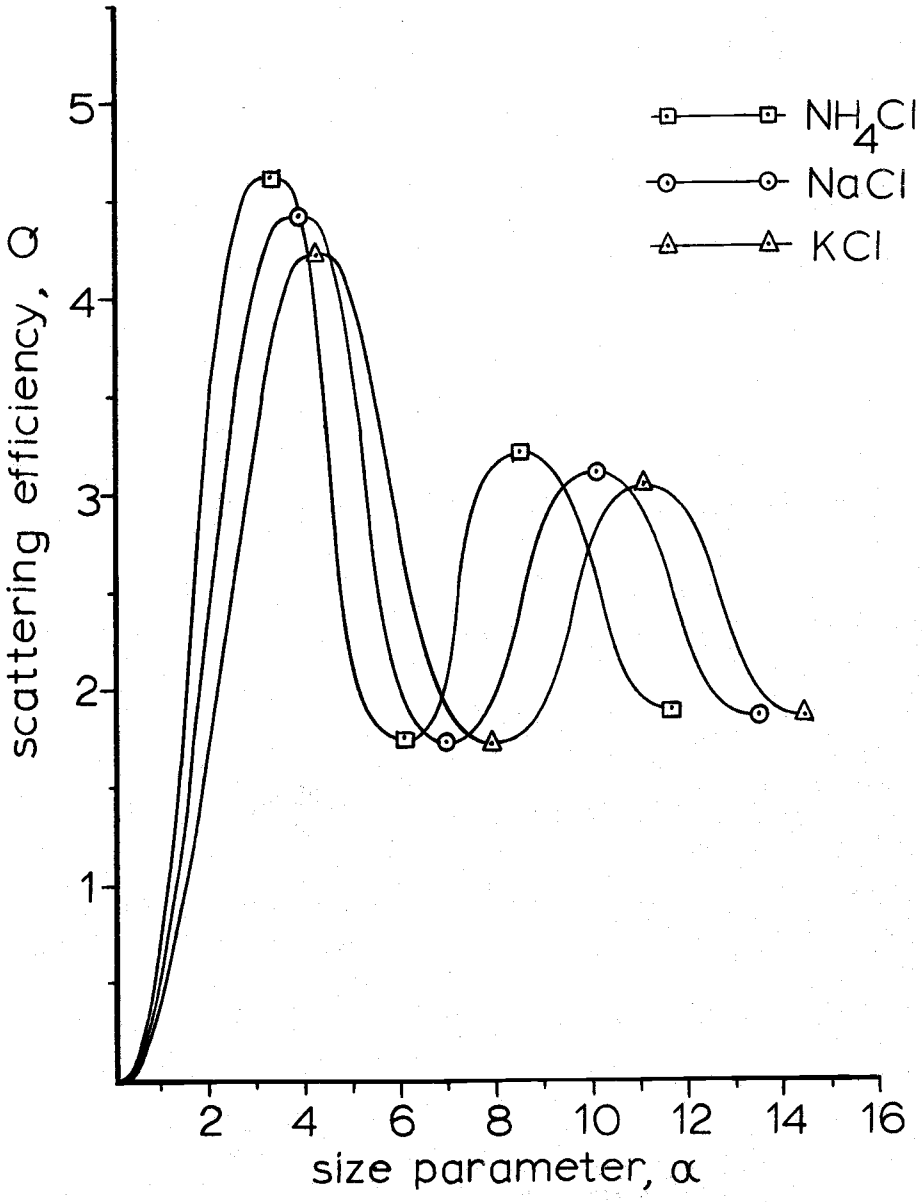

Figure 35. Scattering efficiencies of the experimental aerosols as a function of α.

however, stand in the way of performing an exact, quantitative analysis of this source of disagreement. First, the location of the experimental distribution on the r axis is not known precisely since it was determined at only one concentration for each run and consequently may not be representative of the average over the whole run. The distribution, indeed, may not have been constant over any given run. The second obstacle is the scattering efficiency curve. Penndorf's equation for the scattering efficiency curve provides only the general trends for the curve and neglects the so-called ripple structure. Figure 36 shows an exact curve and a smoothed curve obtained by Penndorf's method for spherical particles of index of refraction 2.0. The ripple structure presents a problem in that it fluctuates so violently and also that it is not possible to obtain exact curves with the ripple structure for particles of arbitrary indices of refraction without solving numerically a horrendous infinite series from the Mie solution.

A second difference between the theoretical and experimental aerosols that might lead to a difference in the theoretical and experimental R' vs m slopes lies in the magnitude of the aerosol concentrations. The mathematical model assumes that the aerosol is dilute enough so that multiple scattering may be neglected. Due to the short pathlength for the light in the experiment, the experi-

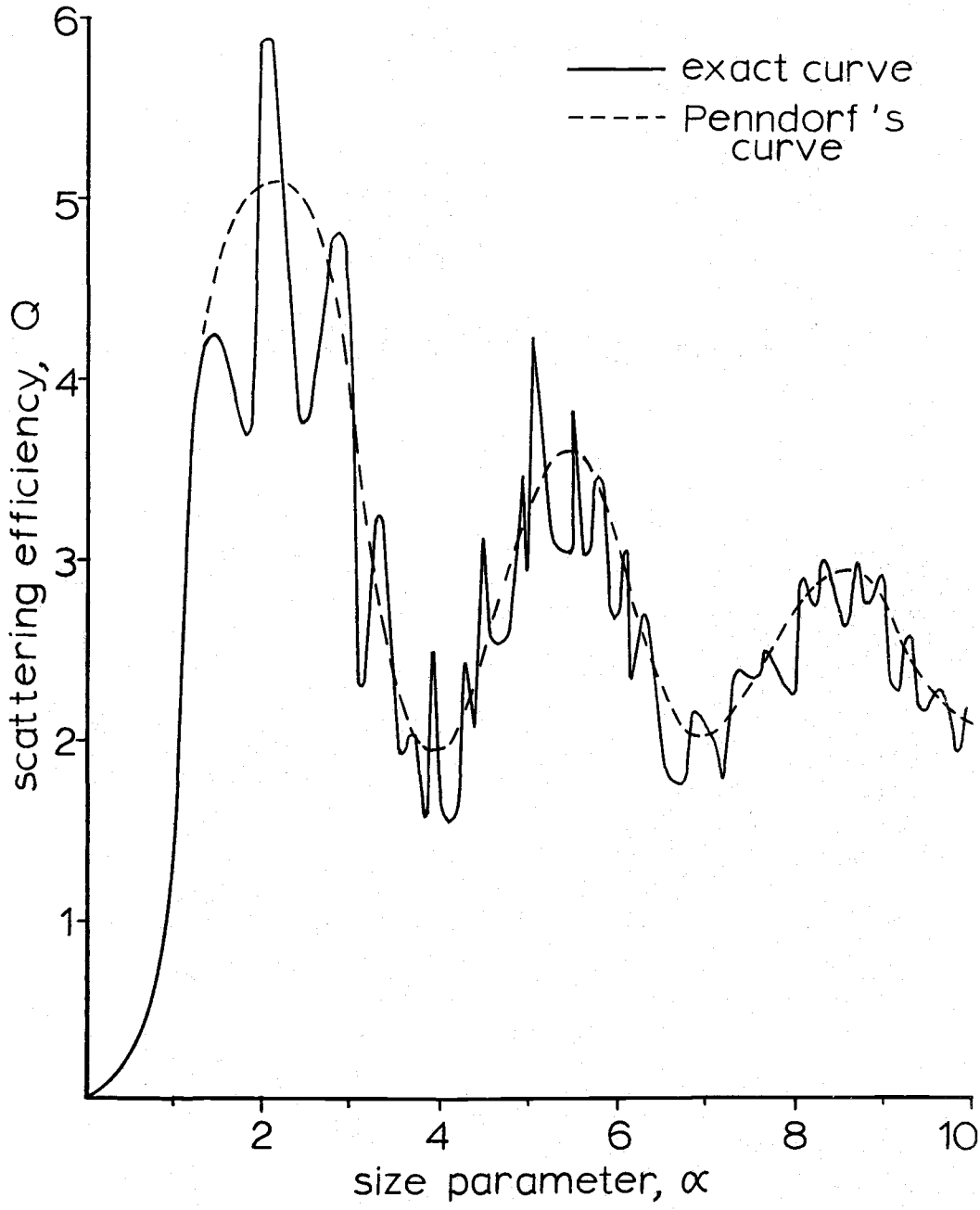

Figure 36. Comparison of scattering efficiencies calculated by Penndorf's method and by the Mie theory.

mental aerosol was used at a high concentration to provide measureable scattered light. The measurement of scattered light in the forward direction may make an individual multiple scattering event relatively insignificant, but with large particle concentrations the probability of such an event may increase to significant proportions. The range of concentrations measured in this experiment extended from 0.001 mg/l to 0.116 mg/l. Observed concentrations in the atmosphere range from 10^{-5} mg/l to 0.005 mg/l (Hendrickson, 1968).

A third difference between the theoretical and experimental aerosols lies in the shape of the individual particles. The mathematical model was derived for spherical particles, but from a miscroscopic examination, the experimental particles were found to be either irregular in shape or cubic and rectangular. Without further experimental investigation it is not possible to estimate the error introduced in assuming that randomly oriented particles of arbitrary shape will scatter light as spheres.

A fourth possible source of disagreement between the theoretical and experimental R' vs m slopes lies in the measurement of the Junge exponent ν. The value of ν for a given aerosol is the value of the slope of the size distribution curve plotted on log-log axes. Since, as indicated earlier, the measured size distributions may not

have been representative of the average distributions over their respective runs, and it is not known whether the distribution was actually constant over any given run, a small uncertainty is introduced in using the measured values of ν to calculate the theoretical R' vs m slopes for comparison with the experimental values of the slopes.

A fifth possible source of the disagreement lies in the construction of the mathematical model. In the model, it was assumed that only those volume elements inside the conical volume V (see Figure 4) contribute to f_s, and that the contribution made by these elements is the flux scattered through the solid angle subtended by the entire objective lens. The error in these assumptions, while tending to cancel one another, over estimates f_s, which has the effect of increasing the theoretical slope. This error is discussed in detail in section III.

A sixth possible source of error is in the assumption that the light scattering for polychromatic light could be approximated by the light scattering at the mean wavelength. This assumption was made in the mathematical model based on the "smoothed" scattering curves for polydisperse aerosols (Figure 5). However, since the wavelengths of light used in this experiment (0.4 to 0.7 microns) cover a small range, and the corresponding scattering curves vary gradually and continuously, the error

introduced is expected to be small.

Thus, only a qualitative discussion of the possible sources of the discrepancy between the theoretical and experimental values of dR'/dm is offered. A more extensive (and prohibitively time consuming) investigation of the instantaneous size distributions, a comparative study of the light scattering characteristics of spheres and cubes or irregular particles, and a detailed examination of multiple scattering would be necessary in order to present a quantitative analysis of the relative magnitudes of the effects mentioned in the preceeding paragraphs. A more profitable investigation, however, might be conducted on actual atmospheric aerosols.

The dependence of the R' vs m slopes on the aerosol index of refraction and the mean aerosol diameter follows directly from the narrowness of the experimental aerosol size distributions. The mathematical model does not predict such a dependence because of the very broad Junge size distribution assumed (see section III). The Junge distribution, covering a range of aerosol diameters from 0.04 to 10.0 microns, scatters light with an efficiency that is averaged over a large part of the scattering efficiency curve for individual particles (Figure 34), and becomes independent of the mean aerosol diameter and aerosol index of refraction. A very narrow distribution, on

the other hand, will have an efficiency that is averaged over only a very small part of the efficiency curve and its light scattering characteristics will follow these curves directly. The experimental aerosols used in this investigation fall in between these two extremes. From Figure 35, it can be seen that the scattering efficiencies are not monotonic functions of the particle diameters, and that the relationship between the efficiency and the index of refraction changes for different values of the particle diameter. The scattering efficiency is related to the R' vs m slope in that a high efficiency implies that more light is scattered and more light is removed from the incident beam. This increases f_s and decreases f_u resulting in lower values of R', which increases the slope since R' is fixed at a value of 1.0 at m = 0 and the slope is negative. Thus the dependence of the slope on the aerosol index of refraction and mean diameter can be explained in part by the similar behavior of the scattering efficiency curves. The fact that the dependence did not follow the efficiency curves exactly can be explained by the imprecise knowledge of the experimental size distributions as discussed previously, the polychromatic incident light, the existing width of the experimental aerosol size distributions, the fact that the width of the distributions increased proportionally with the mean diameter due to the method of generation, and the increase

in forward light scattering with particle diameter.

The effect of the polychromatic light is to necessitate the averaging of the scattering efficiency curves over the wavelengths of light. Since the scattering efficiency curve is a function strictly of α (where $\alpha=\pi d/\lambda$), the abscissa can be expressed as a diameter scale only for a fixed value of λ, and all curves for other wavelengths of light drawn on this abscissa will be compressed or expanded in the direction of the abscissa depending on whether the wavelength is less than or greater than that used to determine the scale originally. Thus, when polychromatic light is used, a curve averaged over the curves of all the component wavelengths and weighted by the relative intensity of that component must be used. The result of this averaging is a curve with damped oscillations with maxima and minima located where they would occur for the single curve for the weighted mean wavelength.

In order to compare the total light scattering by two polydisperse aerosols, the area under curves formed by product of each size distribution curve and the efficiency curve must be compared. This is especially true in the case where the width or spread of the two size distributions is not equal. Due to the method of varying the size distribution in this experiment, the width indeed was not constant.

The last consideration, the increase in forward scattering with increasing particle size, is necessary since

the scattered flux f_s, measured in this experiment is in fact light which has been scattered through an angle of 5° or less and is well within the domain of forward scattering. Thus, a group of small particles may scatter an equal amount of light in total as a group of large particles, but the value of f_s measured for the large particles will be greater. A possible result of this effect is seen in Figure 32 in that the slopes for the R' vs m curves for the 20% nebulizer concentrations in all three cases are approximately equal to or greater than the slopes for the 1% nebulizer concentrations, even though the peak scattering efficiencies decrease with increasing d.

The preceding considerations can also be cited in explaining the weakness of the dependency of the R' vs m slopes on the mean aerosol diameter and the index of refraction. The damping effect of polychromatic light on the scattering efficiency curves, and the increasing forward scattering with increasing particle diameter, both tend to level out the effects of the scattering efficiency curves, which in turn reduces any variation in R' due to variations in d_m for any given mass loading. The result of this is that the R' vs m slopes for aerosols with different values of d_m will not differ greatly. These same effects also tend to bring the scattering efficiency curves for the three different indices of refraction, which

already lie close together, into closer proximity. This decreases the difference in the scattering characteristics among the different indices of refraction, resulting in the weak dependence of the R' vs m slopes on the index of refraction.

Discussion of Errors

There are several sources of random errors that contribute to the scattering of the data points about the regression lines. The precision with which the values of f_{open} and $f_{pinhole}$ could be read from the strip chart was $\pm$ 0.001 volts, where the flux values ranged from about 0.35 volts to 6.0 volts. The aerosol photometer scale could be read to $\pm$ 0.01 scale units, which translates to $\pm$ 0.2% on the filter transmission scale at a photometer scale reading of 4.5, and $\pm$ 0.0001% at 1.5. These values become $\pm$ 0.00189 mg/l and $\pm$ 9.0×10^{-5} mg/l respectively, at their largest, in the case of the 20% NH_4Cl aerosol. Other sources of random errors are: amplifier drift, line voltage fluctuations (affecting the intensity of the light source), and non-homogeneous distribution of the aerosol in the test chamber.

An indication of the magnitude of the combined effect of these errors is given by the index of determination. The index of determination, which is the square of the correlation coefficient, can be interpreted as the fractional amount of the variation in the R' values that can be attributed to the linear regression of R' on m (Wine, 1964).

Thus, subtracting the index of determination from unity, gives the fractional amount of the R' variation that is due to non-linear effects such as the superposition of higher order ploynomial or transcendental functions, or to random errors. If it is accepted that the mathematical model is an accurate representation of the physical experiment, then the linear term in the power series expansion of R' is approximately three orders of magnitude greater than the quadratic term and even more so greater than the cubic and all other higher order terms. Since the model also predicts an absence of transcendental terms, the quantity (1 - index of determination) can be taken as the fractional amount of the R' variation that is due to random errors. The mathematical model, however, is not a completely accurate representation of the physical experiment, as seen by the lack of quantitative agreement between the theoretical and experimental results. Therefore it can be assumed that the fractional amount of the R' variation that is due to random errors is actually less than the quantity (1 - index of determination), and that this quantity may be considered to be only an upper bound. Table VIII lists the indices of determination and the quantity (1 - index of determination) for each of the nine experimental runs, and for the aggregate data. Using the aggregate data as an example, the numbers in the table can be interpreted as follows: 87.6% of the variation in the

TABLE VIII

Maximum Estimates of Random Errors

Aerosol	Percent	Index of Determination	Maximum Fraction of Regression Due to Random Errors
NaCl	20	0.9723	0.0277
NH_4Cl	20	0.8268	0.1732
KCl	20	0.9735	0.0265
NaCl	10	0.9162	0.0838
NH_4Cl	10	0.8133	0.1867
KCl	10	0.7420	0.2580
NaCl	1	0.7979	0.2021
NH_4Cl	1	0.6578	0.3422
KCl	1	0.6616	0.3384
Aggregate Data		0.8760	0.1240

ratio R', when all of the data from the nine experimental runs are plotted together, is due to the linear regression of R' on m, and at most, 12.4% of the variation is due to random errors. This error is comparable to that found in commercial aerosol measuring instruments such as the integrating nephelometer.

VII. CONCLUSION

Results

A mathematical model, based on the Mie theory of light scattering and the Junge aerosol size distribution, was developed that predicted the following functional dependence of R and R' on the mass concentration m:

$$R = 1/(1+Km) \tag{52}$$

and,

$$R' = 2-(1/R) = 1-Km \tag{53}$$

where: K is a constant depending on the specific gravity of the aerosol, the aerosol size distribution, and the average wavelength of incident light and the pathlength of light and the lens area of the measuring system.

Experimental measurements of R' as a function of m were made. A linear correlation between R' and m was indicated by the correlation coefficients for the nine experimental runs that ranged from 0.811 to 0.987. All but one of these coefficients indicated correlation at a 99% confidence level; the exception was at a 95% confidence level.

The values of K found experimentally ranged from 0.3088 to 0.9262 l/mg and were found to have a weak

dependence on the mean aerosol diameter and the aerosol index of refraction. The relationship between K and the mean aerosol diameter was not monotonic and followed qualitatively, the scattering efficiency curves. The relationship between K and the aerosol index of refraction appeared to be roughly proportional for the 1% and 10% nebulizer concentrations but the relationship began to deteriorate at the 20% concentration. This again followed qualitatively the behavior of the scattering efficiency curves.

Since the mathematical model was developed for atmospheric aerosols, the values of K were in quantitative disagreement with the experimental values; however, the functional relationship between R' and m indicated experimentally was identical to that in the model.

Recommendations

Based on the conclusion that R or R' and m appear to follow well defined relationships and that the relationships become independent of the aerosol index of refraction and mean aerosol diameter for broad aerosol size distributions as found in the atmosphere, it appears that a possibility exists for using measurements of the ratio R or R' as an indicator of the aerosol mass concentration. The feasibility of these measurements in the atmosphere using sunlight is even more strongly implied by the results

of the mathematical model. The model predicts that the variations in R or R' with variations in m will be much greater (by a factor of approximately 10^2) in the atmosphere than in the laboratory, resulting in a greater sensitivity in determining m from R or R', and reducing the effect of random errors in the measurement of R or R'. It is thus recommended that atmospheric study of the relationships examined in this investigation be undertaken.

Another application that might warrant further investigation is the substitution of these or similar light flux ratio measurements for transmissometer measurements due to the inherent error in the lens-pinhole arrangement used in the transmissometer to eliminate scattered light. It has been found that these errors may become significant, especially in high aerosol concentrations such as those found in stack discharges (Uthe, 1973).

BIBLIOGRAPHY

BIBLIOGRAPHY

Berek, M., K. Maennchen and W. Schaefer. 1936. Tyndallometric measurement of the dust content of the air, and a new dust measuring apparatus. Zeitschrift fur Instrumentenkunde 56:49-56.

Beutell, R. G., and A. W. Brewer. 1949. Instruments for the measurement of visual range. Journal of Scientific Instrumentation 26:357-359.

Bullrich, K. 1964. Scattered radiation in the atmosphere and the natural aerosol. In: Advances in geophysics, ed. by H. E. Lundsberg and J. Van Miegham. Vol. 10. New York, Academic Press, p. 99-260.

Cadle, R. D. 1965. Particle size: theory and industrial applications. New York, R. Reinhold. 390 p.

California Ambient Air Quality Standards. 1973. In: Air pollution in California: Annual report 1972. Sacramento, California Air Resources Board. 37 p.

Charlson, R. J., H. Horvath and R. F. Pueschel. 1967. The direct measurement of atmospheric light scattering coefficient for studies of visibility and pollution. Atmospheric Environment 1:469-478.

Charlson, R. J. 1968. Visibility. Unpublished manuscript. Seattle, Washington.

Chinn, J. H., C. M. Sliepcevich and M. Tribus. 1955. Particle size distributions from angular variation of intensity of forward scattered light at very small angles. Journal of Physical Chemistry 59:841-844.

Clarenburg, L. A., and L. H. Princen. 1963. An improved instrument for the measurement of the mass concentration of aerosols. Staub, Reinhaltung und der Luft 23:234-236.

Collis, R. T. H., and M. G. H. Ligda. 1964. Laser radar echoes from the clear atmosphere. Nature 203:508.

Collis, R. T. H., F. G. Fernald and M. G. H. Ligda. 1964. Laser radar echoes from a stratified clear atmosphere. Nature 203:1274-1275.

Debye, P. 1909. Der Lichtendruck auf Kugeln von beliebigem Material. Annalen der Physik 30:57-61. (Microfilm)

Fisher, M. A., S. Katz, A. Lieberman and N. E. Alexander. 1955. The aerosoloscope: an instrument for the automatic counting and sizing of aerosol particles. In: Proceedings of the Third National Air Pollution Symposium, Pasadena. p. 112-119.

Friedlander, S. K., and C. S. Wang. 1966. The self-preserving size distribution for coagulation and Brownian motion. Journal of Colloid and Interface Science 22:126-132.

Gucker, F. T., and D. G. Rose. 1954. A photoelectric instrument for counting and sizing aerosol particles. British Journal of Applied Physics, Supplement No. 3, 138:S138-S143.

Gucker, F. T. 1956. Aerosol particle counters. In: Proceedings of the Eleventh Industrial Waste Utilization Conference, Purdue University, Lafayette, Indiana. p. 284-312.

Hatch, T. F. 1961. Dust and disease. In: The air we breathe, ed. by S. M. Farber and R. H. C. Wilson, Springfield, Illinois, Thomas. p. 115-125.

Hendrickson, E. R. 1968. Air sampling and quantity measurement. In: Air pollution, Vol. II, ed. by A. C. Stern, New York, Academic Press. p. 3-51.

Hewson, E. W. 1968. Meteorological measurements. In: Air pollution, Vol. II, ed. by A. C. Stern, New York, Academic Press. p. 329-387.

Hilding, A. C. 1965. Mucociliary insufficiency and its possible relation to chronic bronchitis and emphysema. Medicina Thoracalis 22:329-346.

Hodkinson, J. K. 1966. The optical measurement of aerosols. In: Aerosol science, ed. by C. N. Davies, New York, Academic Press. p. 287-357.

Hodkinson, J. K. 1966. Particle sizing by means of the forward scattering lobe. Applied Optics 5:839-843.

Horvath, H. 1966. Untersuchengung an Naturlichen und Anthropogenen Aerosolen. Doctoral dissertation. Vienna, University of Vienna. (Cited in: Charlson, R. J., H. Horvath and R. F. Pueschel. 1967. The direct measurement of atmospheric light scattering coefficient for studies of visibility and pollution. Atmospheric Environment 1:469-478.)

Junge, C. E. 1955. The size distribution and aging of natural aerosols as determined from electrical and optical data on the atmosphere. Journal of Meterology 12:13-25.

Junge, C. E. 1958. Atmospheric chemistry. In: Advances in Geophysics, ed. by H. E. Lundsberg and J. Van Miegham, Vol. 4. New York, Academic Press. p. 1-108.

Junge, C. E. 1963. Air chemistry and radioactivity. New York, Academic Press. 328 p.

Kerker, M. 1969. The scattering of light and other electromagnetic radiation. New York, Academic Press. 666 p.

Koshi, S. 1958. A new portable aerosol photometer. Bulletin of the National Institute of Industrial Health (Japan) 1:26-32. (Cited in: Davies, C. N. 1966. Aerosol science. New York, Academic Press. 468 p.)

Lundgren, D. A., and D. W. Cooper. 1969. Effect of humidity on light scattering methods of measuring particle concentrations. Journal of the Air Pollution Control Association 19:243-247.

Lauterbach, K. E., A. D. Hayes and M. A. Coelho. 1956. An improved aerosol generator. Archives of Industrial Health 13:156-160. (Microfilm)

McCormick, R. A., and D. M. Baulch. 1962. The variation with height of the dust loading over a city as determined from the atmospheric turbidity. Journal of the Air Pollution Control Association 12:492-496.

Mercer, T. T., M. I. Tillery and M. A. Fores. 1963. An electrostatic precipitator for the collection of aerosol samples for particle size analysis. Atomic Energy Commission Research and Development Report LF-6. Alburquerque, Lovelace Foundation. 13 p.

Middleton, W. E. K. 1952. Vision through the atmosphere. Toronto, University of Toronto Press. 250 p.

Mie, G. 1908. A contribution to the optics of turbid media, especially colloidal metallic suspensions. Annalen der Physik 25:377-445. (Microfilm)

Nadel, J. A. 1965. Structure-function relationships in the airways: bronchoconstriction mediated via vagus nerves or bronchial arteries; peripheral lung constriction mediated via pulmonary arteries. Medicina Thoracalis 22:329-346.

O'Konski, C. T., M. D. Briton and W. I. Higuchi. 1958. Light scattering instrumentation for particle size distribution measurements. In: American society for Testing and Materials special technical publication No. 250, Particle size measurements, Philadelphia. p. 2-28.

Penndorf, R. 1958. An approximation method to the Mie theory for colloidal spheres. Journal of Physical Chemistry 62:1537-1542.

Peterson, C. M., and H. J. Paulus. 1967. Micrometeorological variables applied to the analysis of variations in aerosol concentration and size. Presented at the sixtieth Annual Meeting of the Air Pollution Control Association, Cleveland. Paper No. 67-133, 19 numbered pages.

Pueschel, R. F., and K. E. Noll. 1966. Comparison of calculated and observed visibilities based on measured size distributions. Presented at the annual meeting of the Pacific Northwest International Section of the Air Pollution Control Association, Seattle, Washington, November 1966. (Cited in: Charlson, R. J. 1968. Visibility, unpublished manuscript, Seattle, Washington.)

Pueschel, R. F., and K. E. Noll. 1967. Visibility and aerosol size frequency distributions. Journal of Applied Meteorology 6:1045-1052.

Randall, J. M., and J. D. Keller. 1965. Unpublished manuscript. (Cited in: Hodkinson, J. K. 1966. The optical measurement of aerosols. In: Aerosol science, ed. by C. N. Davies, New York, Academic Press. p. 287-357.)

Robinson, E. 1968. Effect on the physical properties of the atmosphere. In: Air pollution, ed. by A. C. Stern, Vol. I, New York, Academic Press. p. 349-399.

Rockney, V. D. 1959. New developments in observations and instrumentation in the Weather Bureau. Bulletin of the American Meteorological Society 40:554-560.

Rossano, A. T., Jr. 1969. Air pollution control: guidebook for management. Stamford, Conneticut, Environmental Science Services. 214 p.

Sinclair, D. 1953. Light scattering instruments as an aid in air pollution measurements. Air Repair 3(1):51-56.

Sinclair, D. 1967. A new photometer for aerosol particle size analysis. Journal of the Air Pollution Control Association 17:105-108.

Smoluchowsky, M. Von. 1918. Versuch einer mathematischen Theorie der Koagulationskinetik Kolloider Losungen. Zeitschrift fur Physikalische Chemie 92:129-168. (Microfilm)

Steffens, C., and S. Rubin. 1949. Visibility and air pollution. In: Proceedings of the First National Air Pollution Symposium, Pasadena. Stanford Research Institute. p. 103-108.

Steffens, C. 1956. Visibility and air pollution. In: Air pollution handbook, ed. by Magill, P. L., F. R. Holden and C. Ackley. New York, McGraw-Hill. p. 6.1-6.43.

Stratton, J. A. 1941. Electromagnetic theory. New York, McGraw-Hill. 615 p.

Stuke, J. 1955. The Tyndalloscope II, a new improved construction of the dust measuring instrument. Gluckauf 91:1405-1406.

Stuke, J., and J. Rzeznik. 1964. The Tyndallograph, an optical dust measuring apparatus with electrical indicator. Staub, Reinhaltung und der Luft 24:366-368.

Thomas, A. L., and S. Oglesby. 1959. Permissible-type dust counter for coal mines. Mining Engineering 11:328-331.

Thomas, A. L., N. Bira, R. H. Collins and P. Rice. 1961. A portable photometer and particle analyzer. Journal of the Instrument Society of America 8(7):52-56.

Uthe, E. 1973. Meteorologist, Stanford Research Institute. Personal communication.

Van De Hulst, H. C. 1957. Light scattering by small particles. New York, Wiley and Sons. 470 p.

Volz, F. 1959. Photometer mit Selen-Photoelement zur spektralen Messung der Sonnenstrahlung und zur Bestimmung der Wellenlanenabhangigkeit der Dunsttrubung. Archiv fur Meteorologie, Geophysik und Bioklimatologie, series B, 10:100-131. (Cited in: McCormick, R. A., and D. M. Baulch. 1962. The variation with height of the dust loading over a city as determined from the atmospheric turbidity. Journal of the Air Pollution Control Association 12:492-496.

Whitby, K. T., and W. E. Clark. 1966. Electric aerosol particle counting and size distribution measurement system for 0.015 to 1 micron range. Tellus 18: 573-586.

Wine, R. L. 1964. Statistics for scientists and engineers. New Jersey, Prentice-Hall. 671 p.

Zinky, W. R. 1962. A new tool for air pollution control: the aerosol particle counter. Journal of the Air Pollution Control Association 12:578-583.

APPENDICES

APPENDIX A: R vs m data

m (10^{-3}mg/l)	R	Relative Humidity(%)	Temperature(°F)
NaCl 20%			
0.112	0.8636	36.5	72
0.400	0.8627	37.0	72
0.768	0.8577	38.5	72
0.920	0.8597	39.0	72
1.240	0.8611	39.0	72
2.240	0.8636	39.0	72
4.16	0.8601		72
4.880	0.8595	40.0	72
6.480	0.8595	40.0	72
7.680	0.8581	40.0	72
10.80	0.8546	41.0	72.5
15.20	0.8550	41.0	72.5
25.60	0.8532	41.0	72.5
32.0	0.8455	41.0	72.5
40.80	0.8464	41.5	72.5
70.40	0.8323	42.0	72.5
86.40	0.8547	42.0	72.5
NH_4Cl 20%			
0.161	0.8511	43.0	73.0
0.514	0.8525	43.0	73.0
0.857	0.8557	43.0	73.0

APPENDIX A (continued)

m	(10^{-3}mg/l)	R	Relative Humidity(%)	Temperature(°F)
0.911		0.8541	44.0	73.0
1.098		0.8547	44.0	73.0
1.553		0.8527	44.0	73.5
1.875		0.8507	44.0	74.0
2.143		0.8512	44.0	74.0
2.624		0.8498	44.0	74.0
3.480		0.8503	44.0	74.0
4.390		0.8525	44.0	74.0
5.140		0.8489	44.0	74.0
6.000		0.8514	44.0	74.0
7.230		0.8490	44.0	74.0
9.370		0.8486	44.0	74.0
13.92		0.8447	44.0	74.0
18.75		0.8464	44.0	74.0
22.50		0.8423	44.0	74.0
25.45		0.8400	44.0	74.0
30.52		0.8415	44.5	74.0
35.88		0.8353	44.5	74.0
KCl 20%				
0.240		0.8574	43.0	72.0
0.356		0.8556	44.0	72.0

APPENDIX A (continued)

m	(10^{-3}mg/l)	R	Relative Humidity(%)	Temperature(°F)
0.788		0.8594	44.0	72.0
1.200		0.8573	44.5	72.0
1.817		0.8636	45.0	72.0
3.150		0.8666	46.0	73.0
4.175		0.8632	46.0	73.0
6.040		0.8615	46.0	73.0
15.77		0.8576	46.0	73.0
23.65		0.8543	46.0	73.0
33.24		0.8460	46.0	73.0
45.25		0.8406	46.0	73.0
48.00		0.8485	46.0	73.0
43.80		0.8458	46.5	75.0
58.90		0.8441	47.75	75.0
72.00		0.8331	47.0	76.0
89.10		0.8302	47.0	76.5
92.50		0.8235	47.0	77.0
116.60		0.8141	47.5	77.0
NaCl 10%				
0.148		0.8638	38.0	71.5
0.296		0.8558	39.0	71.5
0.363		0.8546	39.0	71.5
0.472		0.8509	39.5	72.0

APPENDIX A (continued)

m	(10^{-3}mg/l)	R	Relative Humidity(%)	Temperature(°F)
0.787		0.8633	40.0	72.0
1.390		0.8610	40.5	72.0
1.936		0.8610	41.0	72.0
3.330		0.8578	41.0	72.0
3.995		0.8575	42.0	72.0
5.810		0.8590	42.0	72.0
8.890		0.8574	42.0	72.0
11.50		0.8551	42.0	72.0
16.94		0.8534	42.0	72.0
22.68		0.8509	42.5	72.0
39.3		0.8503	43.0	72.0
51.40		0.8462	44.0	72.0
65.30		0.8419	44.0	72.0
83.50		0.8432	44.0	72.0
NH_4Cl 10%				
0.175		0.8511	43.0	72.0
0.389		0.8515	44.0	73.0
0.486		0.8538	44.0	73.0
0.974		0.8478	44.0	73.0
2.630		0.8506	44.0	73.0
3.460		0.8523	44.0	73.0
3.990		0.8490	44.0	73.0

APPENDIX A (continued)

m (10^{-3}mg/l)	R	Relative Humidity(%)	Temperature(°F)
5.500	0.8463	44.0	73.0
6.470	0.8482	44.0	73.0
7.680	0.8521	44.0	73.0
16.06	0.8468	44.0	73.0
17.50	0.8434	44.5	73.0
19.95	0.8408	44.5	73.0
23.83	0.8431	45.0	73.0
34.50	0.8318	45.0	73.0
39.90	0.8326	45.0	73.0
KCl 10%			
0.328	0.8674	39.0	73.5
0.618	0.8635	40.0	73.5
0.965	0.8684	40.0	73.5
1.512	0.8668	41.0	73.0
2.207	0.8666	41.0	73.0
2.521	0.8663	41.0	73.0
4.410	0.8644	41.0	73.0
4.915	0.8664	41.0	73.0
8.510	0.8649	41.0	73.0
11.66	0.8656	42.0	73.5
14.69	0.8639	42.0	73.5
11.66	0.8633	44.0	74.0

APPENDIX A (continued)

m	(10^{-3}mg/l)	R	Relative Humidity(%)	Temperature(°F)
11.72		0.8633	44.0	75.0
16.40		0.8627	44.0	75.5
22.70		0.8634	44.0	76.0
35.30		0.8643	44.0	76.0
42.80		0.8548	44.5	76.5
45.40		0.8577	44.5	76.5
NaCl 1%				
0.0854		0.8561	43.0	73.5
0.121		0.8598	43.0	73.5
0.208		0.8630	43.0	73.5
0.219		0.8610	43.0	73.5
0.314		0.8609	43.0	73.5
0.383		0.8625	44.0	74.0
0.458		0.8643	44.0	74.0
0.574		0.8610	44.0	74.0
0.786		0.8641	44.5	74.0
3.076		0.8641	44.5	74.0
5.740		0.8605	44.5	74.0
10.940		0.8568	46.0	73.5
15.370		0.8555	46.0	73.5
19.47		0.8557	46.0	73.0
21.20		0.8557	46.0	73.0

APPENDIX A (continued)

m (10^{-3}mg/l)	R	Relative Humidity(%)	Temperature(°F)
NH_4Cl 1%			
0.065	0.8564	38.0	73.5
0.128	0.8576	40.0	73.5
0.196	0.8556	41.0	74.0
0.266	0.8558	41.0	74.0
0.427	0.8540	41.0	74.0
0.498	0.8551	41.0	74.0
0.723	0.8559	41.0	74.0
0.978	0.8592	41.0	74.0
2.015	0.8493	42.0	73.5
2.37	0.8551	42.0	73.5
2.962	0.8512	42.0	73.5
3.67	0.8556	42.5	73.5
4.80	0.8529	43.0	73.5
6.04	0.8528	43.0	73.5
7.11	0.8528	43.0	73.5
15.40	0.8525	44.0	73.0
20.73	0.8386	44.0	73.0
9.59	0.8512	45.0	78.5
20.70	0.8457	46.0	79.5

APPENDIX A (continued)

m (10^{-3}mg/l)	R	Relative Humidity(%)	Temperature(°F)
KCl 1%			
0.056	0.8621	45.0	71.0
0.114	0.8620	45.0	72.0
0.158	0.8606	45.5	72.0
0.192	0.8661	46.0	72.0
0.239	0.8621	46.0	72.0
0.269	0.8606	46.0	72.0
0.224	0.8556	46.0	72.0
0.341	0.8622	46.0	72.0
0.436	0.8609	46.0	72.0
0.614	0.8587	46.0	72.0
0.896	0.8595	46.0	72.0
1.45	0.8621	46.0	72.0
2.30	0.8614	46.0	72.0
3.16	0.8590	46.0	72.0
4.52	0.8615	46.0	72.0
11.52	0.8572	47.0	73.0
9.82	0.8601	47.0	76.0
16.23	0.8579	48.0	77.5
25.59	0.8564	48.5	79.0
27.30	0.8534	48.5	79.0
7.51	0.8646	47.0	73.0

APPENDIX B: R' vs m Data and Comparison with Least-Squares Line

m (10^{-3}mg/l) (measured)	R' (measured)	R' (least-squares)	Difference	
NaCl 20%				
1.24000E+00	9.98300E-01	9.98320E-01	0.00%	****EVEN****
2.24000E+00	1.00160E+00	9.97773E-01	0.40%	****ABOVE***
4.16000E+00	9.97000E-01	9.96721E-01	0.00%	****EVEN****
6.48000E+00	9.96100E-01	9.95451E-01	0.00%	****EVEN****
7.68000E+00	9.94300E-01	9.94794E-01	0.00%	****EVEN****
1.08000E+01	9.89400E-01	9.93085E-01	0.30%	****BELOW***
1.52000E+01	9.90000E-01	9.90676E-01	0.00%	****EVEN****
2.56000E+01	9.87600E-01	9.84981E-01	0.20%	****ABOVE***
3.20000E+01	9.76900E-01	9.81477E-01	0.40%	****BELOW***
4.08000E+01	9.78100E-01	9.76658E-01	0.10%	****ABOVE***
7.04000E+01	9.58100E-01	9.60449E-01	0.20%	****BELOW***
8.64000E+01	9.54300E-01	9.51688E-01	0.20%	****ABOVE***
4.88000E+00	9.96100E-01	9.96327E-01	0.00%	****EVEN****
NH_4Cl 20%				
1.09800E+00	1.00170E+00	9.99473E-01	0.20%	****ABOVE***
1.55300E+00	9.98900E-01	9.99164E-01	0.00%	****EVEN****
1.87500E+00	9.96200E-01	9.98945E-01	0.20%	****BELOW***
2.14300E+00	9.96900E-01	9.98763E-01	0.10%	****BELOW***
2.62400E+00	9.95000E-01	9.98437E-01	0.30%	****BELOW***
3.48000E+00	9.95600E-01	9.97855E-01	0.20%	****BELOW***
4.39000E+00	9.98700E-01	9.97238E-01	0.10%	****ABOVE***
5.14000E+00	9.93700E-01	9.96728E-01	0.30%	****BELOW***
6.00000E+00	9.97100E-01	9.96144E-01	0.00%	****EVEN****
7.23000E+00	9.93800E-01	9.95309E-01	0.10%	****BELOW***
9.37000E+00	9.93300E-01	9.93856E-01	0.00%	****EVEN****
1.39200E+01	9.87900E-01	9.90767E-01	0.20%	****BELOW***
1.87500E+01	9.90200E-01	9.87488E-01	0.20%	****ABOVE***
2.25000E+01	9.84500E-01	9.84941E-01	0.00%	****EVEN****
2.54500E+01	9.81300E-01	9.82938E-01	0.10%	****BELOW***
3.05200E+01	9.83300E-01	9.79496E-01	0.30%	****ABOVE***
3.58800E+01	9.74500E-01	9.75857E-01	0.10%	****BELOW***

APPENDIX B (continued)

m (10^{-3}mg/l) (measured)	R' (measured)	R' (least-squares)	Difference	
KCl 20%				
1.81700E+00	9.97300E-01	9.97917E-01	0.00%	****EVEN****
3.15000E+00	1.00130E+00	9.97116E-01	0.40%	****ABOVE***
4.17500E+00	9.96800E-01	9.96501E-01	0.00%	****EVEN****
6.04000E+00	9.94600E-01	9.95380E-01	0.00%	****EVEN****
1.57700E+01	9.89300E-01	9.89534E-01	0.00%	****EVEN****
2.36500E+01	9.84700E-01	9.84799E-01	0.00%	****EVEN****
3.32400E+01	9.73200E-01	9.79038E-01	0.50%	****BELOW***
4.52500E+01	9.65700E-01	9.71822E-01	0.60%	****BELOW***
4.80000E+01	9.72000E-01	9.70169E-01	0.10%	****ABOVE***
4.38000E+01	9.73000E-01	9.72693E-01	0.00%	****EVEN****
5.89000E+01	9.70600E-01	9.63620E-01	0.70%	****ABOVE***
7.20000E+01	9.55000E-01	9.55750E-01	0.00%	****EVEN****
8.91000E+01	9.50800E-01	9.45475E-01	0.50%	****ABOVE***
9.25000E+01	9.41000E-01	9.43433E-01	0.20%	****BELOW***
1.16600E+02	9.26900E-01	9.28953E-01	0.20%	****BELOW***
NaCl 10%				
1.39000E+00	1.00050E+00	9.97239E-01	0.30%	****ABOVE***
1.93600E+00	1.00040E+00	9.97068E-01	0.30%	****ABOVE***
3.33000E+00	9.96100E-01	9.96630E-01	0.00%	****EVEN****
3.99500E+00	9.95700E-01	9.96421E-01	0.00%	****EVEN****
5.81000E+00	9.97000E-01	9.95852E-01	0.10%	****ABOVE***
8.89000E+00	9.95600E-01	9.94885E-01	0.00%	****EVEN****
1.15000E+01	9.92400E-01	9.94066E-01	0.10%	****BELOW***
1.69400E+01	9.90100E-01	9.92358E-01	0.20%	****BELOW***
2.26800E+01	9.86700E-01	9.90556E-01	0.30%	****BELOW***
3.93000E+01	9.85900E-01	9.85340E-01	0.00%	****EVEN****
5.14000E+01	9.80100E-01	9.81542E-01	0.10%	****BELOW***
6.53000E+01	9.74100E-01	9.77179E-01	0.30%	****BELOW***
8.35000E+01	9.76000E-01	9.71466E-01	0.40%	****ABOVE***

APPENDIX B (continued)

m (10^{-3}mg/l) (measured)	R' (measured)	R' (least-squares)	Difference	
NH_4Cl 10%				
2.63000E+00	1.00010E+00	9.99983E-01	0.00%	****EVEN****
3.46000E+00	1.00150E+00	9.99459E-01	0.20%	****ABOVE***
3.99000E+00	9.97900E-01	9.99124E-01	0.10%	****BELOW***
5.50000E+00	9.94200E-01	9.98170E-01	0.30%	****BELOW***
6.47000E+00	9.96900E-01	9.97558E-01	0.00%	****EVEN****
7.68000E+00	1.00220E+00	9.96793E-01	0.50%	****ABOVE***
1.60600E+01	9.94900E-01	9.91500E-01	0.30%	****ABOVE***
1.75000E+01	9.90100E-01	9.90591E-01	0.00%	****EVEN****
1.99500E+01	9.86500E-01	9.89043E-01	0.20%	****BELOW***
2.38300E+01	9.89700E-01	9.86593E-01	0.30%	****ABOVE***
2.92000E+01	9.90500E-01	9.83201E-01	0.70%	****ABOVE***
3.45000E+01	9.73600E-01	9.79853E-01	0.60%	****BELOW***
3.99000E+01	9.74500E-01	9.76442E-01	0.10%	****BELOW***
KCl 10%				
1.51200E+00	9.98700E-01	9.98259E-01	0.00%	****EVEN****
2.20700E+00	9.98500E-01	9.98077E-01	0.00%	****EVEN****
2.52100E+00	9.98100E-01	9.97995E-01	0.00%	****EVEN****
4.41000E+00	9.95600E-01	9.97501E-01	0.10%	****BELOW***
4.91500E+00	9.98200E-01	9.97368E-01	0.00%	****EVEN****
8.51000E+00	9.96200E-01	9.96428E-01	0.00%	****EVEN****
1.16600E+01	9.97200E-01	9.95603E-01	0.10%	****ABOVE***
1.46900E+01	9.94900E-01	9.94811E-01	0.00%	****EVEN****
1.16600E+01	9.94100E-01	9.95603E-01	0.10%	****BELOW***
1.17200E+01	9.94100E-01	9.95588E-01	0.10%	****BELOW***
1.64000E+01	9.93200E-01	9.94363E-01	0.10%	****BELOW***
2.27000E+01	9.94200E-01	9.92715E-01	0.10%	****ABOVE***
3.02400E+01	9.91200E-01	9.90742E-01	0.00%	****EVEN****
3.53000E+01	9.95400E-01	9.89418E-01	0.60%	****ABOVE***
4.28000E+01	9.82600E-01	9.87455E-01	0.40%	****BELOW***
4.54000E+01	9.86500E-01	9.86775E-01	0.00%	****EVEN****

APPENDIX B (continued)

m (10^{-3}mg/l) (measured)	R' (measured)	R' (least-squares)	Difference	
NaCl 1%				
3.07600E+00	1.00200E+00	9.99236E-01	0.20%	****ABOVE***
5.74000E+00	9.96900E-01	9.97665E-01	0.00%	****EVEN****
1.09400E+01	9.91800E-01	9.94598E-01	0.20%	****BELOW***
1.53700E+01	9.90100E-01	9.91986E-01	0.10%	****BELOW***
1.94700E+01	9.90400E-01	9.89568E-01	0.00%	****EVEN****
2.12000E+01	9.90400E-01	9.88547E-01	0.10%	****ABOVE***
NH_4Cl 1%				
2.91500E+00	9.91600E-01	9.98221E-01	0.60%	****BELOW***
2.37000E+00	9.99500E-01	9.97948E-01	0.10%	****ABOVE***
2.96200E+00	9.94200E-01	9.97492E-01	0.30%	****BELOW***
3.67000E+00	1.00030E+00	9.96948E-01	0.30%	****ABOVE***
4.80000E+00	9.96500E-01	9.96078E-01	0.00%	****EVEN****
6.04000E+00	9.96400E-01	9.95123E-01	0.10%	****ABOVE***
7.11000E+00	9.96400E-01	9.94300E-01	0.20%	****ABOVE***
1.54000E+01	9.92000E-01	9.87919E-01	0.40%	****ABOVE***
2.07300E+01	9.76500E-01	9.83817E-01	0.70%	****BELOW***
9.59000E+00	9.94200E-01	9.92314E-01	0.10%	****ABOVE***
2.07000E+01	9.86400E-01	9.83840E-01	0.20%	****ABOVE***
KCl 1%				
1.45000E+00	1.00000E+00	9.99946E-01	0.00%	****EVEN****
2.30500E+00	9.99100E-01	9.99618E-01	0.00%	****EVEN****
3.16000E+00	9.95800E-01	9.99289E-01	0.30%	****BELOW***
4.52000E+00	9.99200E-01	9.98767E-01	0.00%	****EVEN****
7.51000E+00	1.00340E+00	9.97618E-01	0.50%	****ABOVE***
9.82000E+00	9.97400E-01	9.96730E-01	0.00%	****EVEN****
1.15200E+01	9.93400E-01	9.96077E-01	0.20%	****BELOW***
1.62300E+01	9.94200E-01	9.94268E-01	0.00%	****EVEN****
2.55900E+01	9.92300E-01	9.90672E-01	0.10%	****ABOVE***
2.73000E+01	9.88200E-01	9.90015E-01	0.10%	****BELOW***

APPENDIX C: Aggregate R' vs m Data and Comparison with Least-Squares Line

m (10^{-3}mg/l) (measured)	R' (measured)	R' (least-squares)	Difference	
1.67000E+00	9.96300E-01	9.99365E-01	0.30%	****BELOW***
2.63000E+00	1.00010E+00	9.98846E-01	0.10%	****ABOVE***
3.46000E+00	1.00150E+00	9.98398E-01	0.30%	****ABOVE***
3.99000E+00	9.97900E-01	9.98111E-01	0.00%	****EVEN****
5.50000E+00	9.94200E-01	9.97294E-01	0.30%	****BELOW***
6.47000E+00	9.96900E-01	9.96770E-01	0.00%	****EVEN****
7.68000E+00	1.00220E+00	9.96116E-01	0.60%	****ABOVE***
1.60600E+01	9.94900E-01	9.91584E-01	0.30%	****ABOVE***
1.75000E+01	9.90100E-01	9.90806E-01	0.00%	****EVEN****
1.99500E+01	9.86500E-01	9.89481E-01	0.30%	****BELOW***
2.38300E+01	9.89700E-01	9.87383E-01	0.20%	****ABOVE***
2.92000E+01	9.90500E-01	9.84479E-01	0.60%	****ABOVE***
3.45000E+01	9.73600E-01	9.81613E-01	0.80%	****BELOW***
3.99000E+01	9.74500E-01	9.78694E-01	0.40%	****BELOW***
1.39000E+00	1.00050E+00	9.99517E-01	0.00%	****EVEN****
1.93600E+00	1.00040E+00	9.99222E-01	0.10%	****ABOVE***
3.33000E+00	9.96100E-01	9.98468E-01	0.20%	****BELOW***
3.99500E+00	9.95700E-01	9.98108E-01	0.20%	****BELOW***
5.81000E+00	9.97000E-01	9.97127E-01	0.00%	****EVEN****
8.89000E+00	9.95600E-01	9.95461E-01	0.00%	****EVEN****
1.15000E+01	9.92400E-01	9.94050E-01	0.10%	****BELOW***
1.69400E+01	9.90100E-01	9.91109E-01	0.10%	****BELOW***
2.26800E+01	9.86700E-01	9.88005E-01	0.10%	****BELOW***
3.93000E+01	9.85900E-01	9.79018E-01	0.70%	****ABOVE***
5.14000E+01	9.80100E-01	9.72475E-01	0.70%	****ABOVE***
6.53000E+01	9.74100E-01	9.64959E-01	0.90%	****ABOVE***
8.35000E+01	9.76000E-01	9.55118E-01	2.10%	****ABOVE***
1.81700E+00	9.97300E-01	9.99286E-01	0.10%	****BELOW***
3.15000E+00	1.00130E+00	9.98565E-01	0.20%	****ABOVE***
4.17500E+00	9.96800E-01	9.98011E-01	0.10%	****BELOW***
6.04000E+00	9.94600E-01	9.97002E-01	0.20%	****BELOW***
1.57700E+01	9.89300E-01	9.91741E-01	0.20%	****BELOW***
2.36500E+01	9.84700E-01	9.87480E-01	0.20%	****BELOW***
3.32400E+01	9.73200E-01	9.82295E-01	0.90%	****BELOW***
4.52500E+01	9.65700E-01	9.75801E-01	1.00%	****BELOW***
4.80000E+01	9.72000E-01	9.74314E-01	0.20%	****BELOW***
4.38000E+01	9.73000E-01	9.76585E-01	0.30%	****BELOW***
5.89000E+01	9.70600E-01	9.68420E-01	0.20%	****ABOVE***
7.20000E+01	9.55000E-01	9.61336E-01	0.60%	****BELOW***
8.91000E+01	9.50800E-01	9.52090E-01	0.10%	****BELOW***
9.25000E+01	9.41000E-01	9.50252E-01	0.90%	****BELOW***
1.16600E+02	9.26900E-01	9.37220E-01	1.10%	****BELOW***

APPENDIX C (continued)

m (10^{-3}mg/l) (measured)	R' (measured)	R' (least-squares)	Difference	
1.09800E+00	1.00170E+00	9.99675E-01	0.20%	****ABOVE***
1.55300E+00	1.00970E+00	9.99429E-01	1.00%	****ABOVE***
1.87500E+00	9.96200E-01	9.99255E-01	0.30%	****BELOW***
2.14300E+00	9.96900E-01	9.99110E-01	0.20%	****BELOW***
2.62400E+00	9.95000E-01	9.98850E-01	0.30%	****BELOW***
3.48000E+00	9.95600E-01	9.98387E-01	0.20%	****BELOW***
4.39000E+00	9.98700E-01	9.97895E-01	0.00%	****EVEN****
5.14000E+00	9.93700E-01	9.97489E-01	0.30%	****BELOW***
6.00000E+00	9.97100E-01	9.97024E-01	0.00%	****EVEN****
7.23000E+00	9.93800E-01	9.96359E-01	0.20%	****BELOW***
9.37000E+00	9.93300E-01	9.95202E-01	0.10%	****BELOW***
1.39200E+01	9.87900E-01	9.92742E-01	0.40%	****BELOW***
1.87500E+01	9.90200E-01	9.90130E-01	0.00%	****EVEN****
2.25000E+01	9.84500E-01	9.88102E-01	0.30%	****BELOW***
2.54500E+01	9.81300E-01	9.86507E-01	0.50%	****BELOW***
3.05200E+01	9.83300E-01	9.83766E-01	0.00%	****EVEN****
3.58800E+01	9.74500E-01	9.80867E-01	0.60%	****BELOW***
1.24000E+00	9.98300E-01	9.99598E-01	0.10%	****BELOW***
2.24000E+00	1.00160E+00	9.99057E-01	0.30%	****ABOVE***
4.16000E+00	9.97000E-01	9.98019E-01	0.10%	****BELOW***
4.88000E+00	9.96100E-01	9.97630E-01	0.10%	****BELOW***
6.48000E+00	9.96100E-01	9.96765E-01	0.00%	****EVEN****
7.68000E+00	9.94300E-01	9.96116E-01	0.10%	****BELOW***
1.08000E+01	9.89400E-01	9.94429E-01	0.50%	****BELOW***
1.52000E+01	9.90000E-01	9.92049E-01	0.20%	****BELOW***
2.56000E+01	9.87600E-01	9.86426E-01	0.10%	****ABOVE***
3.20000E+01	9.76900E-01	9.82965E-01	0.60%	****BELOW***
4.08000E+01	9.78100E-01	9.78207E-01	0.00%	****EVEN****
7.04000E+01	9.58100E-01	9.62202E-01	0.40%	****BELOW***
8.64000E+01	9.54300E-01	9.53550E-01	0.00%	****EVEN****
1.51200E+00	9.98700E-01	9.99451E-01	0.00%	****EVEN****
2.20700E+00	9.98500E-01	9.99075E-01	0.00%	****EVEN****
2.52100E+00	9.98100E-01	9.98905E-01	0.00%	****EVEN****
4.41000E+00	9.95600E-01	9.97884E-01	0.20%	****BELOW***
4.91500E+00	9.98200E-01	9.97611E-01	0.00%	****EVEN****
8.51000E+00	9.96200E-01	9.95667E-01	0.00%	****EVEN****
1.16600E+01	9.97200E-01	9.93964E-01	0.30%	****ABOVE***
1.46900E+01	9.94900E-01	9.92325E-01	0.20%	****ABOVE***
1.16600E+01	9.94100E-01	9.93964E-01	0.00%	****EVEN****
1.17200E+01	9.94100E-01	9.93931E-01	0.00%	****EVEN****
1.64000E+01	9.93200E-01	9.91401E-01	0.10%	****ABOVE***
2.27000E+01	9.94200E-01	9.87994E-01	0.60%	****ABOVE***
3.02400E+01	9.91200E-01	9.83917E-01	0.70%	****ABOVE***
3.53000E+01	9.95400E-01	9.81181E-01	1.40%	****ABOVE***
4.28000E+01	9.82600E-01	9.77125E-01	0.50%	****ABOVE***
4.54000E+01	9.86500E-01	9.75720E-01	1.10%	****ABOVE***

APPENDIX C (continued)

m (10^{-3}mg/l) (measured)	R' (measured)	R' (least-squares)	Difference	
1.45000E+00	9.99500E-01	9.99484E-01	0.00%	****EVEN****
2.30500E+00	9.98600E-01	9.99022E-01	0.00%	****EVEN****
3.16000E+00	9.95300E-01	9.98560E-01	0.30%	****BELOW***
4.52000E+00	9.98700E-01	9.97824E-01	0.00%	****EVEN****
7.51000E+00	1.00290E+00	9.96208E-01	0.60%	****ABOVE***
1.15200E+01	9.92900E-01	9.94039E-01	0.10%	****BELOW***
9.82000E+00	9.96900E-01	9.94959E-01	0.10%	****ABOVE***
1.62300E+01	9.93700E-01	9.91492E-01	0.20%	****ABOVE***
2.55900E+01	9.91800E-01	9.86431E-01	0.50%	****ABOVE***
2.73000E+01	9.87700E-01	9.85507E-01	0.20%	****ABOVE***
2.01500E+00	9.93500E-01	9.99179E-01	0.50%	****BELOW***
2.37000E+00	1.00140E+00	9.98987E-01	0.20%	****ABOVE***
2.96200E+00	9.96100E-01	9.98667E-01	0.20%	****BELOW***
3.67000E+00	1.00220E+00	9.98284E-01	0.30%	****ABOVE***
4.80000E+00	9.98400E-01	9.97673E-01	0.00%	****EVEN****
6.04000E+00	9.98300E-01	9.97002E-01	0.10%	****ABOVE***
7.11000E+00	9.98300E-01	9.96424E-01	0.10%	****ABOVE***
1.54000E+01	9.97900E-01	9.91941E-01	0.60%	****ABOVE***
9.69000E+00	9.96100E-01	9.95029E-01	0.10%	****ABOVE***
2.07000E+01	9.88300E-01	9.89075E-01	0.00%	****EVEN****
3.07600E+00	1.00100E+00	9.98605E-01	0.20%	****ABOVE***
5.74000E+00	9.95900E-01	9.97165E-01	0.10%	****BELOW***
1.09400E+01	9.90800E-01	9.94353E-01	0.30%	****BELOW***
1.53700E+01	9.89100E-01	9.91958E-01	0.20%	****BELOW***
1.94700E+01	9.89400E-01	9.89741E-01	0.00%	****EVEN****
2.12000E+01	9.89400E-01	9.88805E-01	0.00%	****EVEN****

APPENDIX D: Particle Size Distribution Data

Diameter (microns)	Number Count								
	NaCl			NH_4Cl			KCl		
	1%	10%	20%	1%	10%	20%	1%	10%	20%
0.3	115			120					
0.4	74	36	11	92	15	7	98	16	13
0.6	37	88	28	10	103	16	94	130	45
0.8	4	55	58	4	93	24	32	73	50
1.2	7	37	67	3	24	52	5	26	47
1.7		7	42		6	62		6	22
2.5		2	10			13		2	19
3.5						5			9
Mean (microns)	0.41	0.76	1.13	0.37	0.75	1.39	0.55	0.74	1.19

APPENDIX E: Penndorf's Method for Calculating the General Shape of the Scattering Efficiency Curve.

Penndorf (1958) has developed empirical expressions for the values of $\rho = 2\alpha(n-1)$, where n is the particle index of refraction, at which the extrema of the scattering efficiency curve occur and the value of the scattering efficiency at these extrema.

The equation for the location of the extrema is given by:

$$\rho_y(n) = \rho_y(1) + 0.3(n-1) \qquad \text{(E-1)}$$

where: $\rho_y(n)$ is the value of ρ corresponding to the yth max. or min.

n is the particle index of refraction

$\rho_y(1)$ is given by the following table:

TABLE E-1

maxima y	y(1)	minima y	y(1)
1	4.08	1	7.62
2	10.79	2	14.0
3	17.16	3	20.32
4	23.47	4	26.63
5	29.78	5	32.93

α is obtained from the definition of ρ.

The equation for the values of $Q_y(n)$, the scattering efficiency at the yth maxima or minima, is given by:

$$Q_y(n) = a + bM \qquad \text{(E-2)}$$

where: $M = (n^2-1)/(n^2+2)$ (E-3)

a and b are given by the following table:

TABLE E-2

y	at the maxima a	at the maxima b	at the minima a	at the minima b
1	3.173	4.02	1.542	0.579
2	2.404	2.25	1.734	0.433
3	2.247	1.52	1.813	0.328
4	2.178	1.14	1.855	0.262
5	2.139	0.92	1.822	0.218

Kerker (1969) states that an accuracy of 3% or better can be obtained by drawing a smooth curve between the values of the extrema.

Using equation (E-1) and table (E-1), and equations (E-2) and (E-3) and table (E-2), the following table can be constructed for the three values of n corresponding to the three experimental aerosol materials:

TABLE E-3

Aerosol	n	y	Maximum α	Maximum Q	Minimum α	Minimum Q
KCl	1.49	1	4.31	4.23	7.93	1.71
		2	11.18	3.05	14.43	1.85
NH_4Cl	1.64	1	3.34	4.62	6.10	1.75
		2	8.58	3.21	11.67	1.89
NaCl	1.54	1	3.92	4.43	7.20	1.72
		2	10.13	3.10	13.53	1.86

Drawing smooth curves through these extrema results in Figure 35.